High-Pressure Synthesis, Crystal Structures and Physical Properties of A-Site Columnar-Ordered Quadruple Perovskites

A Thesis

Submitted by

Ran LIU

In fulfillment for the award of the degree of

Doctor of Science

Graduate School of Chemical Sciences and Engineering,

Hokkaido University

2021

Abstract

Perovskite materials have been intensively researched for decades. Complex and attractive thermoelectric, electrochemical, catalytic, and multiferroic properties of perovskites originate from an interplay among spin, charge, and orbital degrees of freedom. The perovskite-type structure has become one of the most adaptive structures in inorganic and solid-state chemistry with many representatives such as $CaMnO_3$-based compounds. ABO_3 is the basic stoichiometry of the perovskite-type structure. But there are also special classes of perovskites with other specific stoichiometries like quadruple perovskites $A'A_3B_4O_{12}$ and $A_2A'A''B_4O_{12}$ and so on. In this work, using R_2O_3 (R = rare earth elements), transition metals, and alkali metals, we aimed on designing and preparation of new perovskite-type materials belonging to the $A_2A'A''B_4O_{12}$ family. Crystal structures, magnetic properties, and other physical properties of prepared perovskites were investigated.

Chapter 1 introduces the general background including the basic structure, magnetism, and some magnetic materials and their applications, and so on. Chapter 2 mainly presents the techniques we used in this research. From chapters 3 to 5 pay attention to the three different perovskite compounds study. And the conclusions are given in chapter 6.

Chapter 3 illustrates the compounds $Y_2MnGa(Mn_{4-x}Ga_x)O_{12}$ (x = 0, 1, 2, and 3) which were synthesized at high pressure and high temperature. Samples exhibit spin-glass-like magnetic behaviors. Synchrotron X-ray and neutron powder diffraction were used to study the crystal structures and cation distributions. These solutions adapt the parent structure of the A-site columnar-ordered quadruple perovskite family with space group $P4_2/nmc$ (No. 137). They have lattice parameters of a = 7.36095 Å and c = 7.75384 Å (x = 0), a = 7.36168 Å and c = 7.71616 Å (x = 1), a = 7.36034 Å and c = 7.67142 Å (x = 2), and a = 7.36393 Å and c = 7.61685 Å (x = 3) at room temperature. The x = 0 sample has a cation distribution of $[Y^{3+}_2]_A[Mn^{3+}]_{A'}[Ga^{3+}_{0.68}Mn^{2+}_{0.32}]_{A''}[Mn_{3.68}Ga_{0.32}]_BO_{12}$ with a preferred localization of Ga^{3+} in

the tetrahedral A″ site and with a small amount of Ga^{3+} in the octahedral B site. A complete triple A-site order, $[Y^{3+}{}_2]_A[Mn^{3+}]_{A'}[Ga^{3+}]_{A''}[Mn^{3+}{}_{4-x}Ga^{3+}{}_x]_BO_{12}$, is realized for $x \geqslant 1$. All samples demonstrate spin-glass-like magnetic properties, and the absence of a long-range magnetic order at the ground state at 1.5 K was confirmed by neutron diffraction for the $x = 1$ sample. First-principles calculations indicated the spin-glass-like magnetic ordering is derived from the Ga substitution to the B sites and gave evidence that the ideal cation distribution could produce robust ferromagnetism in this family of perovskites.

Chapter 4 presents the ABO_3 perovskites have many ferroelectric instabilities that result from the varieties of long-range and short-range polar distortions. On the other hand, polar distortions are very limited in quadruple perovskites $AA'_3B_4O_{12}$ and $A_2A'A''B_4O_{12}$. Here we showed that $R_2MnMn(MnTi_3)O_{12}$ (R = Nd, Eu, and Gd) belongs to the family of A-site columnar-ordered quadruple perovskites. $R_2MnMn(MnTi_3)O_{12}$ compounds exhibit relaxor-like ferroelectric properties slightly below room temperature. They were synthesized by a high-pressure high-temperature method for R = Nd, Eu, and Gd at about 6 GPa and 1570 K. At room temperature they crystallize in centrosymmetric space group $P4_2/nmc$ (No. 137), and their crystal structures were studied by synchrotron powder X-ray diffraction. They exhibit broad dielectric anomalies just below room temperature with characteristic frequency-dependent features of the relaxor ferroelectric behavior. *P*–*E* loop measurements at 77 K confirmed ferroelectricity for R = Nd and Eu. Magnetic and specific heat measurements showed the presence of long-range ferrimagnetic transitions below 20 K (R = Nd), 30 K (R = Eu), and 42 K (R = Gd). Additional specific heat anomalies were observed below about 5 K for R = Nd, and Gd probably due to the involvement of rare-earth cations in long-range orderings. The coexistence of ferrimagnetic transitions and relaxor-like ferroelectric properties make $R_2MnMn(MnTi_3)O_{12}$ perovskites become multiferroic materials.

Chapter 5 shows $NaRMn_2Ti_4O_{12}$ (R = Sm, Eu, Gd, Dy, Ho, and Y) compounds which prepared at high pressure (about 6 GPa) and high temperature (about 1750 K) conditions. Those

samples adopt an A-site columnar-ordered quadruple-perovskite structure with the generic chemical formula $A_2A'A''B_4O_{12}$. Their crystal structures were studied by powder synchrotron X-ray and neutron diffraction between 1.5 and 300 K. They maintain a paraelectric structure with centrosymmetric space group $P4_2/nmc$ (No. 137) at all temperatures, in comparison with the related $CaMnTi_2O_6$ perovskite, in which a ferroelectric transition occurs at 630 K. The centrosymmetric structure was also confirmed by second-harmonic generation. It has a cation distribution of $[Na^+R^{3+}]_A[Mn^{2+}]_{A'}[Mn^{2+}]_{A''}[Ti^{4+}{}_4]_BO_{12}$ (to match with the generic chemical formula) with statistical distributions of Na^+ and R^{3+} at the large A site and a strongly split position of Mn^{2+} at the square-planar A′ site. We found a C-type long-range antiferromagnetic structure of Mn^{2+} ions at the A′ and A″ sites below T_N = 12 K for R = Dy and found that the presence of Dy^{3+} disturbs the long-range ordering of Mn^{2+} below a second transition at lower temperatures. The first magnetic transition occurs below 8−13 K in all compounds, but the second magnetic transition occurs only for R = Dy, Sm, Eu. All compounds show large dielectric constants of a possible extrinsic origin similar to that of $CaCu_3Ti_4O_{12}$. $NaRMn_2Ti_4O_{12}$ with R = Er−Lu crystallized in the $GdFeO_3$-type *Pnma* perovskite structure, and $NaRMn_2Ti_4O_{12}$ with R = La, Nd contained two perovskite phases: an $AA'_3B_4O_{12}$-type *Im*−3 phase and a $GdFeO_3$-type *Pnma* phase.

Chapter 6 presents the general conclusion and prospects based on this work.

Keywords: Perovskite, High-pressure synthesis, Crystal structure, Magnetic property.

List of Abbreviations

MPMS	Magnetic property measurement system
PPMS	Physical property measurement system
XRPD	X-ray powder diffraction
SXRD	Synchrotron X-ray diffraction
RT	Room Temperature
FC	Field cooling
ZFC	Zero field cooling
T_C	Curie temperature
T_N	Neel temperature
AFM	Antiferromagnetic
FM	Ferromagnetic
t	Tolerance factor
θ	Weiss temperature
C	Curie constant
μ_{eff}	Effective magnetic moment
BVS	Bond valance sum
C_p	Heat capacity
NIMS	National Institute for Materials Science
χ	Magnetic susceptibility
ρ	Electrical resistivity

High-Pressure Synthesis, Crystal Structures and Physical Properties of A-Site Columnar-Ordered Quadruple Perovskites

Contents

Chapter 1. Introduction

1.1. Perovskite crystal structure

1.1.1. Traditional perovskite structure

ABO_3 compounds synthesis to a lot of structures, such as perovskites, $LiNbO_3$, corundum, ilmenite, hexagonal $BaMnO_3$-type structures, hexagonal $LuMnO_3$-type, pyroxenes, rare earth sesquioxide structures (A, B and C (bixbyite)), $AlFeO_3$, $KSbO_3$, $PbReO_3$, $CaIrO_3$ and others, based on the deference of size and natural properties for A and B cations. [1] The perovskite-type structure may be a standout amongst those practically critical and versatile structures for inorganic chemistry. [2–4] It will be assembled from a skeleton for corner imparted BO_6 octahedra that structure cavities, which would be filled with cations. Those perfect perovskite structures may be cubic (space assembly *Pm*–3*m*) for $a_p \approx 3.8$ Å. However, that cubic structure may be infrequently acknowledged during room temperature due to the befuddle around those sizes for A, B furthermore O. This mismatch, which may be normally portrayed by the Goldschmidt tolerance factor, prompts different distortions. [5] Distortions could be acknowledged as tilts for unbending BO_6 octahedra on a main close estimation. Thus, slants are portrayed by utilizing the Glazer slant framework and the B–O–B bond. [6] In the basic ABO_3 structure, the B–O–B tilt angles are between 140° and 180°. **Figure 1.1.** shows the ideal perovskite structure.

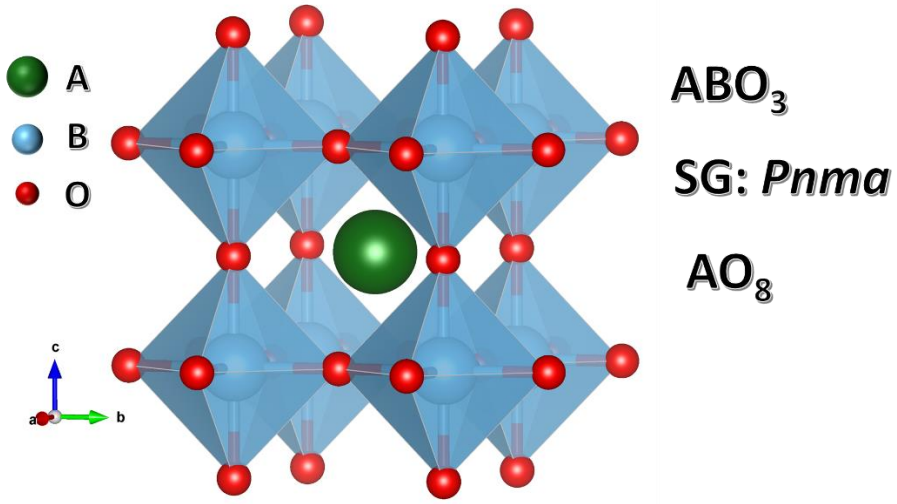

Figure 1.1. ABO_3 ideal perovskite structure.

1.1.2. A special class of the perovskite

An extraordinary class of the perovskite family is framed for the a+a+a+ slant framework with huge B–O–B slant points of around 140–145° (from the base space group *Im*–3). [7,8] $AA'_3B_4O_{12}$ structures, called A-site-ordered quadruple perovskites, have a twelve-fold coordination A site and a square-planar coordination A′ site. (**Figure 1.2.**) The A′ positions most are the the Jahn–Teller cations (such as, Cu^{2+} and Mn^{3+}) or other cations which were called square-planar coordination: Cu^{3+},[8] Fe^{2+},[9,10] Co^{2+},[11] Pd^{2+},[12] Pb^{4+},[13] and Mn^{2+}. [14] To gain the $AA'_3B_4O_{12}$ perovskites usually need high pressure (HP) and high temperature (HT). A lot of the representatives of the subfamily perovskite structure $AA'_3B_4O_{12}$ with A = Na^+, Mn^{2+}, Cd^{2+}, Ca^{2+}, Sr^{2+}, Pb^{2+}, R^{3+} (R = rare earths), Ce^{4+}, Bi^{3+} and Th^{4+}, and B = Mn^{3+}, Mn^{4+}, Fe^{3+}, Cr^{3+}, Al^{3+}, Ti^{4+}, V^{4+}, Ge^{4+}, Sn^{4+}, Ru^{4+}, Ir^{4+}, Ta^{5+}, Nb^{5+}, Sb^{5+} and others are quadruple perovskite. [7] This subfamily, $AA'_3B_4O_{12}$, was discovered in 1967 in $CaCu_3Ti_4O_{12}$ during Cu^{2+} doping of $CaTiO_3$. [15] Since then, there needs more significant research favor to create new parts about such quadruple perovskites. These efforts promote numerous fascinating phenomena about physical and chemical properties which were discovered. For instance, giant dielectric constant,[7] inter-site charge transfer and disproportionation, [8] multiferroic properties, reentrant structural transitions,[16] and high catalytic activity.[17]

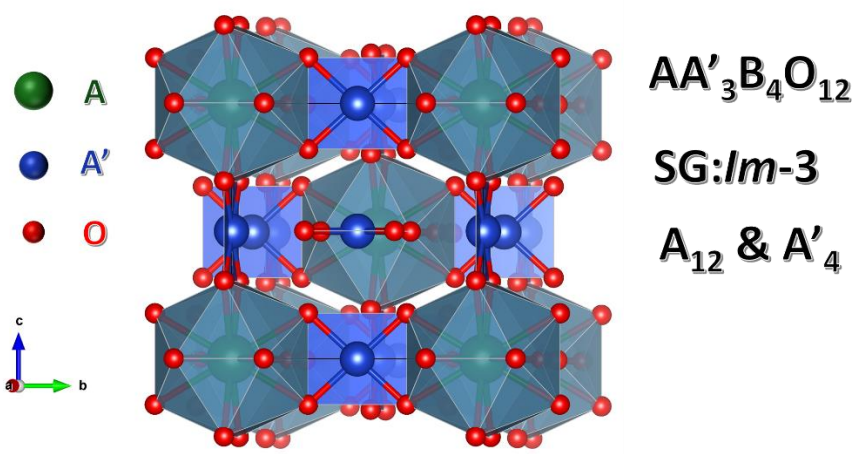

Figure 1.2. Fragments of structures with polyhedra for the A, A′and A″ sites in $AA'_3B_4O_{12}$ quadruple perovskites. [4]

1.1.3. Another special class of the perovskite

Another extraordinary perovskite family could be structured for those a+a+c− tilt framework and extremely vast B–O–B tilt angles range of 140–150° (from the base space group *P*4_2*/nmc*).[3,4] For this situation, another structure, also named A-site-ordered quadruple perovskites, $A_2A'A''B_4O_{12}$ stoichiometry were found, where A′site is still occupied by the square-planar cations, however the A″ site occupied by the tetrahedral coordination. We call this structure is A-site columnar-ordered for distinguishing the $AA'_3B_4O_{12}$. [18] This subfamily representer, $CaFeTi_2O_6$, was discovered in 1995. [9,19,20] Then in the later time about 19 years, there is no new members were found,[3,4] until 2014, the $CaMnTi_2O_6$ were reported. [21] In recent years, so many new $A_2A'A''B_4O_{12}$ quadruple perovskites have been observed.[18, 22-24]

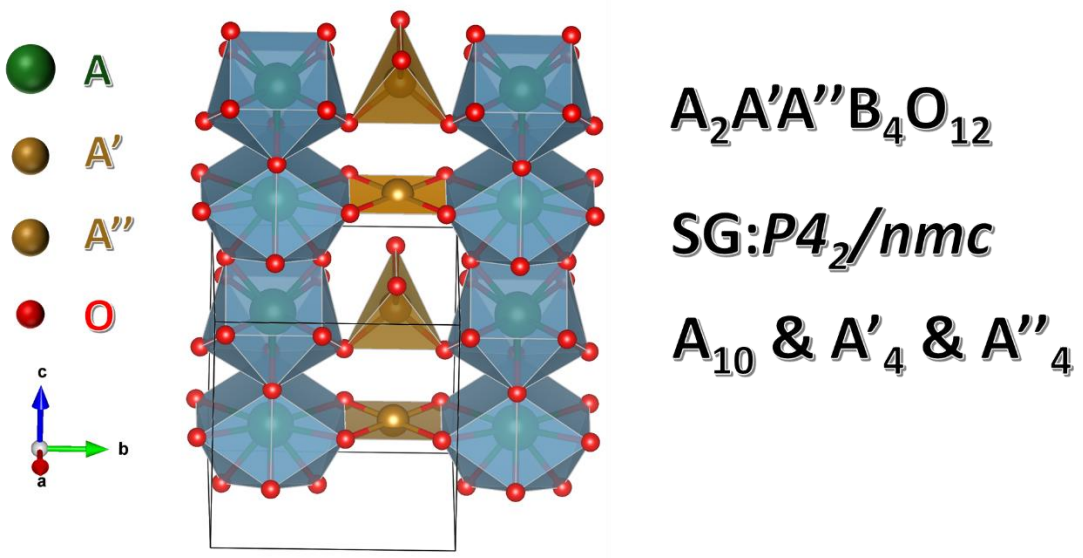

Figure 1.3. Fragments of structures with polyhedra for the A, A′, and A″ sites $A_2A'A''B_4O_{12}$ quadruple perovskites. [4]

1.2. Magnetism

1.2.1. Origin of magnetism

Magnetism is an intimate property that responds to an applied magnetic field, which originates from the electrons of atoms, especially unpaired electrons. Magnetism is associated with the *angular momentum of elementary particles*, [25,26] so this magnetism quantum theory is closely linked to the quantization of angular momentum. Protons, neutrons, and electrons have an intrinsic angular momentum $\frac{1}{2}\ \hbar$ which know as the spin, where $\hbar$ is Planck's constant h divided by 2π. Magnetic moments of electronic spin are usually bigger than the nuclear spin creates. Because of that nucleon has a much greater mass, $\approx 1.67 \times 10^{-27}$ kg. We did not care about nuclear magnetism, however, pay more attention to electronic magnetism, which is also the main factor considered in solid. An elementary particle, electron, has charge $-e$ and m_e that are two different sources of angular momentum. One of them is connected with the orbital motion around the nucleus, another is associate with the spin. In atomic physics, the *Bohr magneton* (symbol μ_B) is the natural unit (smallest unit) for stating the magnetic moment of an

electron, which is caused by either its orbital or spin angular momentum. The Bohr magneton is defined as $\mu_B = \frac{e\hbar}{2m_e}$, where e is the elementary charge, $\hbar$ is the reduced Planck constant, m_e is the electron rest mass.

Considering the main factor of magnetism is electron spins μ_S, $\mu_S = g\sqrt{S(S+1)}\mu_B$, where S is the sum of the spin quantum numbers and g is the gyromagnetic ratio, also known as the "g factor" (free electrons: 2.00023). When both spin and orbital motions of electrons are considered, the total magnetic moment will become $\mu_{S+L} = \sqrt{4S(S+1) + L(L+1)}\mu_B$, where L is the sum of the orbital angular momentum. In general, most of the 3d transition metal ions do possess orbital angular momentum.

1.2.2. Types of magnetic behaviors

Some different types of magnetic states were shown in **Figure 1.4.** [27] (a) paramagnetic, [28] the unpaired electron spins are oriented at random directions; (b) ferromagnetic, all of the unpaired electron spins align in parallel; (c) antiferromagnetic, the spins are aligned antiparallel; (d) canted antiferromagnetic or weak ferromagnetic, all of the spins are canted to each other; (e) ferrimagnetic, there is a net magnetic moment because of the moments of the aligned and anti-aligned are unequal.

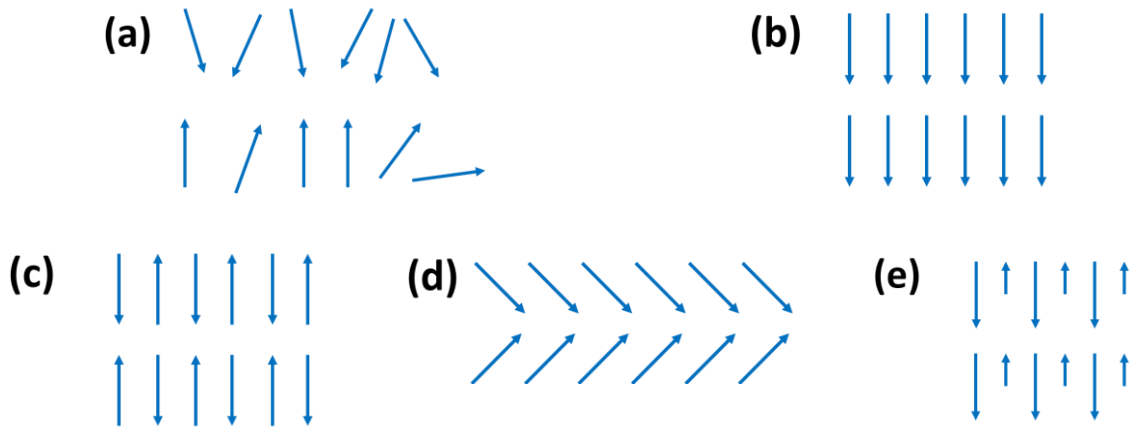

Figure 1.4. Schematic magnetic phenomena: (a) paramagnetism; (b) ferromagnetism; (c) antiferromagnetism; (d) canted antiferromagnetism or weak ferromagnetism, and (e) ferrimagnetism

1.2.2.1 Ferromagnetism and exchange

Ferromagnetism and the Curie temperature were demonstrated by Weiss in terms of a huge internal "molecular field" proportional to the magnetization, which theory including the localized and delocalized electrons. No such magnetic field exists. But this was regarded as a useful approach to approximate the effect of the interatomic Coulomb interaction in quantum mechanics, which $\mathcal{H} = -2\mathcal{J}\mathbf{S}_1 \cdot \mathbf{S}_2$, where **S1** and **S2** are operators describing the localized spins on two adjacent atoms. If $\mathcal{J} > 0$, there is the ferromagnetic order that exists in three dimensions. In the exchange-coupled magnetic lattice, the spin waves are the low-energy exist. A ferromagnet has spontaneously spin-split energy bands in the delocalized electron area. Spin-dependent density functional theory can effectively calculate the density of $\uparrow$ and $\downarrow$ states.

The spontaneous magnetization ***M*s**, which is due to the alignment of the magnetic moments located on an atomic lattice, is the characteristic feature of a ferromagnet. Basing on the crystal structure, sample shape, or atomic scale positions the magnetization like to lie along the easy axis. If heating above the Curie point will reduce the reversible collapse of the spontaneous magnetization.

1.2.2.2 Antiferromagnetism and exchange

Antiferromagnetism is an interesting magnetic order. A crystal lattice is divided into two or more sublattices. All their net magnetization is zero. Louis Néel is the first to research the antiferromagnetic ordering transition, [29] points that this magnetic susceptibility exists in a small peak. And the natural specific heat is similar to that marked at Curie point of a ferromagnet. Until the neutron scattering appeared, this sublattice magnetization $M\alpha$ was measured directly. Sublattice magnetization is the order parameter. In at least one direction,

this conjugate field is a staggering field that alternates in the direction from one atomic site to the next.

1.2.2.3. Other magnetic order

A ferrimagnet can be seen as the antiferromagnet which including two unequal sublattices. Most oxides with net magnetization are ferrimagnets. An example is yttrium-iron garnet (YIG) $Y_3Fe_5O_{12}$. The iron in YIG (Fe^{3+}, $3d^5$) stays at two different positions. One (16*a*) site at octahedra coordination by oxygen, the other (24*d*) occupy the tetrahedra positions by oxygen. Neighboring positions share common oxygen coordination, and a strong antiferromagnetic *a*-*d* interaction exists. This ferrimagnetic framework causes a moment of $5\mu_B$ per formula at $T = 0$ K, because of the single uncompensated $3d^5$ ion per formula unit.

The significant feature of a spin glass is the cusp in susceptibility when zero-field cooling (ZFC). When the temperature $T_f < \Delta\mathcal{J} / k_B$, called the spin freezing temperature, the spins freeze in random directions. In this system, there are several nearly degenerate magnetic ground-state configurations, if a field is applied, the biggest net moment in one direction of the field will be picked out. So different with the ferromagnet, where the response to a small applied field is reversible given, there is no coercivity. The spin-glass between field-cooled (FC) and zero-field-cooled (ZFC) responses is so different. There is a small remanent magnetization being frozen in below T_f in the FC. Another experimental signature of canonical spin glass is the specific heat of magnetic origin, which is linear in temperature and independent of the number of magnetic impurities when the temperature is below T_f, while there are no specific heat changes at the freezing temperature.

1.2.4. Magnetic susceptibility and Curri–Weiss law

When put the substance into a magnetic field $\boldsymbol{H}$, there will cause magnetization $\boldsymbol{M}$ on the substance, which phenomenon between $\boldsymbol{H}$ and $\boldsymbol{M}$ can use the formula $\boldsymbol{M} = \chi\boldsymbol{H}$ to make an

explanation. The proportional coefficient χ is as we all know the magnetic susceptibility of the substance. The values of χ could be used to distinguish the different sorts of magnetic behavior. When we discuss the diamagnetic substances, usually the χ is regarded as small and slightly negative. However, the paramagnetic substances, χ is small and positive. In ferromagnetic substances, $\chi < 1$ and such materials are strongly impacted by the magnetic field. In antiferromagnetic substances, χ is positive and the value may be comparable to or somewhat less than that for paramagnetic substances. [28]

Besides the absolute magnitudes, the temperature dependence of susceptibilities for different kinds of magnetic materials is also a significant parameter to distinguish them. Considering the ferro-, ferri-, antiferro-, heli-magnetic or spin-glass, when the temperature is above the Curie temperature as we all know, T_c (ferro- and ferri-magnets), or the Néel point, T_N (antiferro- and heli-magnets), those compounds will lose the spin order to become the paramagnetic structure. At these transition temperatures, there is a balance between the exchange interactions and the thermal energy, in which the former maintains the ordered-aligned structures and the latter tend to randomize the orientation of spins. **Figure 1.5.** [30] explain the schematic figure of the temperature dependence for the magnetic susceptibility of different magnetic behaviors.

The simple Curie law can perfectly explain the paramagnetic material behaviors, which pronounces that the magnetic susceptibility of a material is inversely proportional to temperature: $\chi = C/T$, where C is Curie constant. Such a Curie behavior can be found when there is no spontaneous interaction between adjacent unpaired electrons. [30] With the temperature increase, the alignment order will become more and more difficult, then the χ will be reduced. Besides the paramagnetic compounds, we usually use a more general Curi–Weiss law, $\chi = C/T - \theta$ to explain those cases when there exists the spontaneous interaction between adjacent spins, where C is the Curie constant and θ is the Weiss constant. We can

calculate the effective moment based on the Currie constant, which can be got from Currie's law or Curie–Weiss law, using the equation $\mu_{\text{eff}} = 2.84\sqrt{\chi(T-\theta)} = 2.84\sqrt{C}$. [30]

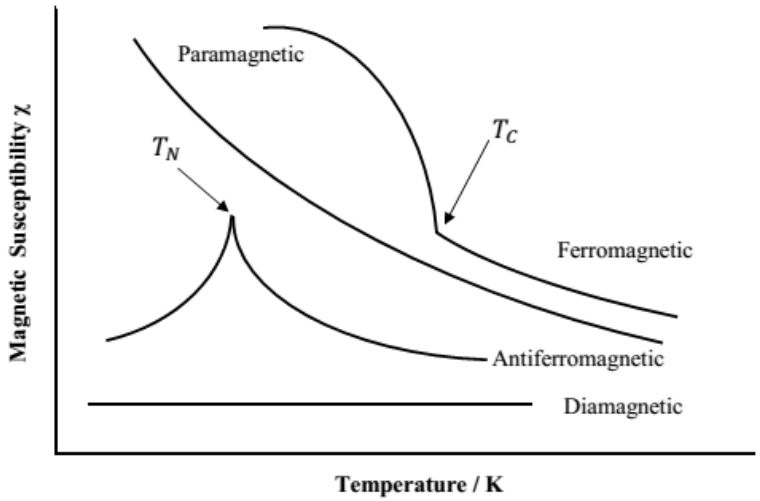

Figure 1.5. The temperature dependence of the magnetic susceptibility of diamagnetic, paramagnetic, ferromagnetic, and antiferromagnetic materials. [27]

1.3. Chemical Environments

1.3.1. Crystal field

The crystal field is an electric field that origin from surrounding ligands in the crystal, in the perovskite which is mainly caused by the negatively charged electrons in the oxygen orbitals. [31]

Considering the *d* orbitals of transition metal ions in a perovskite structure, the metal center is usually surrounded by six oxygen ions, which support that neighboring atoms arise the crystal field potential, impact the free diffusion of electrons, and quench orbital angular momentum by splitting of the *d* orbitals. [32] The *d* orbitals split into two parts. The first are d_{x2-y2} and d_{z2} orbitals also called e_g orbitals, which point to *p* orbitals of ligands oxygen ions, which are raised in energy. The second are d_{zx}, d_{yz}, and d_{xy} orbitals, also called t_{2g} orbitals, which point diagonally between the *p* orbitals, are relatively unaffected by the field. The resulting energy

difference is identified as Δ*o* showing in **Figure 1.6.**

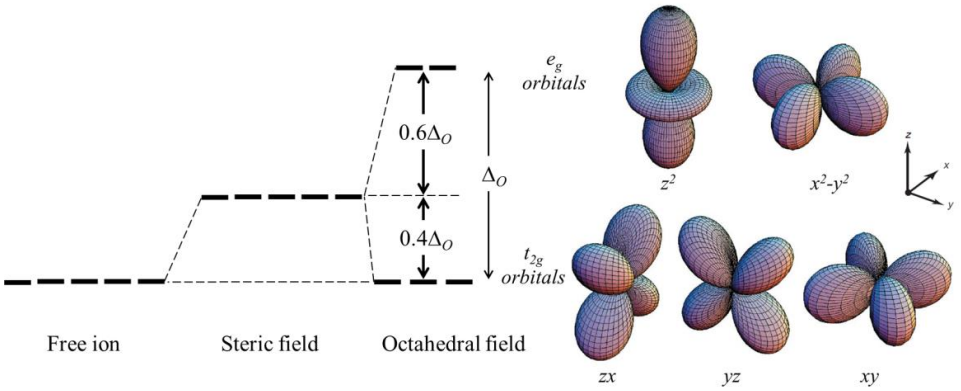

Figure 1.6. The *d* orbital splitting in octahedral field conditions. [35]

1.3.2. The Jahn-Teller effect

A single electron (or hole) in the degenerate level tends to distort spontaneously,[28] shown as **Figure 1.7.**, which is called the *Jahn-Teller effect*. This effect is significantly impacting the d^4 and d^9 ions in octahedral structure (Mn^{3+}, Cu^{2+}),[33 34, 35, 36] which can effectively reduce the energy through distorting the coordination. When the local strain is ϵ, the energy change can be expressed as $\delta\varepsilon = -A\,\epsilon + B\,\epsilon^2$, where the first part is crystal-field stabilization energy and the second is the increased elastic energy. The *A* and *B* are constants and the minimum of energy is at $\epsilon = A/2B$. The former, crystal energy, keeps a crucial role in stabilizing ionic structures. Considering the d^1 stabilization energy is $0.4\ \Delta_{oct}$ at the octahedral site, that can splits to the t_{2g} levels by further increased the uniaxial distortion.[28] The splitting keeps the center of gravity level, e_g levels are increased $0.6\Delta_{oct}$ while the t_{2g} levels are reduced $-\ 0.4\Delta_{oct}$ in an octahedral crystal field (**Figure 1.7.**). [37] The d^5 ions Fe^{2+} or Mn^{2+}, which represent no crystal-field stabilization energy because all orbits singly are occupied. [38 39, 40, 41]

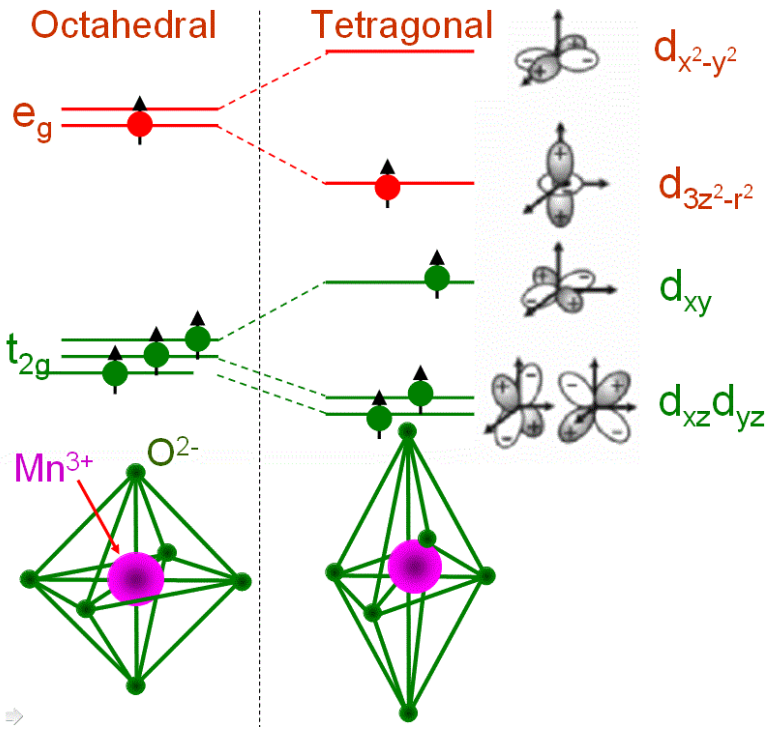

Figure 1.7. Jahn–Teller distortion of an octahedral site containing a d^4 ion. [42]

1.4. Magnetic interaction

1.4.1. Exchange interaction

The principal exchange mechanism for both ferromagnetic and antiferromagnetic metals includes the overlap of the partly localized atomic orbitals of adjacent atoms. [43] Besides, other interactions include the localized and delocalized electrons in mental, the purely delocalized electrons are also be involved. In 3*d* metals, extended wave functions and a spin-polarized local density of states were used to describe the electrons. Using the one-electron *d* wave functions, rather than the free-electron waves is more appropriate to describe them. In the tight-binding model, the overlap of the one-electron wave functions is small and the electrons remain mostly localized on the atoms. The model Hamiltonian is

$$\mathcal{H} = \sum_{ij} t_{ij} c_i^{\dagger} c_j$$

where the sum is the conduction band in terms of the electron creation and annihilation operators $c^{\dagger}$ and c. Usually considering the nearest-neighbor interactions and transfer integral

$t_{ij} = t$. Considering in a generally half-filled band is antiferromagnetic that the energy acquires related to letting the wave capacities grow onto adjoining destinations is possibly accomplished when the neighbors are antiparallel, leaving unfilled $\uparrow$ orbitals on the adjoining locales to move into. The nearly filled or empty bands tend to be ferromagnetic, because of the same spin when electrons hop into empty states. This can explain the phenomena why chromium and manganese are antiferromagnetic, but iron, cobalt, and nickel are ferromagnetic.

1.4.2. Superexchange

The electrons in insulators are localized, such as the oxides compounds. In transition-mental oxides, there are the 3*d*-orbitals hybridized with the oxygen 2*p*-orbitals rather than the 3*d*–3*d* overlap direct interaction. The "superexchange" interaction [44] transmit by the oxygen bridges, [27] described by the Heisenberg Hamiltonian. **Figure 1.8.** shows a typical superexchange bond. In the situation that a singly electron occupied 3*d*-orbital or a half-filled *d* shell (Fe^{3+}, Mn^{2+}), the energy of (b) is lower than that (a), the reason is that both electrons in oxygen 2*p*-orbital can easily spread out into the unoccupied 3*d*-orbitals. The superexchange interaction $\mathcal{J}$ involves both simultaneous virtual transfer of two electrons with the instantaneous formation of a $3d^{n+1}2p^5$ excited state and the interaction of order $-2t^2/U$, where *t* is the *p*–*d* transfer integral and *U* is the on-site 3*d* Coulomb interaction. $\mathcal{J}$ is sensitively on both the interatomic separation and the M–O–M bond angle.

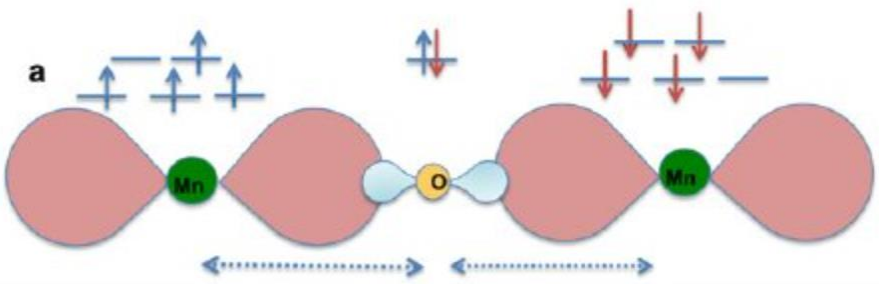

Figure 1.8. Superexchange interaction favoring AFM coupling. [45]

1.4.3. Double exchange

Double exchange arises including 3*d* ions which have both localized and delocalized *d* electrons. Different from the ferromagnetic superexchange, mixed-valence configurations are required, which are actually in any metal. Unlike the normal metal, the number of configurations was required just two. For example, $(La_{0.7}Ca_{0.3})MnO_3$, a double-exchange material, which has both $Mn^{4+}$and Mn^{3+} ions (d^3 and d^4) stays on the octahedral sites. By the charge states of the other ions in a compound, La^{3+}, Ca^{2+}, and O^{2-}, the two Mn valence states are imposed. Both octahedral coordination of d^3core electrons is kept in the narrow $t_{2g}^{\uparrow}$ band. However, the fourth *d* electron localized in $e_g^{\uparrow}$ the band. [46, 51] **Figure 1.9.**

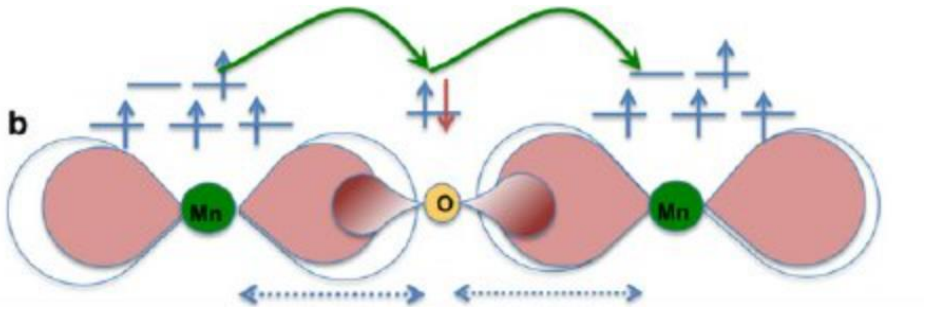

Figure 1.9. Double exchange interaction favoring FM coupling between the Mn ions, which is mediated via the O ion lying in between.[45]

1.5. Micromagnetism, domains, and applications.

1.5.1. Micromagnetic energy

The fundamental reason for micro-magnetism is that a magnet is a mesoscopic consistent medium where atomic-scale construction can be overlooked: ***M***(***r***) and ***Hd*** (***r***) are the most nonuniform, yet continuously changing functions of ***r***. ***M***(***r***) differs in direction: it can compare with the spontaneous magnetization ***Ms***. Domains like to form in the lowest-energy state of ferromagnetic or ferrimagnetic samples, to minimize the system total self-energy, which can be demonstrated as the formula:

$$\varepsilon_d = -\frac{1}{2}\int \mu_0 \mathbf{H}_d \cdot \mathbf{M} \mathrm{d}^3 r$$

Energy minimization is dependent upon limitations forced by exchange, anisotropy, and magnetostriction. The domain structure will disappear when a big enough field is applied. And the underlying spontaneous magnetization of the ferromagnet can be reformed. When reducing the field, the new domain structure a hysteresis can be formed again, shown in **Figure 1.10.** The hysteretic response of the ferromagnet, not only depends on the current situation but also connects with previous behavior, which is the magnets memory.

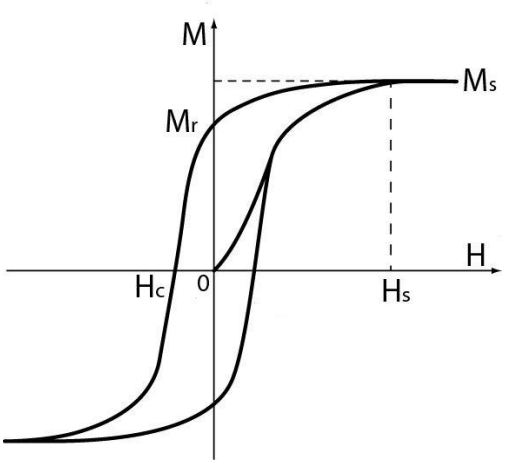

Figure 1.10. The hysteresis loop of a ferromagnet. Initially in an unmagnetized, virgin state. Magnetization appears as an imposed magnetic field *H*, modifies and eventually eliminates the microstructure of ferromagnetic domains magnetized in different directions, to reveal the spontaneous magnetization M_s. The remanence M_r which remains when the applied field is restored to zero, and the coercivity H_c, which is the reverse field needed to reduce the magnetization to zero, are marked on the loop.

1.5.2. Domain theory

Domain theory is an endeavor to lessen the intricacy of the magnetic energy, which assumes the large uniform magnetization area exists in the macroscopic sample. That area can be divided by the planar regions, the domain walls, where the magnetization can easily rotate

from one direction to another. The model is supported under the domain observed. If the domain exists, then there will be so many domain walls. The net magnetization can be changed by the applied field, which can move the domain wall or making the magnetization rotate towards the same direction. The magnetostatic energy base on the wall positions and the domain orientations. Domain theory destroys weak magnetic materials, especially in thin-film elements, in which the demagnetizing field is so small. Therefore, industries prefer states with the continuous rotation of magnetization to the domains.

1.5.3. Applications of magnets

Temporary magnets mainly are used to make magnetic flux produced by the circulating currents or permanent magnets. A huge number of huge electrical sheet steel are utilized each year in electromagnetic apparatus such as transformers, motors, and generators. Various elaborate components in magnetic circuits are produced using nickel-iron alloys, which offer alluring blends of penetrability, polarization, and resistivity. Protecting ferrites are especially appropriate for high-frequency applications, for example, power supplies, gags, and radio wires, and for microwave gadgets.

Permanent magnets convey attractive transitions into a region of space like the air gap, which is on extra energy. Hard ferrite and rare-earth magnets suit to produce flux densities that are comparable to their spontaneous polarization $\boldsymbol{J_s}$. Applications depend on the origin of flux distribution, including static or time-dependent, as well as the nonuniform or spatially uniform. What's more, the physical effect, force, torque, induced emf, Zeeman splitting, magnetoresistance, are also be discussed in applications. In reality, permanent magnets most are applied in electric motors, generators, and actuators. From the microwatts of wristwatch motors to the kilowatts of industrial drives, permanent magnets can all achieve the requirements. So many consumer applications from motors are made every year.

1.6. Quadruple perovskites of A-site ordered structure

1.6.1. Expected compositions of $A_2A'A''B_4O_{12}$

The $A''O_4$ tetrahedral site is exceptional in $A_2A'A''B_4O_{12}$. Cations that can occupy a tetrahedral coordination environment and their ionic radii. [48] Cu^{2+}, $Fe^{2+}$and Mn^{2+} were found so far in the A″ site of $A_2A'A''B_4O_{12}$ and they presumably unintentionally cover with cations found at the A′ site (**Figure. 1.11.**). The charge and size of Co^{2+}, Mg^{2+}, and Zn^{2+}, for instance, are near those of Cu^{2+}, $Fe^{2+}$and Mn^{2+}, yet they would like to ideally possess the tetrahedral A″ site rather than the square-planar A′ site. [49] On the other hand, nonetheless, all cations can stay at octahedral coordination, and some of them (e.g., Ni^{2+}, Sn^{4+}, and Ti^{4+}) present an exceptional inclination for such an environment. [48] Therefore, strong competitions with the octahedral B position or the arrangement of different phases where such cations have octahedral coordination are conceivable. One technique to constrain them into the A″ site is to utilize cations at the B locales with a considerably more inclination for octahedral conditions (like $NiCr_2O_4$ and Cu Cr_2O_4 spinels). We can choose that with enough high pressing factors during the sintering a few components (like Cu^{2+}, Fe^{2+} and Mn^{2+}) can be balanced at the A″ site. For instance, 5 GPa was sufficient to keep Fe^{2+} in the square-planar A′ site of $CaFe_3Ti_4O_{12}$, while more than 12 GPa was needed to make $CaFeTi_2O_6$ with Fe^{2+} in both the square-planar A′ and tetrahedral A″ sites. [9]

The appears of the A″ site gives an extra level of opportunity in $A_2A'A''B_4O_{12}$, and the quantity of components that can have tetrahedral coordination is bigger than that with a square-planar climate (**Figure. 1.11.**). Thus, it is normal that $A_2A'A''B_4O_{12}$ perovskites must be various and flexible.

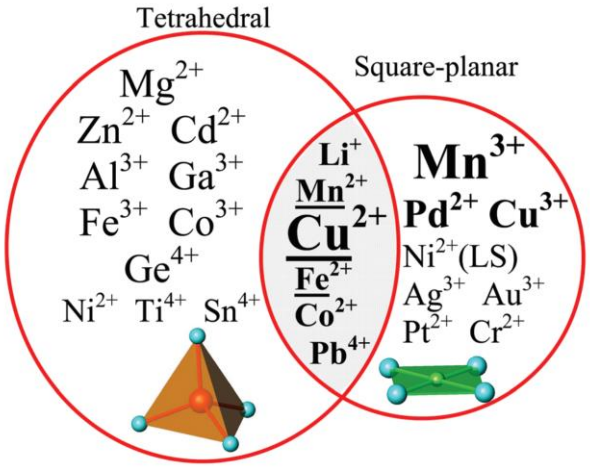

Figure 1.11. A schematic figure with some cations that can have tetrahedral coordination and square-planar coordination in oxides and their overlap.[4]

1.6.2. Known distortions

The parent design of $AA'_3B_4O_{12}$ belongs to the space group *Im*–3 (No. 204). All twists from the immediate gathering subgroup relations are experimentally achieved (not including the same *Im*–3 symmetry with $6a_p \times 6a_p \times 6a_p$) (**Figure. 1.12.**). These contortions are exemplified in $CaCu_3Ti_4O_{12}$ (the parent structure),[15 50] $CaCu_3Ga_2Sb_2O_{12}$, [51] $Ce_{0.5}Cu_3Ti_4O_{12}$, [52] $(Li_{1.333}Cu_{1.333})Nb_4O_{12}$, [53] $CaCu_3Fe_4O_{12}$, [8 54] $A^{2+}Mn_7O_{12}$ (A = Cd, Ca, Sr and Pb) [55, 56] and $BiCu_{0.2}Mn_{6.8}O_{12}$. [16] Most of these contortions are temperature-driven, that is, they are seen on cooling for a specific structure, and there exists a high-temperature parent adjustment. Notwithstanding, there are a couple of composition-driven distortions, that is, they are controlled by a specific organization and replace during the synthesis. [55, 56]

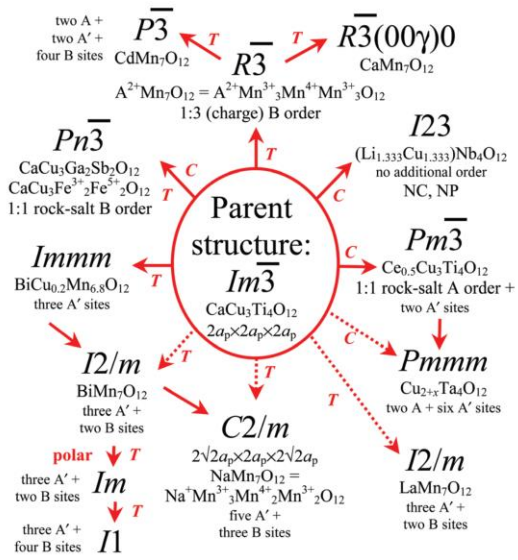

Figure 1.12. A schematic diagram of all direct group–subgroup distortions and other known distortions of the parent structure of $AA'_3B_4O_{12}$ quadruple perovskites (space group *Im*–3).[4]

The parent design of $A_2A'A''B_4O_{12}$ has the space bunch $P4_2/nmc$ (No. 137). There are seven twists from the immediate gathering subgroup relations (not including the same $P4_2/nmc$ symmetry with $2a_p \times 2a_p \times 6a_p$ and $6a_p \times 6a_p \times 2a_p$) (**Figure 1.13.**). Three of them have effectively been found experimentally. Surprisingly, a temperature-driven legitimate polar bending happens in $CaMnTi_2O_6$ with no impacts of single-electron pairs.[21]This is a very encouraging fact in correlation with the $AA'_3B_4O_{12}$ family.

Figure 1.13. A schematic diagram of all direct group–subgroup distortions of the parent structure of $A_2A'A''B_4O_{12}$ quadruple perovskites (space group $P4_2/nmc$). [4]

1.7. Objectives of this thesis

In the perovskites with R_2O_3 (R = rare-earth elements and Y) and Mn_2O_3 system, two large groups have been widely researched. One is $RMnO_3$ such as $TbMnO_3$ which exhibits multiferroicity. [57] The other one is RMn_7O_{12} like $LaMn_7O_{12}$ which has a C-type structure made up of ferromagnetically coupled antiferromagnetic planes. [58] $BiMn_7O_{12}$ is the polar distortions.[59-61] $HgMn_7O_{12}$ and $PbMn_7O_{12}$ both have new magnetic properties. [62,63]

One of A-site columnar-ordered quadruple perovskites $CaMnTi_2O_6$ [64] has a ferroelectric transition at 630 K, a long-range antiferromagnetic transition at 10 K, and switchable polarization at room temperature. [65,66] Its physical properties are very fascinating. Another member of A-site columnar-ordered quadruple perovskites, $Y_2MnMnMn_4O_{12}$, also presents the magnetic and physical properties are attractive. [67] RMn_3O_6 illustrate complex magnetic behaviors with some magnetic transition temperature, [62] spin-flop transitions, [68] and counterintuitive magnetic structures. [68] I would like to study the Mn-based perovskite materials with triple A-site ordering. A-site columnar-ordered quadruple perovskites can exhibit complex magnetic behaviors if magnetic cations are introduced into the B sites in addition to the A sites.[69,70]

In my works, all compounds were synthesized from MnO_x, R_2O_3 (rare-earth element and Y), under high-pressure and high-temperature conditions for about 2 hours. Three series compounds of Mn-based A-site columnar-ordered quadruple perovskite were introduced.

1.7.1. $A_2A'A''B_4O_{12}$ perovskites: $Y_2MnGa(Mn_{4-x}Ga_x)O_{12}$

To make a new spin-glass perovskites structure successfully, I chose the Mn_2O_3, Y_2O_3,

and Ga_2O_3 as the start powders. After annealing put all powders together and grind enough. Then put them into an Au capsule to make an experimental cell for 2 hours under high pressure and high temperature. Finally A-site columnar-requested fourfold perovskites $Y_2MnGa(Mn_{4-x}Ga_x)O_{12}$ with x = 0, 1, 2, and 3 were got. Through the XRD, and magnetic measurements I found all samples are as expected. Ga and Mn prefer different A and B sites. Details will present in chapter 3.

1.7.2. $A_2A'A''B_4O_{12}$ perovskites: $R_2MnMn(MnTi_3)O_{12}$

One of $A_2A'A''B_4O_{12}$ perovskites compounds, $R_2MnMn(MnTi_3)O_{12}$ (R = Nd, Eu, and Gd), originated from stoichiometric mixtures of MnO and commercial TiO_2 (99.9%) and R_2O_3 (99.9%). Final samples were successful *via* the high pressure and high temperature, which present an interesting phenomenon on magnetic behaviors and other aspects. Crystal structure and physical properties will be discussed in chapter 4.

1.7.3. $A_2A'A''B_4O_{12}$ perovskites: $NaRMn_2Ti_4O_{12}$

ABO_3 perovskites compound containing Ti at the octahedral B sites have important applications in modern technologies. In this part, we select different rare-earth elements to make $NaRMn_2Ti_4O_{12}$ (R = Sm, Eu, Gd, Dy) materials. Under the 6 GPa and high temperature for 2 hours, all samples were succeeded. Then I measured samples' XRD date and also calculate other physical properties. The conclusions for those samples discussions in chapter 5.

References in chapter 1

1. Giaquinta, D. M.; Zur Loye, H.-C., Structural predictions in the ABO_3 phase diagram. *Chem. Mater.* **1994,** *6* (4), 365-372.
2. Mitchell, R. H., *Perovskites: modern and ancient*. Almaz Press Thunder Bay, 2002, Ontario, Canada.
3. King, G.; Woodward, P. M., Cation ordering in perovskites. *J. Mater. Chem.* **2010,** *20* (28), 5785-5796.
4. Belik, A. A., Rise of A-site columnar-ordered $A_2A'A''B_4O_{12}$ quadruple perovskites with intrinsic triple order. *Dalton Transactions* **2018,** *47* (10), 3209-3217.
5. Goldschmidt, V. M., Die gesetze der krystallochemie. *Naturwissenschaften* **1926,** *14* (21), 477-485.
6. Glazer, A.; Ahtee, M.; Megaw, H., *Acta Crystallogr., Sect. A: Cryst. Phys., Diffr., Theor. Gen. Crystallogr*. **1975**, *31*,756-762
7. Vasil'ev, A.; Volkova, O., New functional materials $AC_3B_4O_{12}$. *Low Temperature Physics* **2007,** *33* (11), 895-914.
8. Yamada, I., High-pressure synthesis, electronic states, and structure–property relationships of perovskite oxides, $ACu_3Fe_4O_{12}$ (A: divalent alkaline earth or trivalent rare-earth ion). *J. Ceram. Soc. Jpn.* **2014,** *122* (1430), 846-851.
9. Leinenweber, K.; Linton, J.; Navrotsky, A.; Fei, Y.; Parise, J., High-pressure perovskites on the join $CaTiO_3$-$FeTiO_3$. *Phys. Chem. Miner.* **1995,** *22* (4), 251-258.
10. Linton, J.; Navrotsky, A.; Fei, Y., The Thermodynamics of Ordered Perovskites on the $CaTiO_3$-$FeTiO_3$ Join. *Phys. Chem. Miner.* **1998,** *25* (8), 591-596.
11. Ovsyannikov, S. V.; Zainulin, Y. G.; Kadyrova, N. I.; Tyutyunnik, A. P.; Semenova, A. S.; Kasinathan, D.; Tsirlin, A. A.; Miyajima, N.; Karkin, A. E., New

antiferromagnetic perovskite $CaCo_3V_4O_{12}$ prepared at high-pressure and high-temperature conditions. *Inorg. Chem.* **2013,** *52* (20), 11703-11710.

12. Shiro, K.; Yamada, I.; Ikeda, N.; Ohgushi, K.; Mizumaki, M.; Takahashi, R.; Nishiyama, N.; Inoue, T.; Irifune, T., Pd^{2+}-Incorporated Perovskite $CaPd_3B_4O_{12}$(B= Ti, V). *Inorg. Chem.* **2013,** *52* (3), 1604-1609.
13. Sakai, Y.; Yang, J.; Yu, R.; Hojo, H.; Yamada, I.; Miao, P.; Lee, S.; Torii, S.; Kamiyama, T.; Lezaic, M., A-Site and B-site Charge Orderings in an s–d Level Controlled Perovskite Oxide $PbCoO_3$. *J. Am. Chem. Soc.* **2017,** *139* (12), 4574-4581.
14. Shimura, G.; Shirako, Y.; Niwa, K.; Hasegawa, M., High-pressure synthesis and relationship between A-site ordering and local structure of multicomponent perovskites $(Ln_{0.25}Mn_{0.75})(Al_{0.25}Ti_{0.75})O_3$, Ln= La, Pr, Nd, Sm, Gd, Tb, Dy, Y. *J. Solid State Chem.* **2016,** *242*, 55-62.
15. Deschanvres, A.; Raveau, B.; Tollemer, F., Substitution of copper for a divalent metal in perovskite-type titanates. *Bull. Soc. Chim. Fr* **1967,** *11*, 4077-4078.
16. Belik, A. A.; Matsushita, Y.; Khalyavin, D. D., Reentrant structural transitions and collapse of charge and orbital orders in quadruple perovskites. *Angew. Chem. Int. Ed.* **2017,** *56* (35), 10423-10427.
17. Yamada, I., Novel catalytic properties of quadruple perovskites. *Science and Technology of advanced MaTerialS* **2017,** *18* (1), 541-548.
18. Shimura, G.; Niwa, K.; Shirako, Y.; Hasegawa, M., High - Pressure Synthesis and Magnetic Behavior of A - Site Columnar - Ordered Double Perovskites, $LnMn(Ga_{0.5}Ti_{0.5})_2O_6$ (Ln= Sm, Gd). *Eur. J. Inorg. Chem.* **2017,** *2017* (4), 835-839.
19. Leinenweber, K.; Parise, J., High-pressure synthesis and crystal structure of $CaFeTi_2O_6$, a new perovskite structure type. *J. Solid State Chem.* **1995,** *114* (1), 277-281.

20. Yao, N.; Navrotsky, A.; Keinenweber, K., Convergent Beam Electron Diffraction and High Resolution Electron Microscopy of $CaFeTi_2O_6$ Perovskite. *J. Solid State Chem.* **1996,** *123* (1), 73-82.
21. Liu, R.; Tanaka, M.; Mori, H.; Inaguma, Y.; Yamaura, K.; Belik, A. A., Ferrimagnetic and relaxor ferroelectric properties of $R_2MnMn(MnTi_3)O_{12}$ perovskites with R= Nd, Eu, and Gd. *J. Mater. Chem. C* **2021,** *9* (3), 947-956.
22. Solana-Madruga, E.; Arévalo-López, Á. M.; Dos Santos-García, A. J.; Urones-Garrote, E.; Ávila-Brande, D.; Sáez-Puche, R.; Attfield, J. P., Double Double Cation Order in the High-Pressure Perovskites $MnRMnSbO_6$. *Angew. Chem. Int. Ed.* **2016,** *55* (32), 9340-9344.
23. Zhang, L.; Matsushita, Y.; Yamaura, K.; Belik, A. A., Five-Fold Ordering in High-Pressure Perovskites RMn_3O_6 (R= Gd–Tm and Y). *Inorg. Chem.* **2017,** *56* (9), 5210-5218.
24. McNally, G. M.; Arévalo-López, Á. M.; Kearins, P.; Orlandi, F.; Manuel, P.; Attfield, J. P., Complex Ferrimagnetism and Magnetoresistance Switching in Ca-Based Double Double and Triple Double Perovskites. *Chem. Mater.* **2017,** *29* (20), 8870-8874.
25. Cotton, F. A.; Wilkinson, G.; Murillo, C. A.; Bochmann, M.; Grimes, R., *Advanced inorganic chemistry*. Wiley New York: **1988**; Vol. 6.
26. O'handley, R. C., *Modern magnetic materials: principles and applications*. Wiley: **2000**.
27. West, A. R., *Solid state chemistry and its applications*. John Wiley & Sons: **2014**.
28. Miller, A., Landolt-bornstein: Numerical data and functional relationships in science and technology. *Optica Acta: International Journal of Optics* **1985,** *32* (5), 507-508.
29. Koshibae, W.; Kawamura, Y.; Ishihara, S.; Okamoto, S.; Inoue, J.-i.; Maekawa, S., Interplay of spin and orbital orderings in perovskite manganites. *J. Phys. Soc. Jpn.* **1997,** *66* (4), 957-960.

30. Kittle, C., Introduction to Solid State Physics, John Willey and Sons Inc., UK. **2005**.

31. Miessler G. L and T. D.A., Inorganic Chemistry. **2004**: Pearson Education.

32. Tokura, Y. and N. Nagaosa, Orbital physics in transition-metal oxides. Science, **2000**. 288(5465), 462-468.

33. Vallin, J. T.; Watkins, G. D., The Jahn-teller effect for Cr^{2+} in II–VI crystals. *Solid State Commun.* **1971,** *9* (13), 953-956.

34. Alonso, J.; Martinez-Lope, M.; Casais, M.; Fernandez-Diaz, M., Evolution of the Jahn− Teller distortion of MnO_6 octahedra in $RMnO_3$ perovskites (R= Pr, Nd, Dy, Tb, Ho, Er, Y): a neutron diffraction study. *Inorg. Chem.* **2000,** *39* (5), 917-923.

35. Lufaso, M. W.; Gemmill, W. R.; Mugavero III, S. J.; Kim, S.-J.; Lee, Y.; Vogt, T.; zur Loye, H.-C., Synthesis, structure, magnetic properties and structural distortion under high pressure of a new osmate, Sr_2CuOsO_6. *J. Solid State Chem.* **2008,** *181* (3), 623-627.

36. Attfield, M.; Battle, P.; Bollen, S.; Kim, S.; Powell, A.; Workman, M., Structural and electrical studies of mixed copper/ruthenium oxides and related compounds of zinc and antimony. *J. Solid State Chem.* **1992,** *96* (2), 344-359.

37. Tokura, Y.; Nagaosa, N., Orbital physics in transition-metal oxides. *Science* **2000,** *288* (5465), 462-468.

38. Rodríguez, E.; López, M. L.; Campo, J.; Veiga, M. L.; Pico, C., Crystal and magnetic structure of the perovskites La_2MTiO_6 (M= Co, Ni). *J. Mater. Chem.* **2002,** *12* (9), 2798-2802.

39. Baettig, P.; Seshadri, R.; Spaldin, N. A., Anti-polarity in ideal $BiMnO_3$. *J. Am. Chem. Soc.* **2007,** *129* (32), 9854-9855.

40. Azuma, M.; Carlsson, S.; Rodgers, J.; Tucker, M. G.; Tsujimoto, M.; Ishiwata, S.; Isoda, S.; Shimakawa, Y.; Takano, M.; Attfield, J. P., Pressure-induced intermetallic valence transition in $BiNiO_3$. *J. Am. Chem. Soc.* **2007,** *129* (46), 14433-14436.

41. Viola, M. d. C.; Martinez-Lope, M.; Alonso, J.; Velasco, P.; Martinez, J.; Pedregosa, J.; Carbonio, R.; Fernández-Díaz, M., Induction of colossal magnetoresistance in the double perovskite Sr_2CoMoO_6. *Chem. Mater.* **2002,** *14* (2), 812-818.
42. Liao, Y., Practical electron microscopy and database. An Online Book 2006.
43. Blundell, S., Magnetism in condensed matter: oxford master series. *Condensed Matter Physics (Oxford Series Publications, 2001)* **2001**, 29.
44. Kittel, C.; McEuen, P.; McEuen, P., *Introduction to solid state physics*. Wiley New York: **1996**; Vol. 8.
45. Panigrahi, P.; Araujo, C. M.; Hussen, T.; Ahuja, R., Crafting ferromagnetism in Mn-doped MgO surfaces with p-type defects. Science and technology of advanced materials **2014**.
46. Bhaskar, A.; Liu, C.-J.; Yuan, J.; Chang, C.-L., Thermoelectric properties of n-type $Ca_{1-x}Bi_xMn_{1-y}Si_yO_{3-\delta}$ (x= y= 0.00, 0.02, 0.03, 0.04, and 0.05) system. *J. Alloys Compd.* **2013,** *552*, 236-239.
47. Raveau, B.; Zhao, Y.; Martin, C.; Hervieu, M.; Maignan, A., Mn-site doped $CaMnO_3$: creation of the CMR effect. *J. Solid State Chem.* **2000,** *149* (1), 203-207.
48. Shannon, R., Acta Crystallogr., Sect. A: Cryst. Phys., Diffr., Theor. Gen. Crystallogr. **1976**.
49. Waroquiers, D.; Gonze, X.; Rignanese, G.-M.; Welker-Nieuwoudt, C.; Rosowski, F.; Göbel, M.; Schenk, S.; Degelmann, P.; André, R.; Glaum, R., Statistical analysis of coordination environments in oxides. *Chem. Mater.* **2017,** *29* (19), 8346-8360.
50. Subramanian, M.; Li, D.; Duan, N.; Reisner, B.; Sleight, A., High dielectric constant in $ACu_3Ti_4O_{12}$ and $ACu_3Ti_3FeO_{12}$ phases. *J. Solid State Chem.* **2000,** *151* (2), 323-325.
51. Byeon, S.-H.; Lufaso, M. W.; Parise, J. B.; Woodward, P. M.; Hansen, T., High-pressure synthesis and characterization of perovskites with simultaneous ordering of

both the A-and B-site cations, $CaCu_3Ga_2M_2O_{12}$ (M= Sb, Ta). *Chem. Mater.* **2003,** *15* (20), 3798-3804.

52. Saito, T.; Yamada, R.; Ritter, C.; Senn, M. S.; Attfield, J. P.; Shimakawa, Y., Control of L-type ferrimagnetism by the Ce/vacancy ordering in the A-site-ordered perovskite $Ce_{1/2}Cu_3Ti_4O_{12}$. *Inorg. Chem.* **2014,** *53* (3), 1578-1584.
53. Sato, M.; Hama, Y., Structure of new perovskite-related compounds, $LiCuM_3O_9$(M= Nb, Ta). *J. Mater. Chem.* **1993,** *3* (3), 233-236.
54. Yamada, I.; Murakami, M.; Hayashi, N.; Mori, S., Inverse charge transfer in the Quadruple Perovskite $CaCu_3Fe_4O_{12}$. *Inorg. Chem.* **2016,** *55* (4), 1715-1719.
55. Glazkova, Y. S.; Terada, N.; Matsushita, Y.; Katsuya, Y.; Tanaka, M.; Sobolev, A. V.; Presniakov, I. A.; Belik, A. A., High-pressure synthesis, crystal structures, and properties of $CdMn_7O_{12}$ and $SrMn_7O_{12}$ perovskites. *Inorg. Chem.* **2015,** *54* (18), 9081-9091.
56. Belik, A. A.; Glazkova, Y. S.; Katsuya, Y.; Tanaka, M.; Sobolev, A. V.; Presniakov, I. A., Low-Temperature Structural Modulations in $CdMn_7O_{12}$, $CaMn_7O_{12}$, $SrMn_7O_{12}$, and $PbMn_7O_{12}$ Perovskites Studied by Synchrotron X-ray Powder Diffraction and Mossbauer Spectroscopy. *The Journal of Physical Chemistry C* **2016,** *120* (15), 8278-8288.
57. Matsubara, M.; Manz, S.; Mochizuki, M.; Kubacka, T.; Iyama, A.; Aliouane, N.; Kimura, T.; Johnson, S. L.; Meier, D.; Fiebig, M. Magnetoelectric domain control in multiferroic $TbMnO_3$. *Science* **2015**, *348*, 1112-1115.
58. Prodi, A.; Gilioli, E.; Cabassi, R.; Bolzoni, F.; Licci, F.; Huang, Q.; Lynn, J. W.; Affronte, M.; Gauzzi, A.; Marezio, M. Magnetic structure of the high-density single-valent e_g Jahn-Teller system $LaMn_7O_{12}$. *Phys. Rev. B* **2009**, *79*, 085105.

59. Itoh, M.; Wang, R.; Inaguma, Y.; Yamaguchi, T.; Shan, Y.; Nakamura, T., Ferroelectricity induced by oxygen isotope exchange in strontium titanate perovskite. *Phys. Rev. Lett*. **1999**, *82* (17), 3540.

60. Jang, H.; Kumar, A.; Denev, S.; Biegalski, M. D.; Maksymovych, P.; Bark, C.; Nelson, C. T.; Folkman, C.; Baek, S. H.; Balke, N., Ferroelectricity in strain-free $SrTiO_3$ thin films. *Phys. Rev. Lett.* **2010**, *104* (19), 197601.

61. Taniguchi, H.; Shan, Y. J.; Mori, H.; Itoh, M., Critical soft-mode dynamics and unusual anticrossing in $CdTiO_3$ studied by Raman scattering. *Phys. Rev. B* **2007**, *76* (21), 212103.

62. W.-T. Chen, C.-W. Wang, H.-C. Wu, F.-C. Chou, H.-D. Yang, A. Simonov and M. S. Senn, Improper ferroelectric polarization in a perovskite driven by intersite charge transfer and ordering, Phys. Rev. B: Condens. *Matter Mater. Phys.*, **2018**, *97*, 144102.

63. A. A. Belik, Y. S. Glazkova, Y. Katsuya, M. Tanaka, A. V. Sobolev and I. A. Presniakov, Low-temperature structural modulations in $CdMn_7O_{12}$, $CaMn_7O_{12}$, $SrMn_7O_{12}$, and $PbMn_7O_{12}$ perovskites studied by synchrotron X-ray powder diffraction and Mossbauer spectroscopy, *J. Phys. Chem. C*, **2016**, *120*, 8278–8288.

64. Belik, A. A., Rise of A-site columnar-ordered $A_2A'A''B_4O_{12}$ quadruple perovskites with intrinsic triple order. *Dalton Transactions* **2018,** *47* (10), 3209-3217.

65. Aimi, A.; Mori, D.; Hiraki, K.-i.; Takahashi, T.; Shan, Y. J.; Shirako, Y.; Zhou, J.; Inaguma, Y., High-Pressure Synthesis of A-Site Ordered Double Perovskite $CaMnTi_2O_6$ and Ferroelectricity Driven by Coupling of A-Site Ordering and the Second-Order Jahn–Teller Effect. *Chem. Mater.* **2014,** *26* (8), 2601-2608.

66. Li, Z.; Cho, Y.; Li, X.; Li, X.; Aimi, A.; Inaguma, Y.; Alonso, J. A.; Fernandez-Diaz, M. T.; Yan, J.; Downer, M. C., New Mechanism for Ferroelectricity in the Perovskite Ca_{2-}

$_x$Mn$_x$Ti$_2$O$_6$ Synthesized by Spark Plasma Sintering. *J. Am. Chem. Soc.* **2018,** *140* (6), 2214-2220.

67. Zhang, L.; Matsushita, Y.; Yamaura, K.; Belik, A. A., Five-Fold Ordering in High-Pressure Perovskites RMn_3O_6(R= Gd–Tm and Y). *Inorg. Chem.* **2017,** *56* (9), 5210-5218.

68. Vibhakar, A.; Khalyavin, D.; Manuel, P.; Zhang, L.; Yamaura, K.; Radaelli, P.; Belik, A.; Johnson, R., Magnetic structure and spin-flop transition in the A-site columnar-ordered quadruple perovskite $TmMn_3O_6$. *Phys. Rev. B* **2019,** *99* (10), 104424.

69. A. M. Vibhakar , D. D. Khalyavin, P. Manuel, J. Liu, A. A. Belik and R. D. Johnson, Spontaneous rotation of ferrimagnetism driven by antiferromagnetic spin canting, *Phys. Rev. Lett.*, **2020**, *124*, 127201.

70. A. A. Belik, L. Zhang, R. Liu, D. D. Khalyavin, Y. Katsuya, M. Tanaka and K. Yamaura, Valence variations by B-site doping in A-site columnar-ordered quadruple perovskites $Sm_2MnMn(Mn_{4-x}Ti_x)O_{12}$ with $1 \leqslant x \leqslant 3$, *Inorg. Chem.*, **2019**, *58*, 3492–3501.

Chapter 2. Experimental methods

The extreme conditions of high temperature and high pressure, as a special research environment, have an important position in many disciplines such as physics, chemistry, geology, and materials. Especially in physics and geology research, high temperature and high-pressure conditions are very important.

As we all know, under the conditions of high temperature and high pressure, the material's atomic/molecular distance will be shortened, electronic states overlap and interaction integration and other interaction expressions will be significantly enhanced. In particular, the inner electrons of the atom can partly participate in bonding to compete with the outer electrons. As everyone knows, solid-state physics treats materials as “ionic core + outer electron”, and the inner electron effect is hardly considered. However, under high-pressure conditions, bonding and inner electrons participate in the interaction, and the original structure of the material will be destroyed, resulting in a structural phase change. The state of electromagnetic interaction under high pressure will also change significantly, bringing more peculiar physical properties. For example, many famous superconducting materials are formed under high temperature and high-pressure conditions. [1-4]

At the same time, a lot of A-site columnar-ordered quadruple perovskites with complex magnetic properties have been synthesized successfully like RMn_3O_6 (R = Gd, Tm, and Y), [5] and $CeCuMn_6O_{12}$. [6]

The high-pressure method can effectively synthesize the crystal structure of perovskite, which not only saves sintering time but also enhance stability and density. Besides the approach is beneficial to form the ordered structure. In this work, all samples were fabricated under the 6 GPa and different high temperatures. Crystal structures, magnetic properties, and other

physical properties were studied. Using equipment such as X-ray diffraction (XRD), synchrotron X-ray powder diffraction, neutron powder diffraction, magnetic property measurement system (MPMS), physical property measurement system (PPMS), differential scanning calorimetry (DSC), and second-harmonic-generation (SHG) machine.

2.1. Sample synthesis: high-pressure method

In this thesis, all samples were prepared using the belt-type high-pressure apparatus (Kobe Steel, Ltd.). The pressure and temperature of the apparatus can achieve 8 GPa and 2000 ºC. Selecting the pyrophyllite cell can gain quasi-hydrostatic conditions when heating. [7] To get the high temperature, the graphite is selected as part of the furnace. The NaCl sleeve and cylindrical pieces protect the capsules and graphite from contact.

When prepared samples, the first step is to anneal the start powders, including the R_2O_3 (R = rare-earth elements and Y), MnO_x (Mn_3O_4, Mn_2O_3, MnO_2, MnO), to remove water. Then stoichiometric amounts of starting materials were mixed and ground thoroughly in air. Third, put the mixtures into Au or Pt capsules using a hand press and seal them. The last step, making the sample cell from the previous capsules and let them into the high-pressure apparatus for sintering, **Figure 2.1.** When the pressure increased slowly to be determined and stable, the heat process can start. Then kept the target temperature for 2 h. The pressure released also should be slowly.

Figure 2.1. High-pressure apparatus set in National Institute for Materials Science (NIMS).

2.2. X-ray diffraction

2.2.1. Powder X-ray diffraction

Powder X-ray diffraction (XRD) is a useful technique to preliminarily characterize phases and structures. Room temperature (RT) XRD data were collected from Desktop X-ray Diffractometer MiniFlex (Rigaku) (**Figure 2.2.**), which equipped a graphite monochromator and Cu Ka radiation (λ = 1.5418 Å) in 0.2° increments over the range 5°< 2θ<100° with a scanning rate of 5°/min. In this situation, the beam of electrons comes from the Cu 1*s* orbitals.

Figure 2.2. The picture of X-ray Diffractometer MiniFlex (Rigaku)

Using the Bragg's law: $n\lambda = 2d\sin\theta$, where n is an integer, λ is the wavelength of the incident wave, d is the perpendicular distance between pairs of adjacent planes, and θ is the scattering angle,[8] can analysis the XRD data. In this law, crystals can be considered as a semi-transparent mirror off which particular X-ray is reflected depending on deferent angle θ. A lot of crystal information can be got through the recording reflections.

2.2.2. Synchrotron X-ray diffraction

Synchrotron radiation is emitted when charged particles such as electrons, are accelerated radially, i.e. In 1947, synchrotron radiation was first observed. Synchrotron X-ray Diffraction (SXRD) is a very crucial technique to analyze unknown materials efficiently depending on their high energy. And the high-speed particles circulate in ultra-high vacuum tubes, or storage rings (simplified sketch, **Figure 2.3.**), which are made of a certain arrangement of magnets. The diameter of the storage ring may be hundreds of meters.

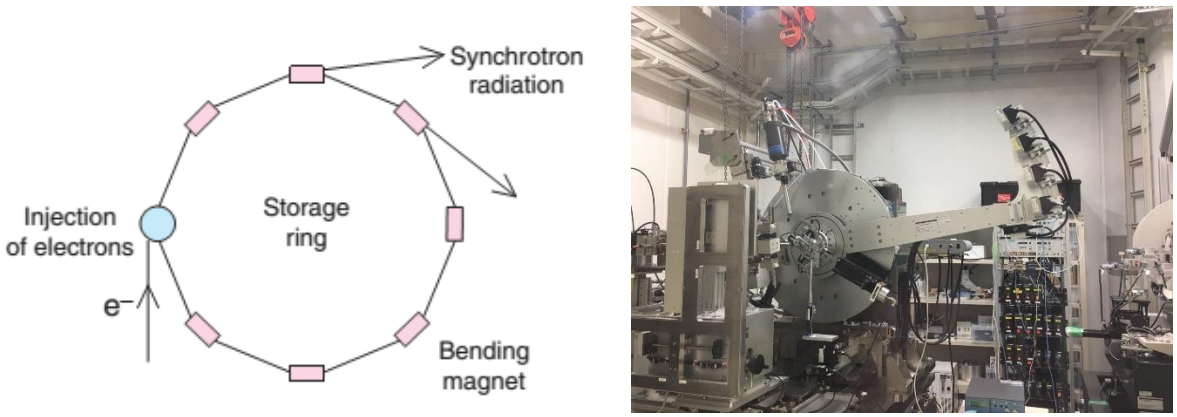

Figure 2.3. Schematic diagram of a synchrotron storage ring (left)[9] and a picture of BL15XU in Spring-8(right).

X-ray powder diffraction (XRPD) data were collected at RT on a RIGAKU MiniFlex600 diffractometer using CuKa radiation (2θ range of 8-140°, a step width of 0.02°, and a scan speed of 1°/min).

In this thesis, the synchrotron X-ray diffraction (SXRD) data were collected at room temperature (RT) on a large Debye–Scherrer camera at the undulator beamline BL15XU of SPring-8. [10,11] The intensity data were collected between 3° and 60.2° at 0.003° intervals in 2θ; the incident beam was monochromatized at l = 0.65298 Å. The samples were packed into Lindemann glass capillaries (inner diameter: 0.1 mm), which were rotated during measurements. Absorption coefficients were also measured for some samples. The Rietveld analysis was performed using the RIETAN-2000 program, [12–14] The impurities for some samples reported in this work were estimated from the refined scale factors by RIETAN-2000 after the Rietveld analysis of synchrotron XRPD data.

2.2.3. Neutron diffraction (NPD)

Neutron powder diffraction (NPD) is complementary to the synchrotron X-ray powder diffraction method, it is particularly useful for materials with light elements and magnetic structure analysis. Because of the weak absorption of neutrons, they can generalize information

on bulk materials and detect the lattice distortions and defects in a non-destructive way. In addition, neutrons possess spin ½ which provides the neutrons to interact with unpaired electrons, and consequently, neutrons are diffracted by both atomic nuclei and unpaired electrons. In this way, neutron powder diffraction can detect the magnetic structure with the priority of any other methods. [13] Rietveld refinements of the crystal and magnetic structures were performed using the FullProf program. [15]

2.3. Differential scanning calorimetry (DSC)

Differential scanning calorimetry (DSC) is a thermoanalytical technique, when the sample undergoes a phase change, glass transition, and chemical reaction, it will absorb and release heat, to keep the sample and reference temperature consistent. Therefore the difference in the amount of heat required to increase the temperature of the sample and reference is measured as a function of temperature can analyze the properties of the materials.

In this thesis, using a Mettler Toledo DSC1 STAR^e system to measure the DSC curves, as shown in **Figure 2.4.**

Figure 2.4. Image of the Mettler Toledo DSC1 STAR^e in NIMS Namiki-site.

2.4. Magnetic properties measurement system (MPMS)

The magnetic properties of all samples were measured by MPMS-XL-7T (Quantum Design) as shown in **Figure 2.5.** The temperature-dependent magnetic susceptibilities (χ) and field-dependent isothermal magnetizations of all prepared samples were measured. The temperature-dependent magnetic susceptibilities (χ) were measured under both field cooling (FC) and zero-field cooling (ZFC) conditions in a temperature range of 2 to 400 K under an applied magnetic field of 100 Oe and10 kOe. Initial negative magnetization on some ZFC curves could be caused by negative trapped fields inside a magnetometer or the sample insertion procedure. [16] The field dependence isothermal magnetizations were measured between +70 kOe and –70 kOe. The ac susceptibility was measured by using MPMS-1T (Quantum Design). The real parts (χ') and imaginary parts (χ'') were measured at different frequencies (f) and different applied oscillating magnetic fields (H_{ac}).

Figure 2.5. Image of the MPMS-XL in NIMS Namiki-site

2.5. Physical properties measurement system (PPMS)

Specific heat, C_p, can provide some information such as phase transition point, magnetic properties of materials, which refers to the energy that is required to heat up or cool down of an object for a certain temperature change. Specific heat measurements were carried out at 0 Oe, 70 kOe, and 90 kOe fields using a relaxation technique with a Physical Property Measurement System (PPMS, Quantum Design), as shown in **Figure 2.6.** Measurement temperature ranged from 2 to 300 K. A hand-pressed pellet of the sample was mounted on an aluminum plate with Apiezon N-Grease for better thermal contact. The calorimeter puck containing a sample-mounting platform is necessary for the measurement (**Figure 2.7.**).

Dielectric properties were measured using a NOVOCONTROL Alpha-A High-Performance Frequency Analyzer between 5–10 and 300–330 K on cooling and heating in the frequency range of 100 Hz and 2 MHz and at H = 0 and 90 kOe.

Figure 2.6. Image of the PPMS-7T in NIMS Namiki-site

Figure 2.7. Calorimeter puck for heat capacity measurement.

2.6. Other technologies used in this work.

2.6.1 P–E hysteresis loop measurements

Ferroelectric properties were evaluated by *P–E* hysteresis loop measurements using an aixACCT TF analyzer 2000 ferroelectric tester at frequencies of 0.02–2 Hz and liquid nitrogen temperature. The samples were, therefore, immersed in liquid nitrogen. No RT measurements were performed as conductivity at RT was too high to apply a high voltage of 8–9 kV. The same pellets with Ag electrodes as those used for dielectric and impedance measurements were used for *P–E* measurements. For different samples, Au electrodes also are prepared by Au sputtering and annealing at 573 K for several min in air, and the sample thickness was reduced compared with the Ag electrodes.

2.6.2 measurements second-harmonic-generation (SHG) measurements

Powder second-harmonic generation (SHG, also named frequency doubling) is a nonlinear optical phenomenon where two photons with the same frequency interact with a nonlinear material, will cause the result that generating a new photon with twice the energy of the initial photons, also means twice the frequency and half the wavelength, at the same time, can conserve the coherence of the excitation. This is a special optical process of sum-frequency

generation (2 photons), and a more effective way of harmonic generation.

All powder SHG measurements were performed at RT for all samples on a modified Kurtz [17] nonlinear optical system using 1064 nm light to check the presence or absence of centrosymmetry. For low-temperature measurements, the samples were put on a sample holder in a homemade cryostat and cooled using liquid nitrogen.

References in chapter 2

1. Drozdov, A.; Eremets, M.; Troyan, I.; Ksenofontov, V.; Shylin, S. I., Conventional superconductivity at 203 kelvin at high pressures in the sulfur hydride system. Nature **2015**, *525* (7567), 73-76.
2. Dias, R. P.; Silvera, I. F., Observation of the Wigner-Huntington transition to metallic hydrogen. Science **2017**, *355* (6326), 715-718.
3. Drozdov, A.; Kong, P.; Minkov, V.; Besedin, S.; Kuzovnikov, M.; Mozaffari, S.; Balicas, L.; Balakirev, F.; Graf, D.; Prakapenka, V., Superconductivity at 250 K in lanthanum hydride under high pressures. Nature **2019**, *569* (7757), 528-531.
4. Snider, E.; Dasenbrock-Gammon, N.; McBride, R.; Debessai, M.; Vindana, H.; Vencatasamy, K.; Lawler, K. V.; Salamat, A.; Dias, R. P., Room-temperature superconductivity in a carbonaceous sulfur hydride. Nature **2020**, *586* (7829), 373-377.
5. Zhang, L.; Matsushita, Y.; Yamaura, K.; Belik, A. A. Five-Fold Ordering in High-Pressure Perovskites RMn3O6 (R = Gd-Tm and Y). Inorg. Chem. **2017**, *56*, 5210-5218.
6. Zhang, L.; Matsushita, Y.; Katsuya, Y.; Tanaka, M.; Yamaura, K.; Belik, A. A. Charge and orbital orders and structural instability in high-pressue quadruple perovskite $CeCuMn_6O_{12}$. J. Phys.: Condens. Matter **2018**, *30*, 074003.
7. Fernández-Sanjulián, J.; E. Morán; Alario-Franco.M. Á.Synthesis, stability range and characterization of $Pr_2Cu_2O_5$.*High Pressure Research* **2010**, *30*(1), 159-166.
8. Baskaran, S. Structure and Regulation of Yeast Glycogen Synthase. **2010**, University of California, Berkeley.
9. West, A. R. Solid State Chemistry and its Application. **2014**, University of Sheffield, UK: Wiley.
10. Tanaka, M.; Katsuya, Y.; Yamamoto, A. A new large radius imaging plate camera for high-resolution and high-throughput synchrotron X-ray powder diffraction by

multiexposure method. Rev. Sci. Instrum. 2008, 79(7), 075106.

11. Tanaka, M.; Katsuya, Y.; Matsushita, Y.; Sakata, O., Development of a synchrotron powder diffractometer with a one-dimensional X-ray detector for analysis of advanced materials. *J. Ceram. Soc. Jpn.* **2013**, *121* (1411), 287-290.
12. Izumi, F.; Momma, K. Three-Dimensional Visualization in Powder Diffraction. *Solid State Phenomena,* **2007**, *130*, 15-20.
13. Izumi, F.; Asano, H.; Murata, H.; Watanabe, N. Rietveld analysis of powder patterns obtained by TOF neutron diffraction using cold neutron sources. *J. Appl. Cryst.* **1987**, *20*, 411-418.
14. Izumi, F.; Ikeda, T. In A rietveld-analysis programm RIETAN-98 and its applications to zeolites, *Mater. Sci. Forum, Trans Tech Publ*, **2000**,321-324, 198-205.
15. Rodríguez-Carvajal, J., Recent advances in magnetic structure determination by neutron powder diffraction. *Physica B* **1993**, *192* (1-2), 55-69.
16. Zhang, L.; Terada, N.; Johnson, R. D.; Khalyavin, D. D.; Manuel, P.; Katsuya, Y.; Tanaka, M.; Matsushita, Y.; Yamaura, K.; Belik, A. A., High-pressure synthesis, structures, and properties of trivalent A-site-ordered quadruple perovskites RMn_7O_{12} (R= Sm, Eu, Gd, and Tb). *Inorg. Chem.*, **2018**, *57* (10), 5987-5998.
17. S. K. Kurtz and T. T. Perry, A powder technique for the evaluation of nonlinear optical materials, *J. Appl. Phys.*, **1968**, *39*, 3798-3813.

Chapter 3. Spin-Glass Magnetic Properties of $Y_2MnGa(Mn_{4-x}Ga_x)O_{12}$ with $0 \leq x \leq 3$

3.1. Introduction

Perovskite manganites have provided a playground to study a complex interplay among charge, spin, and orbital degrees of freedom, and they exhibit many interesting and useful properties.[1,2] $CaMnO_3$-based compounds, for example, have been extensively studied as thermoelectric,[3] electrochemical,[4] catalytic,[5,] and multiferroic materials.[6] $RMnO_3$-based compounds, where R is a rare-earth element, show colossal magnetoresistance[1,7] and one of the largest spin-induced ferroelectric polarization values.[8] Doping effects on $AMnO_3$ have been intensively investigated.[1,2,7]

There are also perovskite manganites with the A-site ordered quadruple perovskite structure, $AA'_3B_4O_{12}$,[9] and a 1:7 composition. Their general formula is AMn_7O_{12} (=$AMn^{3+}{}_3Mn_4O_{12}$) with A = Na,10 Cd, Ca, Sr, Pb,[11,12] Hg,[13] Bi,[14] and R.[15−17] Depending on the charge of the A cations the average oxidation state of manganese at the perovskite B sites can change between +3 and +3.5, resulting in complex charge-, spin-, and orbital-order transitions[10,18] and the appearance of spin-induced ferroelectric polarization.[12,13,19,20] Good catalytic activity of AMn_7O_{12} manganites has recently been demonstrated.[21] Doped AMn_7O_{12} manganites show re-entrant structural transitions and other interesting structural properties.[22]

We recently found perovskite manganites with the A-site columnar-ordered quadruple perovskite structure having a general formula of $A_2A'A''B_4O_{12}$ [23] and a 1:3 composition (or close to 1 : 3). They are formula is RMn_3O_6 (=$A_2Mn^{3+}Mn^{2+}Mn_4O_{12}$) with A = R = Gd−Tm and Y.[24] In $A_2A'A''B_4O_{12}$, the A, A′, and A″ sites have 10-fold, square-planar, and tetrahedral coordination environments, respectively.[23] Therefore, in RMn_3O_6 with the manganese average oxidation state of +3, the tetrahedral A″ site is occupied by Mn^{2+}, as Mn^{3+} is not found in

tetrahedral coordination, and there is a mixed-valence state of manganese at the B sites. RMn_3O_6 demonstrates complex magnetic behaviors with several magnetic transition temperatures,[24] spin-flop transitions, [25] and counterintuitive magnetic structures.[25]

Therefore, in this work, we attempted to remove a mixed-valence state of manganese at the B sites by substituting Ga^{3+} for Mn^{2+} at the tetrahedral A″ site and we prepared $Y_2MnGa(Mn_{4-x}Ga_x)O_{12}$ solid solutions where all cations should have the +3 oxidation states in ideal cases. We found that for the x = 0 sample, the Ga/Mn ordering is not perfect with the determined cation and charge distributions as $[Y^{3+}{}_2]_A[Mn^{3+}]_{A'}[Ga^{3+}{}_{0.68}Mn^{2+}{}_{0.32}]_{A''}[Mn_{3.68}Ga_{0.32}]_BO_{12}$. But, a complete triple A-site order, $[Y^{3+}{}_2]_A[Mn^{3+}]_{A'}[Ga^{3+}]_{A''}[Mn^{3+}{}_{4-x}Ga_{3+x}]_BO_{12}$, is realized for $x \geqslant 1$. All solid solution members exhibit spin-glass (SG)-like magnetic properties due to the presence of Ga^{3+} at the octahedral B sites.

3.2. Experimental details of Chapter 3

$Y_2MnGa(Mn_{4-x}Ga_x)O_{12}$ solid solutions with x = 0, 1, 2, and 3 were prepared from stoichiometric mixtures of Mn_2O_3, Ga_2O_3(99.9%), and Y_2O_3 (99.9%) at 6 GPa and ∼1570 K for 2 h in Au capsules. After heat treatments, the samples were quenched to room temperature (RT), and the pressure was slowly released. All samples were highly friable. Single-phase Mn_2O_3 was prepared from commercial MnO_2 (99.99%) by heating in air at 923 K for 24 h.

X-ray powder diffraction (XRPD) data were collected at RT on a RIGAKU MiniFlex600 diffractometer using Cu Kα radiation (2θ range of 8−100°, a step width of 0.02°, and scan speed of 2°/min). Synchrotron XRPD data were measured at RT on a large Debye−Scherrer camera at the undulator beamline BL15XU of SPring-8.[26,27] The intensity data were collected between 2° and 60.23° at 0.003° intervals in 2θ; the incident beam was monochromatized at λ = 0.65298 Å. The samples were packed into Lindemann glass capillaries (inner diameter: 0.1 mm), which were rotated during measurements. Absorption coefficients were also measured.

The Rietveld analysis was performed using the RIETAN-2000 program.[28] Weight fractions of phases (wt %) reported in this work were estimated by RIETAN-2000 from the refined scale factors after the Rietveld analysis of synchrotron XRPD data.

Neutron powder diffraction data of $Y_2MnGa(Mn_3Ga)O_{12}$ were collected at the ISIS pulsed neutron and muon spallation source at the Rutherford Appleton Laboratory (UK), using the WISH diffractometer located at the second target station.[29] The sample (~1.36 g: samples from four capsules were mixed) was loaded into a cylindrical 3 mm diameter vanadium can and was measured at 1.5, 100, and 297 K. Rietveld refinements of the crystal structures were performed using the FullProf program[30] against the data measured in detector banks at average 2θ values of 58°, 90°, 122°, and 154°, each covering 32° of the scattering plane.

Magnetic measurements were performed on a superconducting quantum interference device (SQUID) magnetometer (Quantum Design, MPMS-XL-7T) between 2 and 400 K in different applied fields under both zero-field-cooled (ZFC) and field-cooled on cooling (FCC) conditions. Negative magnetization observed on some ZFC curves could be caused by the sample insertion procedure or negative trapped fields inside a magnetometer.[15] The inverse magnetic susceptibilities (χ^{-1}) were fit by the Curie−Weiss equation

$$\chi(T) = \mu_{\text{eff}}^2 N \left(3k_{\text{B}}(T-\theta)\right)^{-1} \quad (1)$$

where μ_{eff} is the effective magnetic moment, N is Avogadro's number, k_{B} is Boltzmann's constant, and θ is the Curie−Weiss temperature. For the fitting, we used the FCC curves measured at 10 kOe and temperature intervals between 300 and 395 K for the x = 0 samples and between 200 and 395 K for the x = 1, 2, and 3 samples. Isothermal magnetization measurements were performed between −70 and +70 kOe at different temperatures. Frequency-dependent alternating-current (ac) susceptibility measurements were performed with a Quantum Design MPMS-1T instrument at zero static direct-current (dc) field and different frequencies (f) and different applied oscillating magnetic fields (H_{ac}). Specific heat, C_{p}, at

different magnetic fields was recorded between 2 and 300 K on cooling (and on heating in some cases) by a pulse relaxation method using a commercial calorimeter (Quantum Design PPMS).

First-principles calculations were performed using the projector augmented-wave (PAW) method[31] as implemented in the VASP code.[32] PAW data sets with radial cutoffs of 1.48, 1.34, 1.22, and 0.80 Å for Y, Ga, Mn, and O, respectively, were employed. The exchange-correlation interactions between electrons were treated using the Perdew−Burke−Ernzerhof generalized gradient approximation (GGA)[33] with Hubbard U correction.[34] The effective U value on the Mn 3*d* orbitals was set to 3.9 eV. The interatomic distances strongly influence magnetic interactions. We adopted the experimental lattice constants, and only internal positions are relaxed in all calculations. The forces acting on all the atoms were converged to less than 0.01 eV/Å. The cutoff energy was set to 550 eV, and 2 × 2 × 2 Monkhorst−Pack k-point samplings for the reciprocal space integration were employed for 40-atom models.

3.3. Results and discussion

3.3.1. Crystal Symmetries, Phase Compositions, and Crystal Structure Refinements.

$Y_2MnGa(Mn_{4-x}Ga_x)O_{12}$ solid solutions with $x = 0$, 1, and 2 were single-phase, while the $x = 3$ sample contained about 4.3 wt. % of $Y_3Ga_5O_{12}$ impurity and traces of α-Ga_2O_3 impurity (about 0.7 wt. %), where the weight fractions were estimated from the refined scale factors by RIETAN-2000 after the Rietveld analysis of synchrotron XRPD data. $Y_2MnGa(Mn_{4-x}Ga_x)O_{12}$ solid solutions were found to crystallize in a tetragonal system with space group $P4_2/nmc$ in the parent structure of A-site columnar-ordered quadruple perovskites, $A_2A'A''B_4O_{12}$.[23] They are isostructural with $SmMnGaTiO_6$, $GdMnGaTiO_6$,[35], and $CaFeTi_2O_6$,[36] and therefore structure parameters of $SmMnGaTiO_6$ and $GdMnGaTiO_6$[35] were used as initial ones for the structure refinements of $Y_2MnGa(Mn_{4-x}Ga_x)O_{12}$. Compositional dependence of the lattice parameters in $Y_2MnGa(Mn_{4-x}Ga_x)O_{12}$ as shown in **Figure 3.1.**: the *a* parameter is almost

constant, while the *c* parameter decreases nearly linearly with increasing *x*.

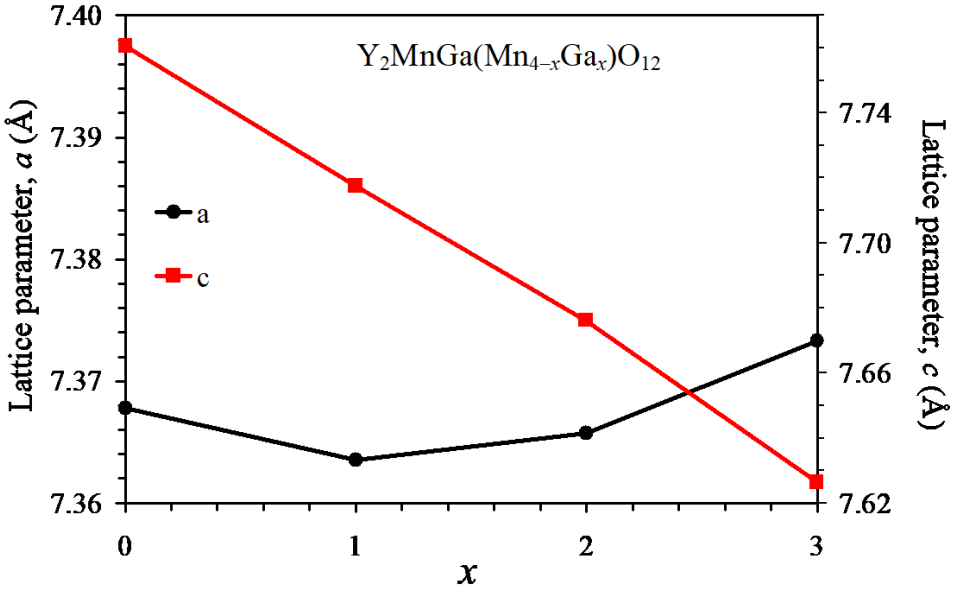

Figure 3.1. Compositional dependence of the lattice parameters (*a* and *c*; space group $P4_2/nmc$) in $Y_2MnGa(Mn_{4-x}Ga_x)O_{12}$ solid solutions.

The ideal cation distribution (that is, with fixed *g*(Mn1) = *g*(Ga2) = *g*(Mn3) = 1) in the *x* = 0 sample, $[Y_2]_A[Mn]_{A'}[Ga]_{A''}[Mn_4]_BO_{12}$, gave the following thermal parameters: *B*(Mn1) = 0.64(9) Å^2, *B*(Ga2) = 2.17(9) Å^2, and *B*(Mn3) = 0.34(3) Å^2. The subsequent refinements of the occupation factors resulted in *g*(Mn1) = 0.984(9), *B*(Mn1) = 0.65(15) Å^2, *g*(Ga2) = 0.938(8), *B*(Ga2) = 1.21(14) Å^2, *g*(Mn3) = 1.026(5), and *B*(Mn3) = 0.60(4) Å^2. The *B* parameter of the Ga2 site (with *g*(Ga2) = 1) was enlarged, and the refined *g* value was noticeably smaller than 1. These facts suggested that the Ga2 site should contain a mixture of Ga and Mn. To keep the total chemical composition, we assumed a distribution of Ga and Mn between the Ga2 and Mn3 sites and only refined *g*(Ga2). Other occupation factors were constrained as follows: *g*(Mn2) = 1 – *g*(Ga2) for the Ga2 site (2*b*) and *g*(Mn3) = 0.75 + 0.25 × *g*(Ga2) and *g*(Ga3) = 0.25 – 0.25 × *g*(Ga2) for the Mn3 = M3 site (8*e*) in order to keep the total chemical compositions at the nominal value. The refined *g*(Ga2) value of 0.68(3) gave the following

cation distribution $[Y_2]_A[Mn]_{A'}[Ga_{0.68}Mn_{0.32}]_{A''}[Mn_{3.68}Ga_{0.32}]_BO_{12}$. The cation distribution obtained from synchrotron XRPD data was very close to the cation distribution found in $[Ho_2]_A[Mn]_{A'}[Ga_{0.66}Mn_{0.34}]_{A''}[Mn_{3.66}Ga_{0.34}]_BO_{12}$ from neutron powder diffraction data.[37] Therefore, the obtained cation distribution in the $x = 0$ sample is quite reasonable. Refined structural parameters, primary bond lengths, and bond-valence sums (BVS)[38] are summarized in **Tables 3.1. and 3.2.** for the $x = 0$ sample.

Table 3.1. Structure Parameters of $Y_2MnGa(Mn_{4-x}Ga_x)O_{12}$ at 297 K from Synchrotron X-ray Powder Diffraction Data

x	0	2	3
a (Å)	7.36095(1)	7.36034(1)	7.36393(1)
c (Å)	7.75384(2)	7.67142(2)	7.61685(2)
V (Å^3)	420.1311(12)	415.5966(10)	413.0428(11)
z(Y)	0.21951(15)	0.22080(13)	0.22039(15)
B(Y) (Å^2)	0.89(3)	0.50(2)	0.21(2)
B(Mn1–SQ) (Å^2)	0.87(10)	0.51(8)	0.09(9)
g(Ga2–T)	0.683(27)Ga	1Ga	1Ga
B(Ga2–T) (Å^2)	0.99(13)	0.34(5)	0.18(7)
g(M3–O)	0.921Mn	0.5Mn	0.25Mn
B(M3–O) (Å^2)	0.61(4)	0.36(2)	0.33(3)
y(O1)	0.0729(6)	0.0639(5)	0.0690(6)
z(O1)	–0.0375(6)	–0.0347(6)	–0.0386(6)
B(O1) (Å^2)	0.16(11)	0.23(9)	0.09(9)
y(O2)	0.5427(8)	0.5497(5)	0.5516(6)
z(O2)	0.5941(9)	0.5978(7)	0.6005(8)
B(O2) (Å^2)	2.86(16)	0.35(10)	0.44(13)
x(O3)	0.4300(4)	0.4301(3)	0.4286(4)
B(O3) (Å^2)	1.04(13)	0.58(8)	0.58(10)
R_{wp} (%)	2.09	1.92	2.19
R_p (%)	1.42	1.36	1.51
R_I (%)	14.58	4.04	4.04
R_F (%)	10.09	4.00	3.43
χ^2	2.29	2.01	2.37

Crystal data: space group $P4_2/nmc$ (No. 137, cell choice 2), $Z = 2$. Y cations occupy the 4*d* site (0.25, 0.25, *z*); Mn1-SQ – 2*a* site (0.75, 0.25, 0.75); Ga2-T – 2*b* site (0.75, 0.25, 0.25); M3-O – 8*e* site (0, 0, 0); O1 and O2 – 8*g* site (0.25, *y*, *z*), and O3 – 8*f* site (*x*, –*x*, 0.25). *g* is the occupation factor. *g*(Y) = 1, *g*(Mn1-SQ) = 1, *g*(O1) = 1, *g*(O2) = 1, and *g*(O3) = 1. SQ: square-planar (site), T: tetrahedral (site), O: octahedral (site).

Table 3.2. Bond Lengths, Bond Angles, Bond-Valence Sum (BVS), and Distortion Octahedral Parameters (Δ) in $Y_2MnGa(Mn_{4-x}Ga_x)O_{12}$ at 297 K from Synchrotron X-ray Powder Diffraction Data

x	0	2	3
Y–O1 (Å) ×2	2.291(5)	2.323(4)	2.268(5)
Y–O1 (Å) ×2	2.364(6)	2.392(4)	2.381(5)
Y–O2 (Å) ×2	2.490(3)	2.400(4)	2.402(5)
Y–O3 (Å) ×4	2.7130(12)	2.7113(8)	2.7170(10)
BVS(Y^{3+})	+3.07	+2.90	+3.05
Mn1–O3 (Å) ×4	1.873(5)	1.875(3)	1.860(4)
Mn1–O2 (Å) ×4	3.074(6)	3.048(5)	3.043(6)
BVS($Mn1^{3+}$)	+3.06	+3.06	+3.18
Ga2–O2 (Å) ×4	1.947(6)	1.881(5)	1.852(5)
Ga2–O1 (Å) ×4	2.892(5)	2.840(4)	2.848(4)
BVS($Ga2^{3+}$)	+2.40	+2.86	+3.07
M3–O1 (Å) ×2	1.9388(14)	1.9178(10)	1.9324(13)
M3–O2 (Å) ×2	2.004(3)	2.021(2)	2.030(3)
M3–O3 (Å) ×2	2.0711(16)	2.0512(11)	2.0442(14)
Δ(M3)	7.3×10^{-4}	8.2×10^{-4}	6.2×10^{-4}
BVS(Mn^{3+})	+3.13	+3.21	+3.15
BVS(Ga^{3+})	+2.89	+2.96	+2.90
M3–O1–M3 ×2	143.31(5)	147.27(5)	144.61(5)
M3–O2–M3 ×2	133.29(5)	131.21(5)	130.19(5)
M3–O3–M3 ×2	138.77(5)	138.46(5)	137.35(5)

The use of the same constraints in the $x = 1$ sample resulted in the refined *g*(Ga2) value of

0.982(19) from synchrotron XRPD data. The cation distribution of the $x = 1$ sample was also determined with neutron powder diffraction data, and the refined g(Ga2) value was 0.924(3) with the same constraints. Therefore, in the final refinements, the ideal cation distribution was assumed from synchrotron XRPD data, and no constraints on the total chemical composition were applied from neutron powder diffraction data. Refined structural parameters, primary bond lengths, and BVS[38] values are summarized in **Table 3.3. and 3.4.** for the $x = 1$ sample. Bond lengths obtained from synchrotron and neutron diffraction data were very close to each other. We note that no combined refinements of both synchrotron and neutron diffraction data were done because samples from different synthesis batches were used. Experimental, calculated, and difference synchrotron XRPD and neutron diffraction patterns of $Y_2MnGa(Mn_3Ga)O_{12}$ are shown in **Figure 3.2**. The crystal structure of $Y_2MnGa(Mn_3Ga)O_{12}$ is illustrated in **Figure 3.3**.

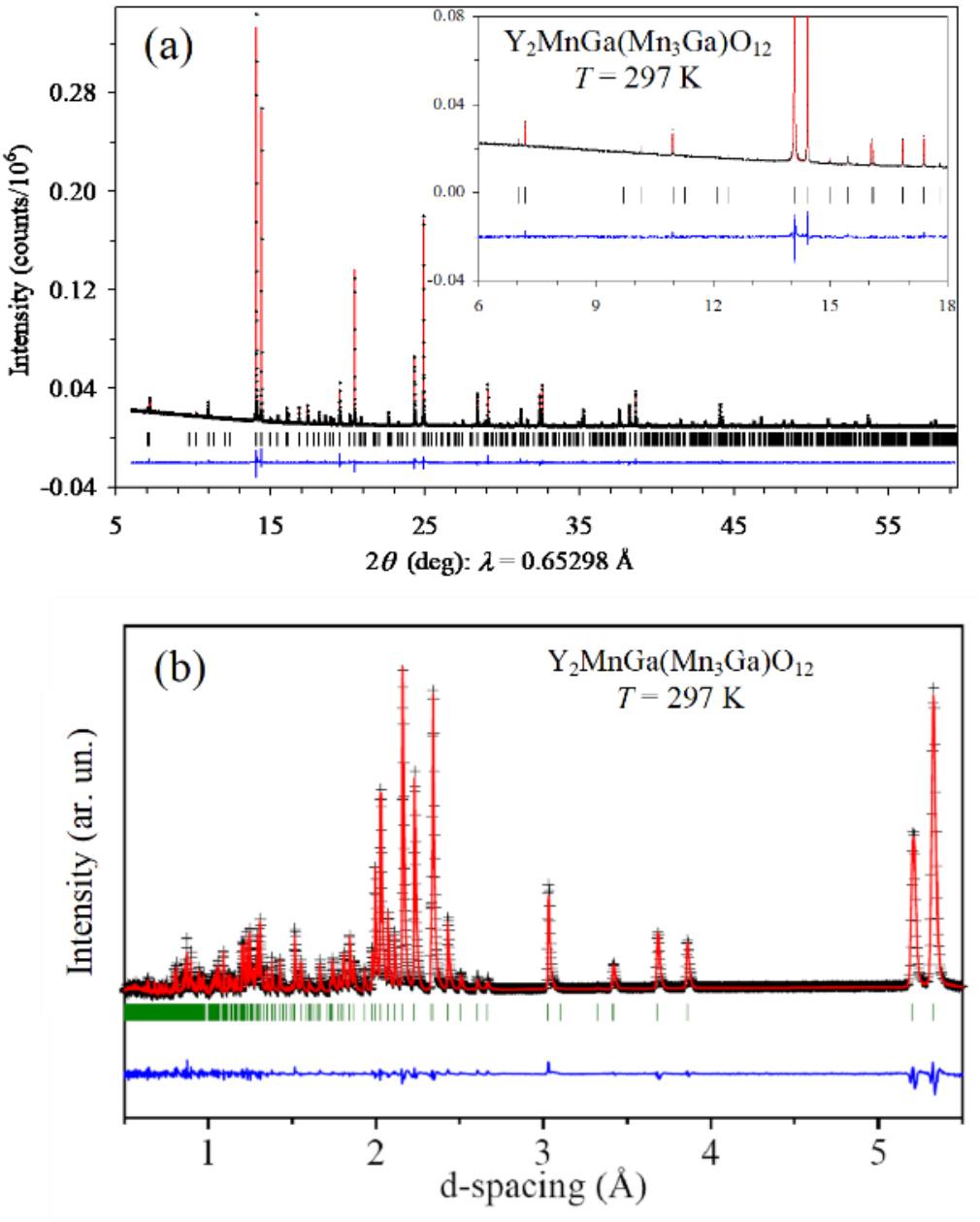

Figure 3.2. Experimental (black crosses), calculated (red line), and difference (blue line) synchrotron X-ray powder diffraction patterns (a) and neutron powder diffraction patterns (b) for $Y_2MnGa(Mn_3Ga)O_{12}$ at T = 297 K. The tick marks show possible Bragg reflection positions of the perovskite phases. The inset shows an enlarged fragment. Ideal cation distributions are given.

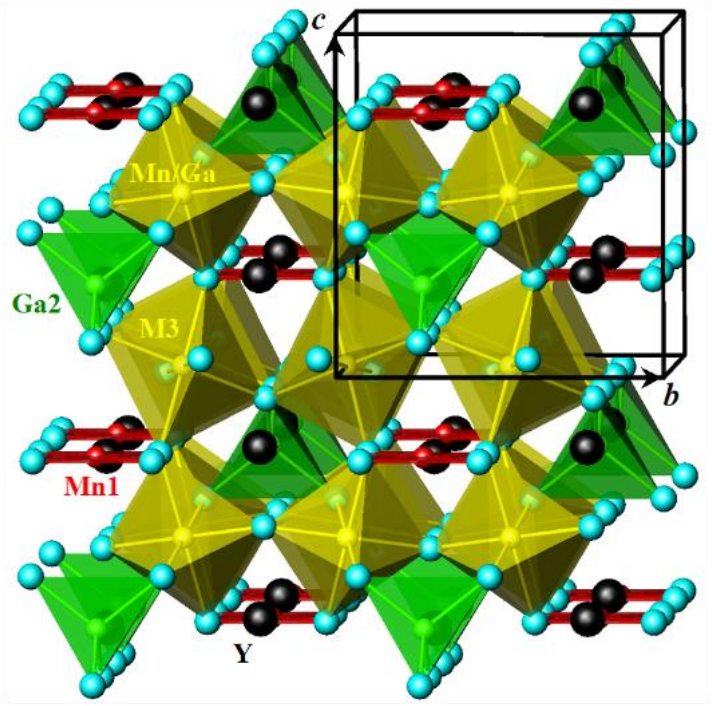

Figure 3.3. Crystal structure of $Y_2MnGa(Mn_3Ga)O_{12}$. $Mn1O_4$ square-planar units, $Ga2O_4$ tetrahedra, and $(Mn/Ga)O_6 = M3O_6$ octahedra are shown. Y atoms are presented by large black spheres.

Table 3.3. Structure Parameters of $Y_2MnGa(Mn_3Ga)O_{12}$ at 297 K from Synchrotron X-ray and Neutron Powder Diffraction Data

	Synchrotron	Neutron
a (Å)	7.36168(1)	7.36215(5)
c (Å)	7.71616(1)	7.71591(9)
V (Å^3)	418.1722(7)	418.211(6)
z(Y)	0.22068(11)	0.22015(18)
B(Y) (Å^2)	0.446(18)	1.87(5)
B(Mn1–SQ) (Å^2)	0.54(7)	1.11(9)
g(Ga2–T)	1Ga	0.934(4)Ga+
B(Ga2–T) (Å^2)	0.54(5)	1.68(10)
g(M3–O)	0.75Mn	0.7160(19)Mn

B(M3–O) (Å^2)	0.40(2)	2.1(6)
y(O1)	0.0741(4)	0.06932(19)
z(O1)	–0.0333(5)	-0.03571(14)
B(O1) (Å^2)	0.33(8)	1.28(4)
y(O2)	0.5491(5)	0.54898(17)
z(O2)	0.5966(6)	0.59780(17)
B(O2) (Å^2)	1.12(10)	1.45(4)
x(O3)	0.4318(3)	0.43204(12)
B(O3) (Å^2)	1.15(9)	1.78(4)
R_{wp} (%)	2.00	3.88
R_p (%)	1.35	3.54
R_I (%)	7.83	3.66
R_F (%)	6.09	-
χ^2	2.18	-

Crystal data: space group $P4_2/nmc$ (No. 137, cell choice 2), Z = 2. Y cations occupy the 4*d* site (0.25, 0.25, *z*); Mn1-SQ – 2*a* site (0.75, 0.25, 0.75); Ga2-T – 2*b* site (0.75, 0.25, 0.25); M3-O – 8*e* site (0, 0, 0); O1 and O2 – 8*g* site (0.25, *y*, *z*), and O3 – 8*f* site (*x*, –*x*, 0.25). *g* is the occupation factor. g(Y) = 1, g(Mn1-SQ) = 1, g(O1) = 1, g(O2) = 1, and g(O3) = 1.

Table 3.4. Bond Lengths, Bond Angles, Bond-Valence Sum (BVS), and Distortion Octahedral Parameters (Δ) in $Y_2MnGa(Mn_3Ga)O_{12}$ at 297 K from Synchrotron X-ray and Neutron Powder Diffraction Data

	Synchrotron	Neutron
Y–O1 (Å) ×2	2.298(4)	2.306(2)
Y–O1 (Å) ×2	2.348(4)	2.380(2)
Y–O2 (Å) ×2	2.401(4)	2.395(2)
Y–O3 (Å) ×4	2.7074(8)	2.707(1)
BVS(Y^{3+})	+3.05	+2.98
Mn1–O3 (Å) ×4	1.893(3)	1.895(1)
Mn1–O2 (Å) ×4	3.056(4)	3.065(1)
BVS($Mn1^{3+}$)	+2.92	+2.89
Ga2–O2 (Å) ×4	1.894(4)	1.889(1)
Ga2–O1 (Å) ×4	2.914(4)	2.874(1)

BVS($Ga2^{3+}$)	+2.73	+2.78
M3–O1 (Å) ×2	1.9366(10)	1.930(1)
M3–O2 (Å) ×2	2.018((2)	2.022(1)
M3–O3 (Å) ×2	2.0556(10)	2.055(1)
Δ(M3)	6.2×10^{-4}	7.0×10^{-4}
BVS(Mn^{3+})	+3.14	+3.15
BVS(Ga^{3+})	+2.89	+2.91
M3–O1–M3 ×2	143.73(5)	145.02(2)
M3–O2–M3 ×2	131.53(5)	131.13(2)
M3–O3–M3 ×2	139.58(5)	139.71(2)

The ideal cation distributions were assumed for the x = 2 and 3 samples, $Y_2MnGa(Mn_{4-x}Ga_x)O_{12}$ and this assumption was confirmed by reasonable B parameters of all the sites. Refined structural parameters, primary bond lengths, and BVS[38] values are summarized in Tables 1 and 2 for the x = 2 and 3 samples.

3.3.2. Crystal Structure Descriptions.

The BVS values for the Y site (+2.90 to +3.07) were close to the expected value of +3 in all samples. The Mn1–O3 bond lengths for the square-planar-coordinated Mn1 site were within 1.86–1.90 Å in all samples as expected for Mn^{3+}, and the BVS values of the Mn1 site (+2.86 to +3.18) support the +3 oxidation state of Mn. The Ga2–O2 bond lengths for the tetrahedral Ga2 site were within 1.85–1.89 Å in the x = 1, 2, and 3 samples as expected for Ga^{3+}, and the BVS values of the Ga2 site (+2.73 to +3.07) were close to +3. On the other hand, the Ga2–O2 bond length was about 1.95 Å in the x = 0 sample, and the BVS value of the Ga2 site was noticeably reduced (+2.40). This feature could be explained by the presence of Mn in the Ga2 site of the x = 0 sample. Because Mn^{3+} cannot be located in tetrahedral sites,[39] the oxidization state of Mn in the Ga2 site should be +2. But the presence of larger Mn^{2+} (with ionic radius of

$r_{IV}(Mn^{2+})$ = 0.66 Å versus $r_{IV}(Ga^{3+})$ = 0.47 Å)[40] noticeably increases the average Ga2–O2 bond length as experimentally observed.

The cation and charge distribution of the x = 0 sample can be presented as $[Y^{3+}{}_2]_A[Mn^{3+}]_{A'}[Ga^{3+}{}_{0.68}Mn^{2+}{}_{0.32}]_{A''}[Mn^{3.087+}{}_{3.68}Ga^{3+}{}_{0.32}]_BO_{12}$, suggesting that a small fraction (about 8.7 %) of Mn at the B site should be in the oxidation state of +4. The cation and charge distribution of the x = 1, 2, and 3 sample can be presented as $[Y^{3+}{}_2]_A[Mn^{3+}]_{A'}[Ga^{3+}]_{A''}[Mn^{3+}{}_{4-x}Ga^{3+}{}_x]_BO_{12}$, where all cations have the +3 oxidation state.

YMn_3O_6 crystallizes in space group *Pmmn* and has two crystallographic positions corresponding to the octahedral B sites with layered charge ordering of Mn^{3+} and $Mn^{3.5+}$.[24] One B site occupied solely by Mn^{3+} has a very strong Jahn-Teller distortion (with the octahedral distortion parameter, Δ, of about 4×10^{-3}). Doping of Ga^{3+} into YMn_3O_6 suppresses the charge-ordered structure, and $Y_2MnGa(Mn_{4-x}Ga_x)O_{12}$ solid solutions crystallize in space group $P4_2/nmc$ with one crystallographic position (M3) corresponding to the octahedral B sites. Surprisingly, the distortion parameters, Δ(M3) = $6–8\times10^{-4}$, and the corresponding M3–O bond lengths are almost the same throughout the solid solutions and do not depend on the amount of Jahn-Teller active Mn^{3+} cations at the B site. In the case of $Sm_2MnMn(Mn_{4-x}Ti_x)O_{12}$ solid solutions, Δ(M3) was 15.8×10^{-4} when the M3 site has 75 % of Jahn–Teller active Mn^{3+} cations (x = 1), and Δ(M3) was 2.2×10^{-4} when the M3 site has 50 % of Jahn-Teller active Mn^{3+} cations (x = 2).[41] Therefore, it seems that the distortions of $M3O_6$ octahedra in $Y_2MnGa(Mn_{4-x}Ga_x)O_{12}$ do not depend on the content of the M3 site, and they are mainly determined by the general structural distortions caused by the content of the A sites, that is, the presence of small Mn^{3+} in the square-planar Mn1 site and small Ga^{3+} in the tetrahedral Ga2 site.

3.3.3. Magnetic Properties of $Y_2MnGa(Mn_{4-x}Ga_x)O_{12}$

Magnetic susceptibilities (χ versus T) of $Y_2MnGa(Mn_{4-x}Ga_x)O_{12}$ are shown in **Figures 3.4. and 3.5**. They were typical for materials with spin-glass-like magnetic properties. They showed

maxima on the ZFC curves and deviations between the ZFC and FCC curves approximately below these maxima. Magnetic susceptibilities were field-independent above certain temperatures and demonstrated field-dependence (that is, differences when measured at 100 Oe and 10 kOe) below about 78 K for $x = 0$, 60 K for $x = 1$, 35 K for $x = 2$, and 18 K for $x = 3$. The temperature point where the difference between the 100 Oe and 10 kOe curves take place systematically shifts to lower temperatures with increasing the content of non-magnetic Ga^{3+}, indicating that this is an intrinsic behavior of the system.

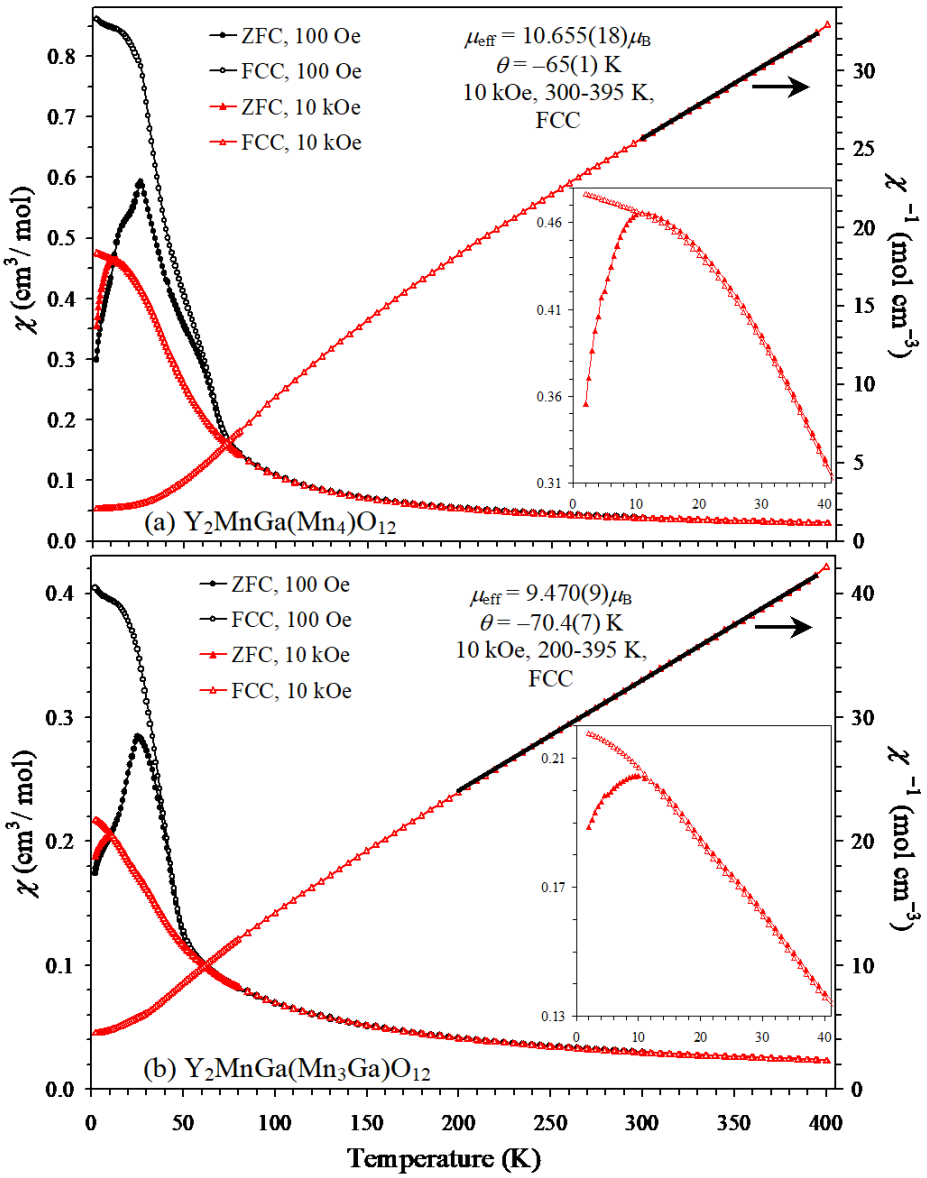

Figure 3.4. ZFC (filled symbols) and FCC (empty symbols) dc magnetic susceptibility ($\chi = M/H$) curves of (a) $Y_2MnGa(Mn_4)O_{12}$ and (b) $Y_2MnGa(Mn_3Ga)O_{12}$ measured at 100 Oe and 10 kOe (left-hand axes). Right-hand axes give the FCC χ^{-1} versus T curves at 10 kOe with the Curie–Weiss fits. Insets show details of the ZFC and FCC curves at 10 kOe at low temperatures.

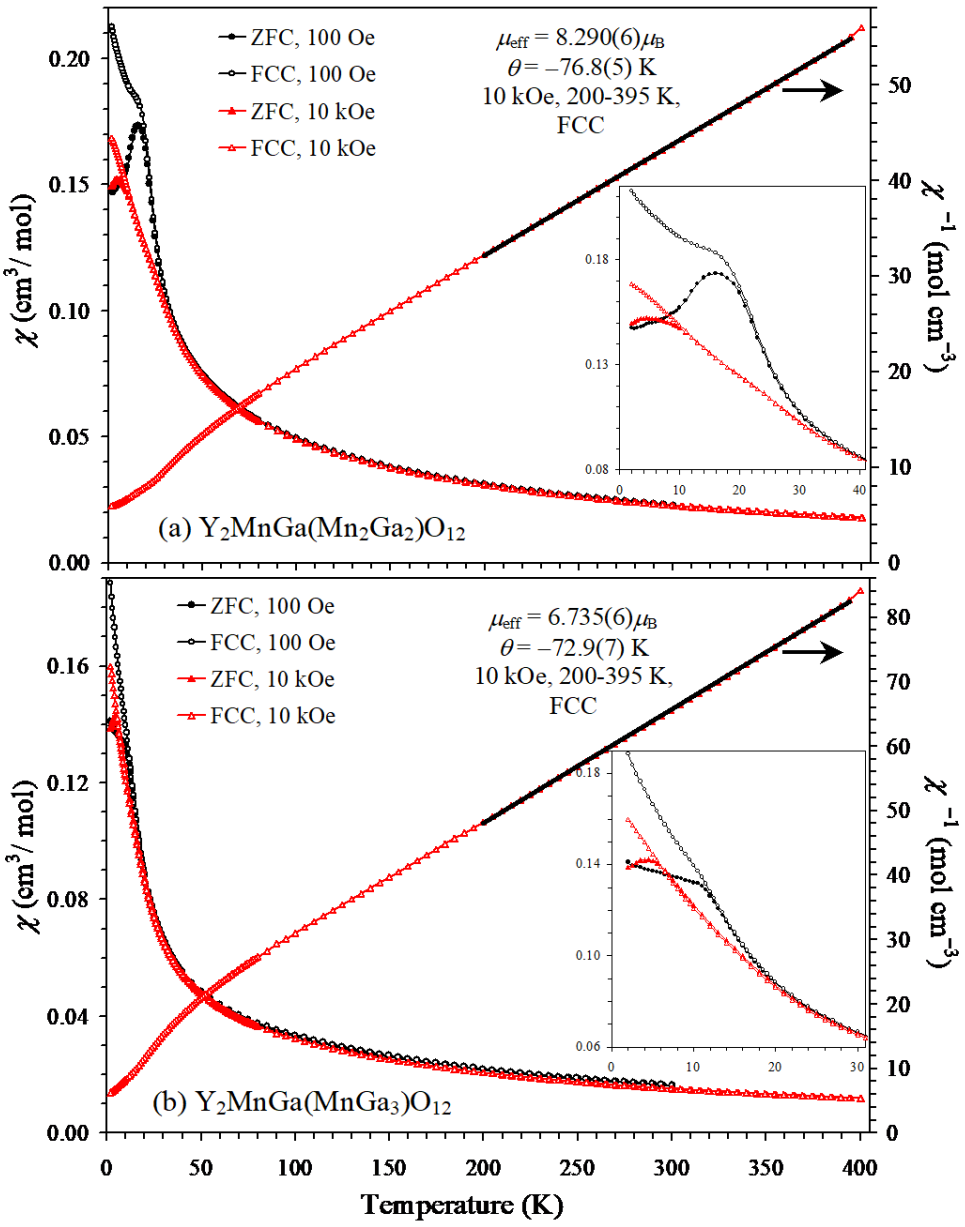

Figure 3.5. ZFC (filled symbols) and FCC (empty symbols) dc magnetic susceptibility ($\chi = M/H$) curves of (a) $Y_2MnGa(Mn_2Ga_2)O_{12}$ and (b) $Y_2MnGa(MnGa_3)O_{12}$ measured at 100 Oe and 10 kOe (left-hand axes). Right-hand axes give the FCC χ^{-1} versus T curves at 10 kOe with the Curie-Weiss fits. Insets show details of the ZFC and FCC curves at 100 Oe and 10 kOe at low temperatures.

Spin-glass (SG) magnetic transition temperatures were determined from sharp peaks or kinks on the χ' versus T and χ'' versus T curves as T_{SG} = 26 K for x = 0, T_{SG} = 26 K for x = 1, T_{SG} = 17 K for x = 2, and T_{SG} = 11 K for x = 3. Ac susceptibility curves are given in **Figure 3.6**. Clear frequency dependence was observed below T_{SG} in all the samples on the χ' versus T curves. Peaks on the χ' versus T and χ'' versus T curves were quite sharp in the x = 0 and 1 samples, while they were broadened in the x = 2 and 3 samples. There was no H_{ac}-field dependence on the χ' versus T and χ'' versus T curves suggesting the absence of the formation of domain structures, which takes place during long-range magnetic orderings. Therefore, all ac susceptibility measurements confirm SG-like transitions.

The inverse dc FCC magnetic susceptibilities (measured at 10 kOe) were fit by the Curie-Weiss equation between 200 and 395 K (x = 1, 2, and 3) or between 300 and 395 K (x = 0) (right-hand axes of Figures 4 and 5)

$$\chi(T) = \mu_{eff}^2 N(3k_B(T-\theta))^{-1} \qquad (1)$$

where μ_{eff} is the effective magnetic moment, N is Avogadro's number, k_B is Boltzmann's constant, and θ is the Curie–Weiss temperature. The obtained values are summarized in **Table 3.5.** The experimental effective magnetic moments were slightly smaller than the calculated values for all the samples. The negative Curie–Weiss temperatures show that the strongest exchange interactions are antiferromagnetic in all compounds.

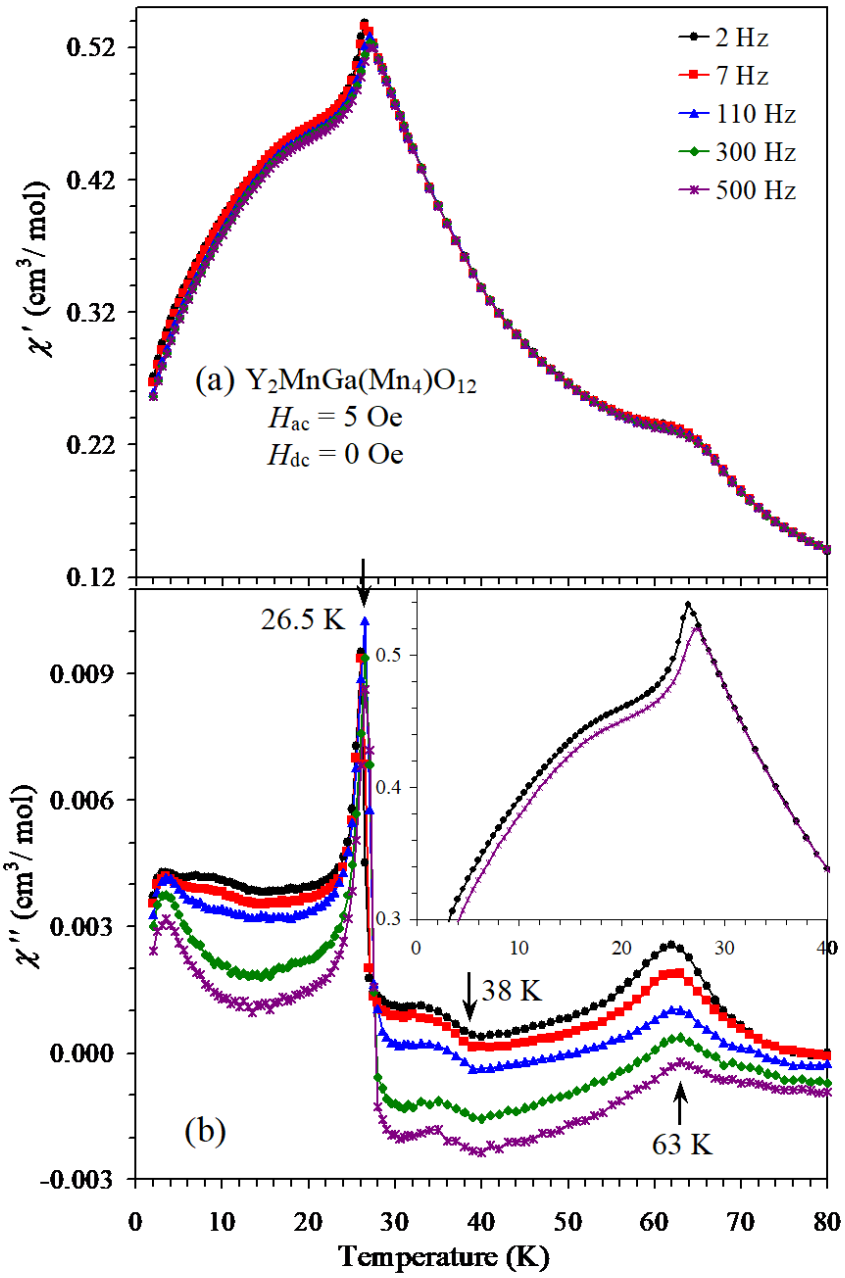

Figure 3.6. (a) Real parts (χ' versus T) and (b) imaginary parts (χ'' versus T) of the ac susceptibilities of $Y_2MnGa(Mn_4)O_{12}$. Measurements were performed on cooling from 80 K to 2 K at zero static (dc) magnetic field using an ac field with the amplitude of H_{ac} = 5 Oe and different frequencies (f = 2, 7, 110, 300, and 500 Hz). Inset shows details of the χ' versus T curves.

Table 3.5. Temperatures of Magnetic Anomalies and Parameters of Curie–Weiss Fits and *M* versus *H* Curves at *T* = 5 K for $Y_2MnGa(Mn_{4-x}Ga_x)O_{12}$ with *x* = 0, 1, 2, and 3

x	T_{SG} (K)	μ_{eff} (μ_B/f.u.)	μ_{calc} (μ_B/f.u.)	θ (K)	M_S (μ_B/f.u.)	M_R (μ_B/f.u.)	H_C (Oe)
0	26	10.655(18)	10.954	–65.0(1.4)	3.09	0.146	~1500
1	26	9.470(9)	9.798	–70.4(7)	2.03	0.049	~1000
2	17	8.290(6)	8.485	–76.8(5)	1.53	0.025	~750
3	11	6.735(6)	6.928	–72.9(7)	1.24	0.012	~450

Curie–Weiss fits were performed between 200 and 395 K for *x* = 1, 2, and 3 and between 300 and 395 K for *x* = 0 using the FCC χ^{-1} versus *T* data at 10 kOe.

M_S is the magnetization value at *T* = 5 K and *H* = 70 kOe. M_R is the remnant magnetization at 5 K, and H_C is the coercive field at 5 K.

T_{SG} is determined from sharp peaks or kinks on the 100 Oe ZFC χ versus *T* curves.

Isothermal magnetization curves (*M* versus *H*) are given in **Figure 3.7**. They were also typical for materials with SG-like magnetic properties as they have stretched S-type shapes with small, extended hysteresis. Parameters of the *M* versus *H* curves are summarized in **Table 3.5.**

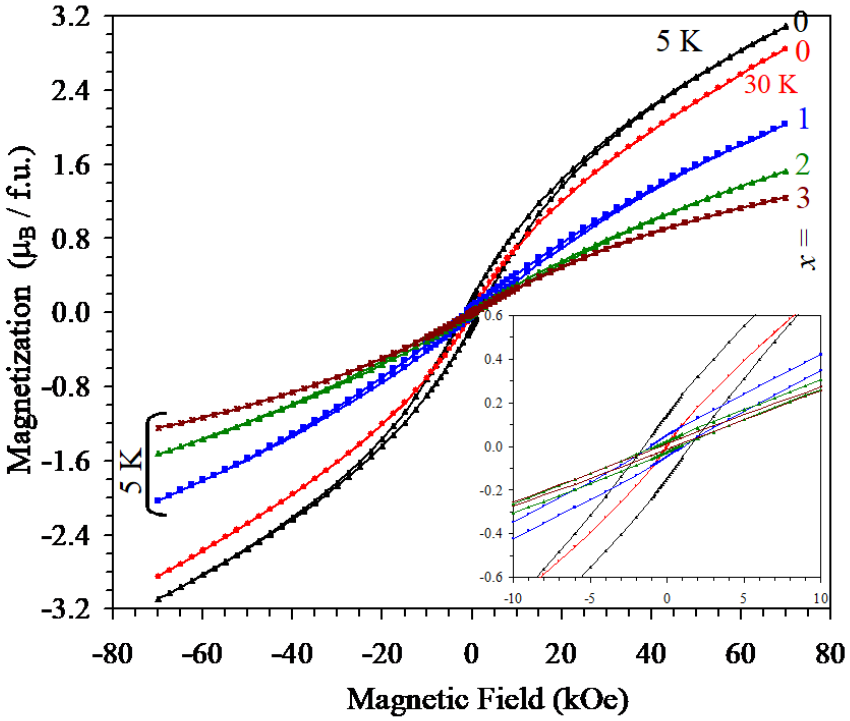

Figure 3.7. *M* versus *H* curves of $Y_2MnGa(Mn_{4-x}Ga_x)O_{12}$ solid solutions at T = 5 K and 30 K for x = 0 and at T = 5 K for x = 1, 2, and 3 (f.u.: formula unit). Inset shows details near the origin.

Specific heat data (**Figures 3.8.–3.10.**) did not show any characteristic λ-type peaks typical for long-range-ordered magnetic transitions even for the x = 0 sample in agreement with the SG-like behavior. Magnetic fields (70–90 kOe) had almost no effects on the specific heat of the x = 0 and 1 samples, while a small effect was observed in the x = 2 and 3 samples below about 10 K.

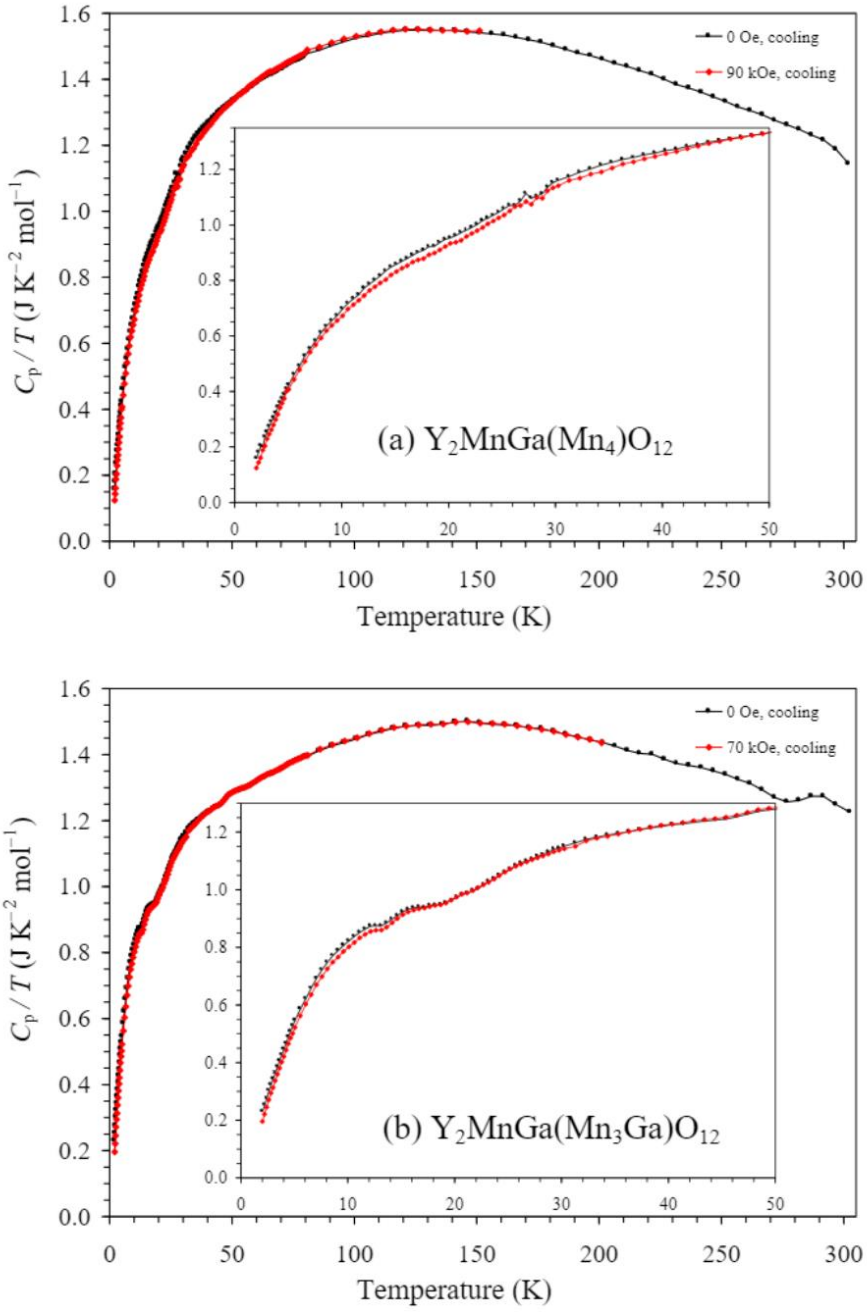

Figure 3.8. Specific heat data of (a) $Y_2MnGa(Mn_4)O_{12}$ measured on cooling at 0 Oe (black curve) and 90 kOe (red curve) and (b) $Y_2MnGa(Mn_3Ga)O_{12}$ measured on cooling 0 Oe (black curve) and 70 kOe (red curve). Data are plotted as C_p/T versus T. Insets show details at low temperatures.

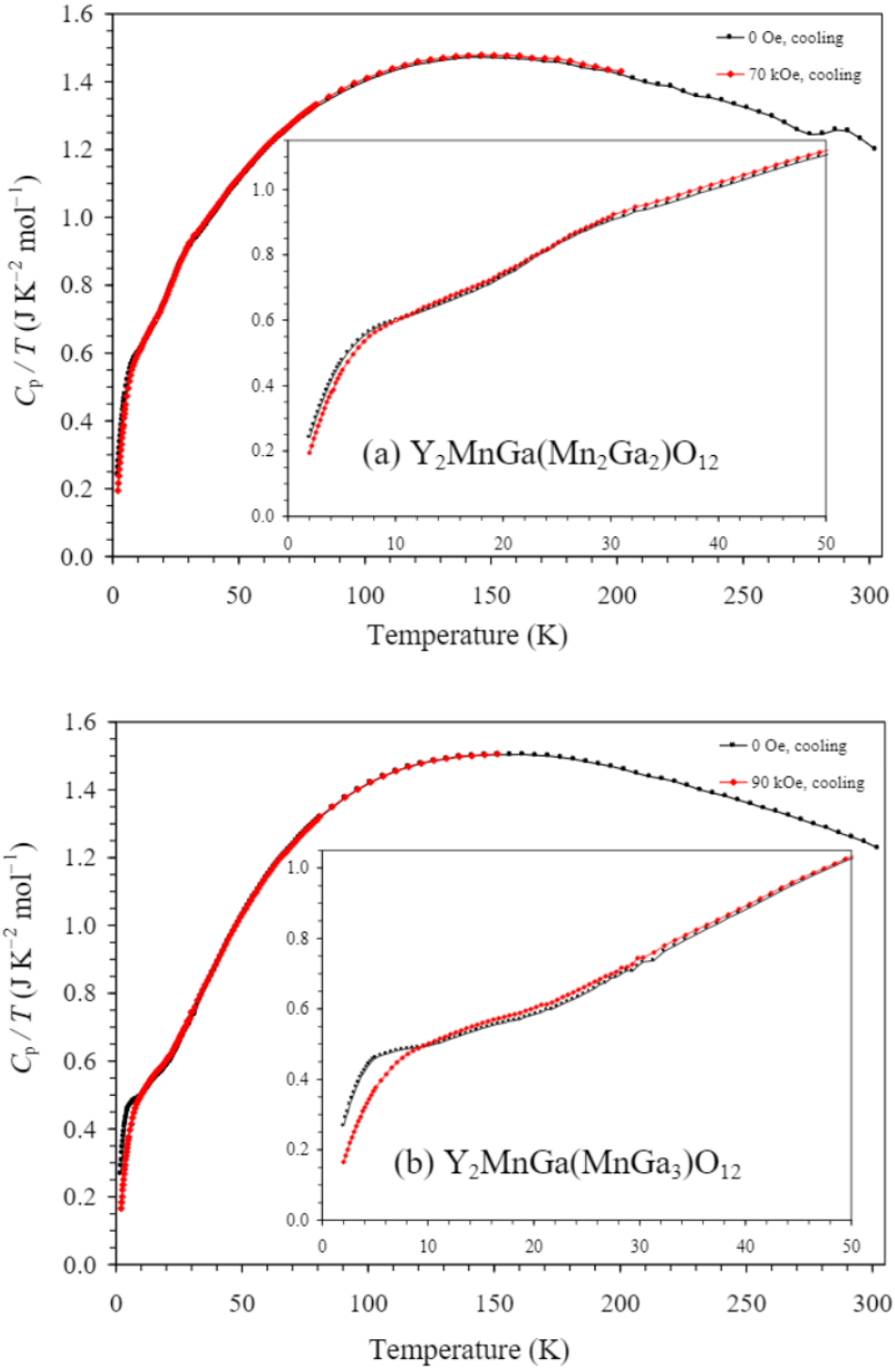

Figure 3.9. Specific heat data of (a) $Y_2MnGa(Mn_2Ga_2)O_{12}$ measured on cooling at 0 Oe (black curve) and 70 kOe (red curve) and (b) $Y_2MnGa(MnGa_3)O_{12}$ measured on cooling 0 Oe (black curve) and 90 kOe (red curve). Data are plotted as C_p/T versus T. Insets show details at low temperatures.

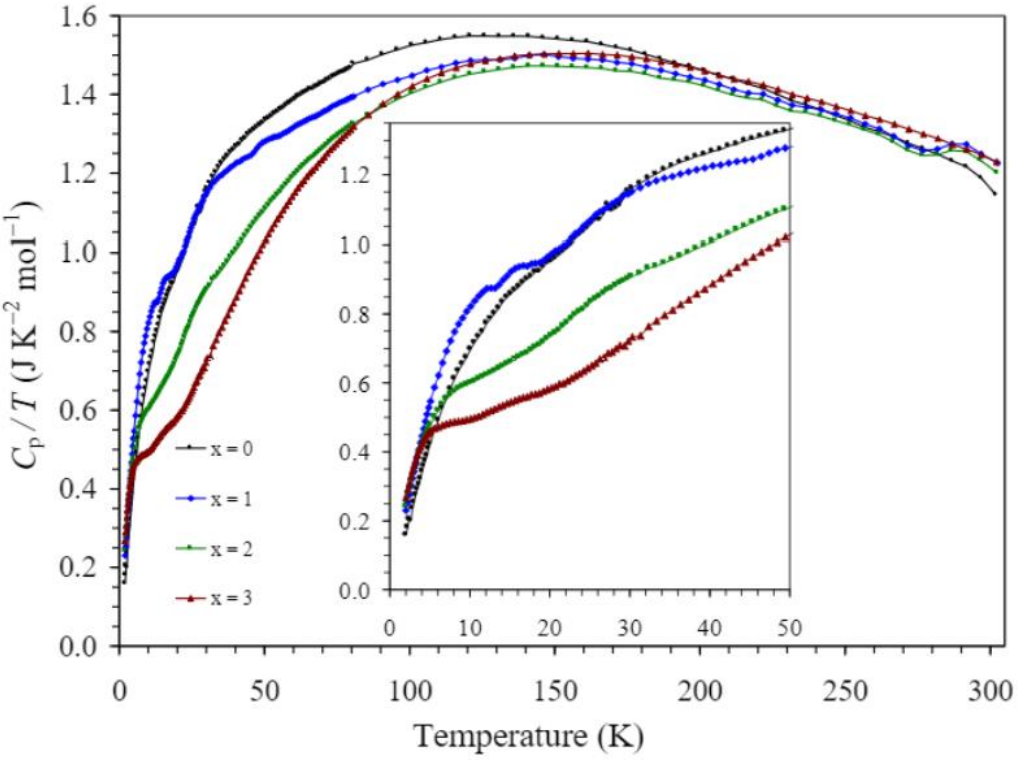

Figure 3.10. Specific heat data $Y_2MnGa(Mn_{4-x}Ga_x)O_{12}$ with x = 0,1,2, and 3 measured on cooling at 0 Oe. Data are plotted as C_p/T versus T. Inset shows details at low temperatures.

No additional sharp magnetic reflections were observed on the neutron powder diffraction pattern of $Y_2MnGa(Mn_3Ga)O_{12}$ at 1.5 K in comparison with the 100 K pattern (**Figure 3.11.**). This fact confirms the absence of long-range magnetic order in agreement with all magnetic and specific heat measurements. However, very broad diffuse scattering centered at about 4.6 Å was found at 1.5 K suggesting short-range antiferromagnetic correlations. As revealed by our first-principles calculations, the sign of the exchange interactions is very sensitive to the presence of Ga in the B site. Therefore, fluctuations and nonuniform distribution of this cation in the lattice are expected to result in the presence of regions with different (ferro or antiferro) spin correlations. However, to demonstrate this diversity of spin correlations, measurements of the magnetic diffuse scattering in a much wider Q-range are required including the small-angle range close to the Q = 0 limit, where clusters with ferromagnetic correlations scatter. No

magnetic reflections were also observed on the neutron powder diffraction pattern of $Ho_2MnGaMn_4O_{12}$ at 1.5 K.[37]

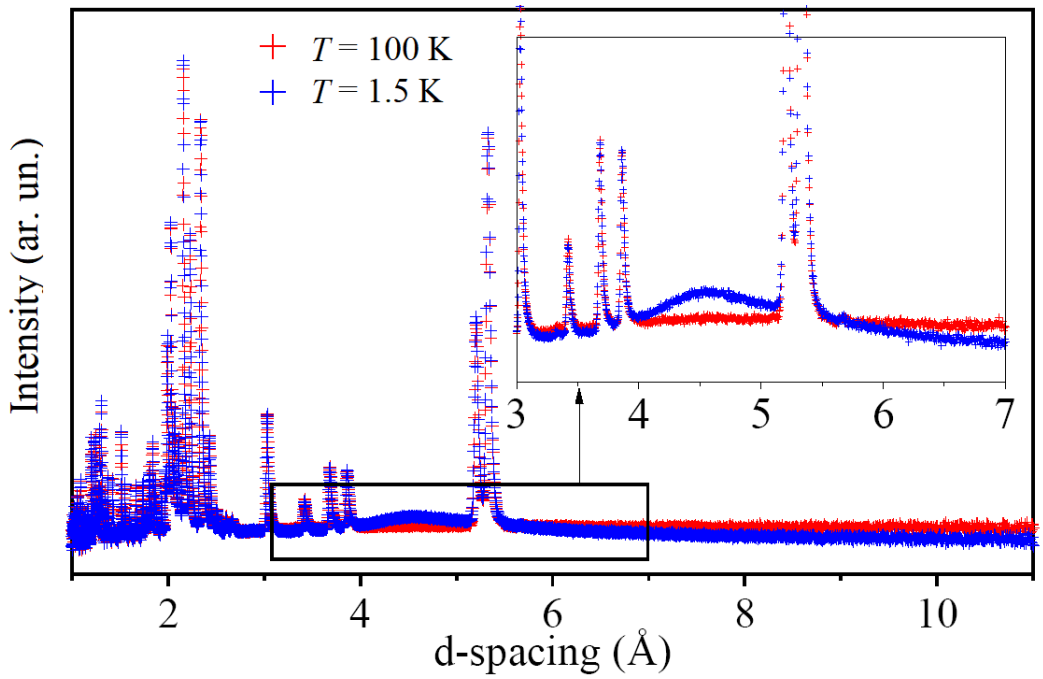

Figure 3.11. Experimental neutron powder diffraction patterns of $Y_2MnGa(Mn_3Ga)O_{12}$ at T = 1.5 K and 100 K. Inset shows details between 3 and 7 Å to emphasize a broad diffuse peak centered near 4.6 Å.

The parent compound YMn_3O_6 (or $Y_2MnMnMn_4O_{12}$) shows a complex magnetic behavior with several long-range-ordered magnetic transitions.[24,25] Therefore, the absence of long-range magnetic ordering in the $Y_2MnGa(Mn_{4-x}Ga_x)O_{12}$ series, especially for the x = 0 composition where the manganese B sublattice is diluted just by 8 % with non-magnetic Ga^{3+} cations, is quite surprising at the first glance. However, the recently established peculiarities of exchange interactions in $TmMn_3O_6$, which are common for all RMn_3O_6 manganites,[25] and the strong preference of Ga to occupy the tetrahedral A″ site found in the present work provides some ideas to qualitatively understand this feature. The key factors could be the dominant

character of the A–B exchange and constraints coming from the A′ and A″ site symmetries. In the tetragonal $P4_2/nmc$ structure of $Y_2MnGa(Mn_{4-x}Ga_x)O_{12}$, both the A′ and A″ sublattices adopt –4*m*2 site symmetry which requires all eight nearest neighbor A–B exchange interactions to be equivalent. This implies that only ferromagnetic B-site intra-sublattice spin polarization can benefit from the A–B exchange (this conclusion can be rigorously obtained based on representation theory). The substitution of Ga for Mn in the tetrahedral A″ site drastically reduces the A–B exchange making it closer to the B–B exchange in the energy scale. This gives rise to a competition between the two exchange interactions, which in turn, makes the system to be very susceptible to the static disorder associated with some degree of randomness in the Ga distribution. In the compositions with $x \geqslant 1$, the A″ sublattice (practically entirely occupied by Ga) is efficiently "excluded" from the exchange and the B-site sublattice is substantially diluted. The latter does not allow drastically changing the balance between the A–B and B–B interactions and promotes a high degree of chemical disorder sufficient to destroy long-range magnetic correlations.

3.3.4. Effects of Doping of YMn_3O_6 by other Trivalent.

In this part, we will describe our results of doping of YMn_3O_6 by other trivalent cations, such as Al^{3+}, Cr^{3+}, and Fe^{3+}. Al^{3+} and Fe^{3+} cations, like Ga^{3+}, can be located in both tetrahedral and octahedral sites. Cr^{3+} shows a very strong preference for octahedral coordination.[39] As the cation distribution is not known and Cr^{3+} should occupy the octahedral site, we will use here a general formula as $Y_2Mn_{6-y}M_{yO12}$ instead of $Y_2MnM(Mn_{4-x}M_x)O_{12}$. $Y_2Mn_{6-y}M_{yO12}$ solid solutions with y = 1, 2, 3, and 4 were prepared at 6 GPa and ∼1570 K for 2 h in Au capsules from stoichiometric mixtures of Y_2O_3, Mn_2O_3, and M_2O_3 (M = Al, Cr, and Fe). Three perovskite phases were found in the case of M = Al and y = 1 and 2: a YMn_3O_6-type *Pmmn* phase, a Y(Mn, Al)O_3-type *Pnma* phase, and a $YMn_3Al_4O_{12}$-type *Im*–3 phase. The appearance

of the YMn_3O_6-type *Pmmn* phase instead of the parent $P4_2/nmc$ structure and almost the same lattice parameters in the y = 1 and 2 samples suggest that the doping level is very small in $Y_2Mn_{6-y}Al_yO_{12}$, and the excess of Al^{3+} goes into other perovskite phases. The y = 3 and 4 samples for M = Al contained just two perovskite phases: a Y(Mn, Al)O_3-type *Pnma* phase and a $YMn_3Al_4O_{12}$-type *Im*–3 phase. $A_2A'A''B_4O_{12}$-related phases appeared only for y = 1 in the case of M = Cr suggesting that the doping level is also small in $Y_2Mn_{6-y}Cr_yO_{12}$, but the doping level of Cr^{3+} is larger than that of Al^{3+}. $A_2A'A''B_4O_{12}$-related phases appeared for all y = 1−4 in case of M = Fe, but their weight fractions were 83−93%, and the samples contained impurities, Y(Mn, Fe)O_3-type *Pnma* phases and Fe_2O_3. These facts suggest that the doping level could be large in $Y_2Mn_{6-y}Fe_yO_{12}$, similar to the doping level by Ga^{3+}, but the synthesis conditions should be optimized to get samples of better quality.

A possible, partial ternary Y_2O_3−Ga_2O_3−Mn_2O_3 phase diagram is shown in **Figure 3.13.** To clarify this phase diagram we also prepared $Mn_{1.4}Ga_{0.6}O_3$ (a single-phase bixbyite-type phase with a = 9.372 Å), $MnGaO_3$ (a two-phase mixture of a bixbyite-type phase with a = 9.357 Å and α-Ga_2O_3), and $YMn_3(Mn_3Ga)O_{12}$ and $YMn_3(Mn_2Ga_2)O_{12}$ (two-phase mixtures of a bixbyite-type phase and a $Y_2MnGa(Mn_{4-x}Ga_x)O_{12}$ - type phase) at the same synthesis conditions. For the Y_2O_3−Ga_2O_3−Mn_2O_3 phase diagram, we also used information about the existence and stability of $Y_3Ga_5O_{12}$[42] and perovskite-related phases of $YGaO_3$,[42] $(R_{1-\delta}Mn_\delta)MnO_3$,[43] YMn_3O_6,[24] and YMn_7O_{12}.[17], interestingly, the doping level by Ga^{3+} is very large in the A-site columnar-ordered quadruple perovskites $Y_2MnGa(Mn_{4-x}Ga_x)O_{12}$, but the doping level by Ga^{3+} is very small in the A-site-ordered quadruple perovskites $YMn_3(Mn_{4-x}Ga_x)O_{12}$. The opposite situation is observed for doping by Al^{3+}.

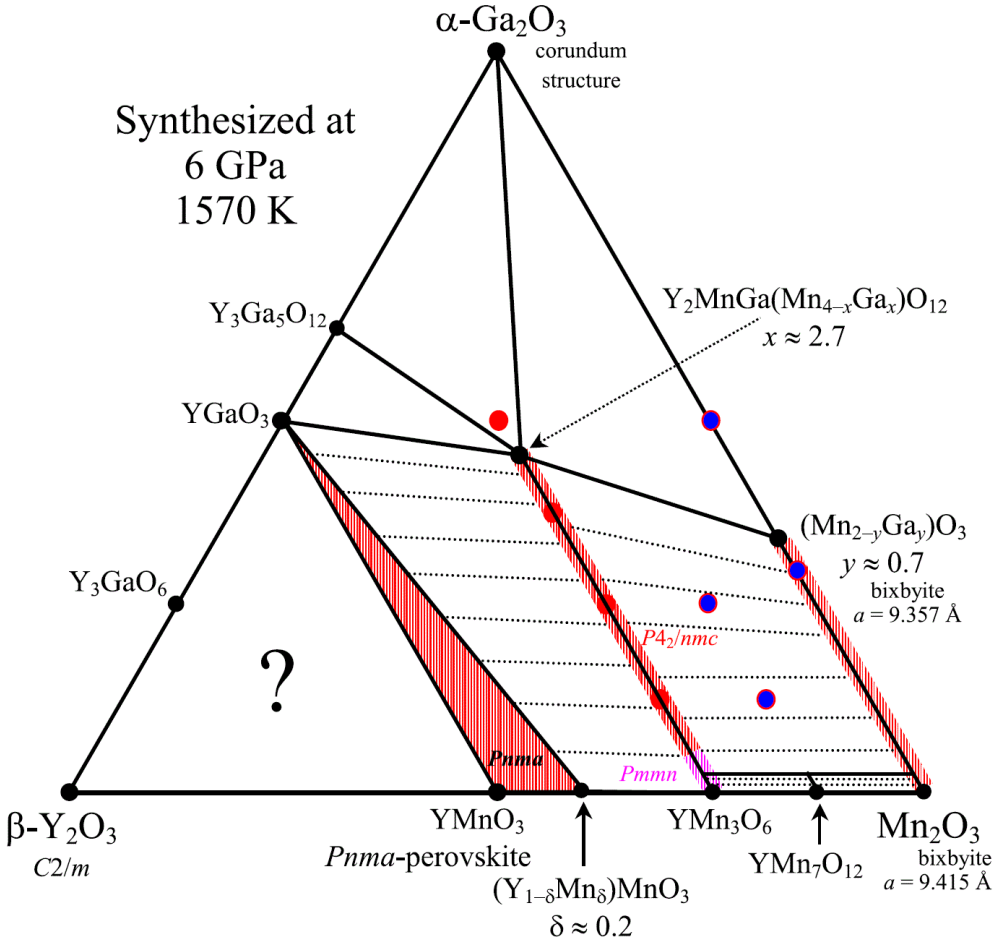

Figure 3.13. A possible partial ternary Y_2O_3–Ga_2O_3–Mn_2O_3 phase diagram after the synthesis at 6 GPa and 1570 K for 2 h in Au capsules. Big red and blue circles show the synthesized compositions. Red-shaded regions show solid solutions. Phase compositions and triangulation near the Y_2O_3 corner were not clarified

3.4. Summary of Chapter 3

A-site columnar-ordered quadruple perovskites $Y_2MnGa(Mn_{4-x}Ga_x)O_{12}$ with x = 0, 1, 2, and 3 were prepared by a high-pressure high-temperature method. Structural studies with synchrotron X-ray and neutron powder diffraction showed that the x = 1, 2, and 3 samples have a complete triple order of cations at the A sites, while the x = 0 sample has partial disordering of Ga and Mn at the A″ and B sites with the preferred occupation of the A″ site by Ga. No

long-range magnetic ordering was observed in all compositions, and they just exhibit SG-like magnetic properties. The first-principles calculations indicated that the AFM interactions could be attributed to the Ga substitution to the B sites and showed that robust ferromagnetism could be realized in this family of perovskite materials in case of ideal cation distributions.

References in chapter 3

1. Salamon, M. B.; Jaime, M., The physics of manganites: Structure and transport. *Rev. Mod. Phys.* **2001,** *73* (3), 583.
2. Edwards, D., Ferromagnetism and electron-phonon coupling in the manganites. *Advances in Physics* **2002,** *51* (5), 1259-1318.
3. Fergus, J. W., Oxide materials for high temperature thermoelectric energy conversion. *J. Eur. Ceram. Soc.* **2012,** *32* (3), 525-540.
4. Zhang, K.; Han, X.; Hu, Z.; Zhang, X.; Tao, Z.; Chen, J., Nanostructured Mn-based oxides for electrochemical energy storage and conversion. *Chem. Soc. Rev.* **2015,** *44* (3), 699-728.
5. Du, J.; Zhang, T.; Cheng, F.; Chu, W.; Wu, Z.; Chen, J., Nonstoichiometric perovskite $CaMnO_{3-\delta}$ for oxygen electrocatalysis with high activity. *Inorg. Chem.* **2014,** *53* (17), 9106-9114.
6. Bhattacharjee, S.; Bousquet, E.; Ghosez, P., Engineering multiferroism in $CaMnO_3$. *Phys. Rev. Lett.* **2009,** *102* (11), 117602.
7. Coey, J.; Viret, M.; Von Molnar, S., Mixed-valence manganites. *Advances in physics* **1999,** *48* (2), 167-293.
8. Kimura, T.; Goto, T.; Shintani, H.; Ishizaka, K.; Arima, T.-h.; Tokura, Y., Magnetic control of ferroelectric polarization. *Nature* **2003,** *426* (6962), 55-58.
9. Vasil'ev, A.; Volkova, O., New functional materials $AC_3B_4O_{12}$. *Low Temperature Physics* **2007,** *33* (11), 895-914.
10. Prodi, A.; Daoud-Aladine, A.; Gozzo, F.; Schmitt, B.; Lebedev, O.; Van Tendeloo, G.; Gilioli, E.; Bolzoni, F.; Aruga-Katori, H.; Takagi, H., Commensurate structural modulation in the charge-and orbitally ordered phase of the quadruple perovskite $(NaMn_3)Mn_4O_{12}$. *Phys. Rev. B* **2014,** *90* (18), 180101.

11. Glazkova, Y. S.; Terada, N.; Matsushita, Y.; Katsuya, Y.; Tanaka, M.; Sobolev, A. V.; Presniakov, I. A.; Belik, A. A., High-pressure synthesis, crystal structures, and properties of $CdMn_7O_{12}$ and $SrMn_7O_{12}$ perovskites. *Inorg. Chem.* **2015,** *54* (18), 9081-9091.
12. Belik, A. A.; Glazkova, Y. S.; Terada, N.; Matsushita, Y.; Sobolev, A. V.; Presniakov, I. A.; Tsujii, N.; Nimori, S.; Takehana, K.; Imanaka, Y., Spin-driven multiferroic properties of $PbMn_7O_{12}$ perovskite. *Inorg. Chem.* **2016,** *55* (12), 6169-6177.
13. Chen, W.-T.; Wang, C.-W.; Wu, H.-C.; Chou, F.-C.; Yang, H.-D.; Simonov, A.; Senn, M. S., Improper ferroelectric polarization in a perovskite driven by intersite charge transfer and ordering. *Phys. Rev. B* **2018,** *97* (14), 144102.
14. Belik, A. A.; Matsushita, Y.; Kumagai, Y.; Katsuya, Y.; Tanaka, M.; Stefanovich, S. Y.; Lazoryak, B. I.; Oba, F.; Yamaura, K., Complex Structural Behavior of $BiMn_7O_{12}$ Quadruple Perovskite. *Inorg. Chem.* **2017,** *56* (20), 12272-12281.
15. Zhang, L.; Terada, N.; Johnson, R. D.; Khalyavin, D. D.; Manuel, P.; Katsuya, Y.; Tanaka, M.; Matsushita, Y.; Yamaura, K.; Belik, A. A., High-pressure synthesis, structures, and properties of trivalent A-site-ordered quadruple perovskites RMn_7O_{12} (R= Sm, Eu, Gd, and Tb). *Inorg. Chem.* **2018,** *57* (10), 5987-5998.
16. Mezzadri, F.; Calicchio, M.; Gilioli, E.; Cabassi, R.; Bolzoni, F.; Calestani, G.; Bissoli, F., High-pressure synthesis and characterization of $PrMn_7O_{12}$ polymorphs. *Phys. Rev. B* **2009,** *79* (1), 014420.
17. Johnson, R.; Khalyavin, D.; Manuel, P.; Katsuya, Y.; Tanaka, M.; Matsushita, Y.; Zhang, L.; Yamaura, K.; Belik, A., Displacive structural phase transitions and the magnetic ground state of quadruple perovskite YMn_7O_{12}. *Phys. Rev. B* **2019,** *99* (2), 024107.

18. Johnson, R.; Mezzadri, F.; Manuel, P.; Khalyavin, D.; Gilioli, E.; Radaelli, P., Evolution of Magneto-Orbital order Upon B-Site Electron Doping in $Na_{1-x}Ca_xMn_7O_{12}$ Quadruple Perovskite Manganites. *Phys. Rev. Lett.* **2018,** *120* (25), 257202.
19. Johnson, R.; Chapon, L.; Khalyavin, D.; Manuel, P.; Radaelli, P.; Martin, C., Giant improper ferroelectricity in the ferroaxial magnet $CaMn_7O_{12}$. *Phys. Rev. Lett.* **2012,** *108* (6), 067201.
20. Terada, N.; Glazkova, Y. S.; Belik, A. A., Differentiation between ferroelectricity and thermally stimulated current in pyrocurrent measurements of multiferroic MMn_7O_{12}(M= Ca, Sr, Cd, Pb). *Phys. Rev. B* **2016,** *93* (15), 155127.
21. Yamada, I., Novel catalytic properties of quadruple perovskites. *Science and Technology of advanced MaTerialS* **2017,** *18* (1), 541-548.
22. Belik, A. A.; Matsushita, Y.; Khalyavin, D. D., Reentrant structural transitions and collapse of charge and orbital orders in quadruple perovskites. *Angew. Chem. Int. Ed.* **2017,** *56* (35), 10423-10427.
23. Belik, A. A., Rise of A-site columnar-ordered $A_2A'A''B_4O_{12}$ quadruple perovskites with intrinsic triple order. *Dalton Transactions* **2018,** *47* (10), 3209-3217.
24. Zhang, L.; Matsushita, Y.; Yamaura, K.; Belik, A. A., Five-Fold Ordering in High-Pressure Perovskites RMn_3O_6(R= Gd–Tm and Y). *Inorg. Chem.* **2017,** *56* (9), 5210-5218.
25. Vibhakar, A.; Khalyavin, D.; Manuel, P.; Zhang, L.; Yamaura, K.; Radaelli, P.; Belik, A.; Johnson, R., Magnetic structure and spin-flop transition in the A-site columnar-ordered quadruple perovskite TmMn 3 O 6. *Phys. Rev. B* **2019,** *99* (10), 104424.
26. Tanaka, M.; Katsuya, Y.; Yamamoto, A., A new large radius imaging plate camera for high-resolution and high-throughput synchrotron X-ray powder diffraction by multiexposure method. *Rev. Sci. Instrum.* **2008,** *79* (7), 075106.

27. Tanaka, M.; Katsuya, Y.; Matsushita, Y.; Sakata, O., Development of a synchrotron powder diffractometer with a one-dimensional X-ray detector for analysis of advanced materials. *J. Ceram. Soc. Jpn.* **2013,** *121* (1411), 287-290.

28. Izumi, F.; Ikeda, T. In A rietveld-analysis programm RIETAN-98 and its applications to zeolites, *Mater. Sci. Forum*, **2000**, 321-324, 198-205.

29. Chapon, L. C.; Manuel, P.; Radaelli, P. G.; Benson, C.; Perrott, L.; Ansell, S.; Rhodes, N. J.; Raspino, D.; Duxbury, D.; Spill, E., Wish: The new powder and single crystal magnetic diffractometer on the second target station. *Neutron News* **2011,** *22* (2), 22-25.

30. Rodríguez-Carvajal, J., Recent advances in magnetic structure determination by neutron powder diffraction. *Physica B* **1993,** *192* (1-2), 55-69.

31. (a) Blöchl, P. E., Projector Augmented-Wave Method. *Phys. Rev. B: Condens. Matter Mater. Phys.* **1994**, *50*, 17953−17979. (b) Kresse, G.; Joubert, J. From Ultrasoft Pseudopotentials to the Projector Augmented-Wave Method. *Phys. Rev. B: Condens. Matter Mater. Phys.* **1999**, *59*, 1758−1775.

32. Kresse, G.; Hafner, J., Ab initio molecular dynamics for liquid metals. *Phys. Rev. B* **1993,** *47* (1), 558-561.

33. Perdew, J. P.; Ruzsinszky, A.; Csonka, G. I.; Vydrov, O. A.; Scuseria, G. E.; Constantin, L. A.; Zhou, X.; Burke, K., Restoring the density-gradient expansion for exchange in solids and surfaces. *Phys. Rev. Lett.* **2008,** *100* (13), 136406.

34. Dudarev, S.; Botton, G.; Savrasov, S.; Humphreys, C.; Sutton, A., Electron-energy-loss spectra and the structural stability of nickel oxide: An LSDA+ U study. *Phys. Rev. B* **1998,** *57* (3), 1505.

35. Leinenweber, K.; Parise, J., High-pressure synthesis and crystal structure of $CaFeTi_2O_6$, a new perovskite structure type. *J. Solid State Chem.* **1995,** *114* (1), 277-281.

36. Shimura, G.; Niwa, K.; Shirako, Y.; Hasegawa, M., High-Pressure Synthesis and Magnetic Behavior of A-Site Columnar-Ordered Double Perovskites, $LnMn(Ga_{0.5}Ti_{0.5})_2O_6$(Ln= Sm, Gd). *Eur. J. Inorg. Chem.* **2017,** *2017* (4), 835-839.
37. Belik, A. A.; Khalyavin, D. D.; Zhang, L.; Matsushita, Y.; Katsuya, Y.; Tanaka, M.; Johnson, R. D.; Yamaura, K., Intrinsic Triple Order in A-site Columnar-Ordered Quadruple Perovskites: Proof of Concept. *Chemphyschem* **2018,** *19* (19), 2449-2452.
38. Brese, N.; O'keeffe, M., Bond-valence parameters for solids. *Acta Crystallogr. Sect. B: Struct. Sci.* **1991,** *47* (2), 192-197.
39. Waroquiers, D.; Gonze, X.; Rignanese, G.-M.; Welker-Nieuwoudt, C.; Rosowski, F.; Göbel, M.; Schenk, S.; Degelmann, P.; André, R.; Glaum, R., Statistical analysis of coordination environments in oxides. *Chem. Mater.* **2017,** *29* (19), 8346-8360.
40. Shannon, R. D., Revised effective ionic radii and systematic studies of interatomic distances in halides and chalcogenides. *Acta crystallographica section A: crystal physics, diffraction, theoretical and general crystallography* **1976,** *32* (5), 751-767.
41. Belik, A. A.; Zhang, L.; Liu, R.; Khalyavin, D. D.; Katsuya, Y.; Tanaka, M.; Yamaura, K., Valence Variations by B-Site Doping in A-Site Columnar-Ordered Quadruple Perovskites $Sm_2MnMn(Mn_{4-x}Ti_x)O_{12}$ with $1 \leq x \leq 3$. *Inorg. Chem.* **2019,** *58* (5), 3492-3501.
42. Marezio, M.; Remeika, J.; Dernier, P., High pressure synthesis of $YGaO_3$, $GdGaO_3$ and $YbGaO_3$. *Mater. Res. Bull.* **1966,** *1* (4), 247-255.
43. Zhang, L.; Gerlach, D.; Dönni, A.; Chikyow, T.; Katsuya, Y.; Tanaka, M.; Ueda, S.; Yamaura, K.; Belik, A. A., Mn Self-Doping of Orthorhombic $RMnO_3$ Perovskites:$(R_{0.667}Mn_{0.333})MnO_3$ with R= Er–Lu. *Inorg. Chem.* **2018,** *57* (5), 2773-2781.

Chapter 4. Ferrimagnetic and relaxor ferroelectric properties of $R_2MnMn(MnTi_3)O_{12}$ perovskites with R = Nd, Eu, and Gd

4.1 Introduction

Perovskite-structure ABO_3 perovskites show a large variety of phase transitions driven by the BO_6 octahedral rotations, which in turn are driven by the size mismatch of the A and B cations, and by ferroelectric instabilities, driven by the hybridization between low-lying empty d states and oxygen states or by effects of lone-pair electrons.[1–3] Polar and ferroelectric distortions can take place on a long-range scale resulting in well-defined ferroelectric transitions or on a short-range scale producing relaxor-type dielectric and ferroelectric responses. As a result, simple ABO_3 perovskites form a very important class of ferroelectric and piezoelectric materials that are used in many aspects of our lives. In particular, relaxor ferroelectric materials have high dielectric and piezoelectric constants,[4] which might be nearly temperature-independent in wide temperature ranges, high specific capacitance, and low remnant polarization requiring low electric fields for switching.

The number of reported proper polar distortions (that is, not caused by spin-induced symmetry breaking) in the so-called A-site-ordered quadruple perovskites with the generic chemical formula of $AA'_3B_4O_{12}$ is very limited.[5] Polar distortions were only reported in $BiMn_7O_{12}$ [6–8] and its derivatives,[9,10] driven by the activity of lone-pair electrons of Bi^{3+} cations, and in $HgMn_7O_{12}$ below 260 K.[11] Even $PbMn_7O_{12}$, which also has lone-pair-electron active Pb^{2+} cations, crystallizes in a centrosymmetric space group.[12] Nevertheless, the dielectric properties of $AA'_3B_4O_{12}$ -type materials have attracted a lot of attention even if materials have centrosymmetric crystal structures after the discovery of giant dielectric constant in cubic $CaCu_3Ti_4O_{12}$ in a wide temperature range.[13] The origin of exceptional dielectric properties of $CaCu_3Ti_4O_{12}$-related materials is electrical inhomogeneity due to the presence of

semiconducting grains and insulating grain boundaries that create an internal barrier layer capacitor effect.[14–16] To the best of our knowledge, relaxor ferroelectric behavior has not been observed among $AA'_3B_4O_{12}$ -type quadruple perovskites.

A new mechanism for ferroelectricity has been recently proposed in $CaMnTi_2O_6$ perovskite,[17,18] which belongs to the so-called A-site columnar-ordered quadruple perovskite family with a generic chemical formula $A_2A'A''B_4O_{12}$.[19] $CaMnTi_2O_6$ shows a well-defined ferroelectric transition at 630 K and switchable ferroelectric polarization at room temperature.[17] It crystallizes in space group $P4_2mc$ below the ferroelectric transition and space group $P4_2/nmc$ above the ferroelectric transition.[17,18] $CaMnTi_2O_6$ and its derivatives[18,20] are the only examples of polar distortions in this subfamily of perovskite materials. Therefore, the expansion of possible functional properties of such perovskites requires the discovery of more examples with polar distortions. From the viewpoint of magnetism, $CaMnTi_2O_6$ exhibits a simple antiferromagnetic (AFM) transition at the Néel temperature of about 10 K.[17,18] However, A-site columnar-ordered quadruple perovskites can show complex magnetic behaviors if magnetic cations are introduced into the B sites in addition to the A sites.[21,22]

In this work, we describe the observation of relaxor ferroelectric behavior in $R_2MnMn(MnTi_3)O_{12}$ oxides with R = Nd, Eu, and Gd, belonging to the family of A-site columnar-ordered quadruple perovskites. In addition, the presence of magnetic rare-earth cations at the A sites and just 25% of magnetic Mn^{2+} cations at the B sites produce ferrimagnetic structures with large uncompensated moments. The coexistence of ferrimagnetic and relaxor-like ferroelectric properties makes $R_2MnMn(MnTi_3)O_{12}$ quadruple perovskites multiferroic materials.

4.2. Experimental details of Chapter 4

$R_2MnMn(MnTi_3)O_{12}$ samples with R = La, Nd, Eu, Gd, and Dy were prepared from stoichiometric mixtures of MnO and commercial TiO_2 (99.9%) and R_2O_3 (99.9%) at 6 GPa and about 1570 K for 2 h in Au capsules using a belt-type high-pressure apparatus, where the synthesis temperature was reached in 10 min. After heat treatments, the samples were quenched to room temperature (RT), and the pressure was slowly released. All samples were dense pellets. Powder samples (after grinding) had dark-brown color. Single-phase MnO was prepared from commercial MnO_2 (99.99%) by annealing at 1273 K in a 20% H_2 + 80% Ar flow for 4 h. TiO_2 and R_2O_3 were annealed at 1273 K for 1 h before use.

X-ray powder diffraction (XRPD) data were collected at RT on a RIGAKU MiniFlex600 diffractometer using CuKa radiation (2θ range of 8–100°, a step width of 0.02°, and a scan speed of 1 °/min). Synchrotron XRPD data were measured at RT on a large Debye–Scherrer camera at the undulator beamline BL15XU of SPring-8.[23,24] The intensity data were collected between 2° and 60.23° at 0.003° intervals in 2θ; the incident beam was monochromatized at λ = 0.65298 Å. The samples were put into Lindemann glass capillaries (inner diameter: 0.1 mm), which were rotated during measurements. The Rietveld analysis was performed using the RIETAN-2000 program.[25] Mass fractions of phases (mass %) reported in this work were estimated by RIETAN-2000 from the refined scale factors after the Rietveld analysis of synchrotron XRPD data.

Magnetic measurements were performed on a SQUID magnetometer (Quantum Design, MPMS-XL-7T) between 2 and 400 K in different applied fields under both zero-field-cooled (ZFC) and field-cooled on cooling (FCC) conditions. The inverse magnetic susceptibilities (χ^{-1}) were fit by the Curie–Weiss equation

$$\chi(T) = \mu_{\text{eff}}^2 N \left(3k_{\text{B}}(T-\theta)\right)^{-1} \qquad (1)$$

where μ_{eff} is the effective magnetic moment, N is Avogadro's number, k_B is Boltzmann's constant, and θ is the Curie–Weiss temperature. For the fitting, we used the FCC curves measured at 10 kOe and temperature intervals between 250 K and 395 K. Isothermal magnetization measurements were performed between –70 kOe and +70 kOe at different temperatures. Specific heat, C_p, at different magnetic fields was recorded between 2 K and 300 K on cooling and heating by a pulse relaxation method using a commercial calorimeter (Quantum Design PPMS). Dielectric data were measured using a NOVOCONTROL Alpha-A High-Performance Frequency Analyzer between 3 K and 330 K on cooling and heating (with the cooling-heating rate of 0.5–1 K min^{-1}) in the frequency range of 100 Hz and 2 MHz and at magnetic fields of 0 Oe and 90 kOe. Impedance spectroscopy was also performed on the same instrument between 200 K and 350 K (with a step of 5 K) in the frequency range of 0.01 Hz and 10 MHz. An epoxy silver paste (dried at 390–410 K) was used as electrodes.

Ferroelectric properties were evaluated by *P–E* hysteresis loop measurements using an aixACCT TF analyzer 2000 ferroelectric tester at frequencies of 0.02–2 Hz and liquid nitrogen temperature. The samples were, therefore, immersed in liquid nitrogen. No RT measurements were performed as conductivity at RT was too high to apply a high voltage of 8–9 kV. The same pellets with Ag electrodes as those used for dielectric and impedance measurements were used for *P–E* measurements. In the case of $Eu_2MnMn(MnTi_3)O_{12}$, we also tried Au electrodes prepared by Au sputtering and annealing at 573 K for 10 min in air, and the sample thickness was reduced by about 2 times to 0.487 mm (in comparison with the Ag electrodes).

Powder second-harmonic-generation (SHG) measurements were performed at RT for all the samples and between 108 K and 298 K for $Eu_2MnMn(MnTi_3)O_{12}$ and $Gd_2MnMn(MnTi_3)O_{12}$ on a modified Kurtz[26] nonlinear optical system using 1064 nm light to check the presence or absence of centrosymmetry. The experimental details are described in ref. 27. For low-temperature measurements, the samples were put on a sample holder in a

homemade cryostat and cooled using liquid nitrogen.

4.3. Results and discussion

4.3.1. Phase compositions, crystal symmetries, and crystal structure refinements

The $La_2MnMn(MnTi_3)O_{12}$ sample was found to consist of two major perovskite phases and MnO impurity. The perovskite phases were an A-site-ordered quadruple perovskite phase with space group *Im*–3 (about 65 mass %; a = 7.6099 Å) and a $GdFeO_3$-type perovskite phase with space group *Pnma* (about 32 mass %; a = 5.5816 Å, b = 7.9015 Å, and c = 5.6071 Å). The $Dy_2MnMn(MnTi_3)O_{12}$ sample was found to crystallize in the $GdFeO_3$-type *Pnma* perovskite structure (with a small amount of $Dy_2Ti_2O_7$ impurity).[22,28] The $R_2MnMn(MnTi_3)O_{12}$ samples with R = Nd, Eu, and Gd adopted the A-site columnar-ordered quadruple perovskite structure. The lattice parameters as a function of the R^{3+} ionic radius[29] are plotted in **Figure 4.1.**. we used the radii for 8-fold coordination as radii for 10-fold coordination are not available. The R = Eu sample contained a small amount of cubic $Eu_2Ti_2O_7$ impurity, and the R = Gd sample – cubic $Gd_2Ti_2O_7$ and $GdFeO_3$-type perovskite impurities.

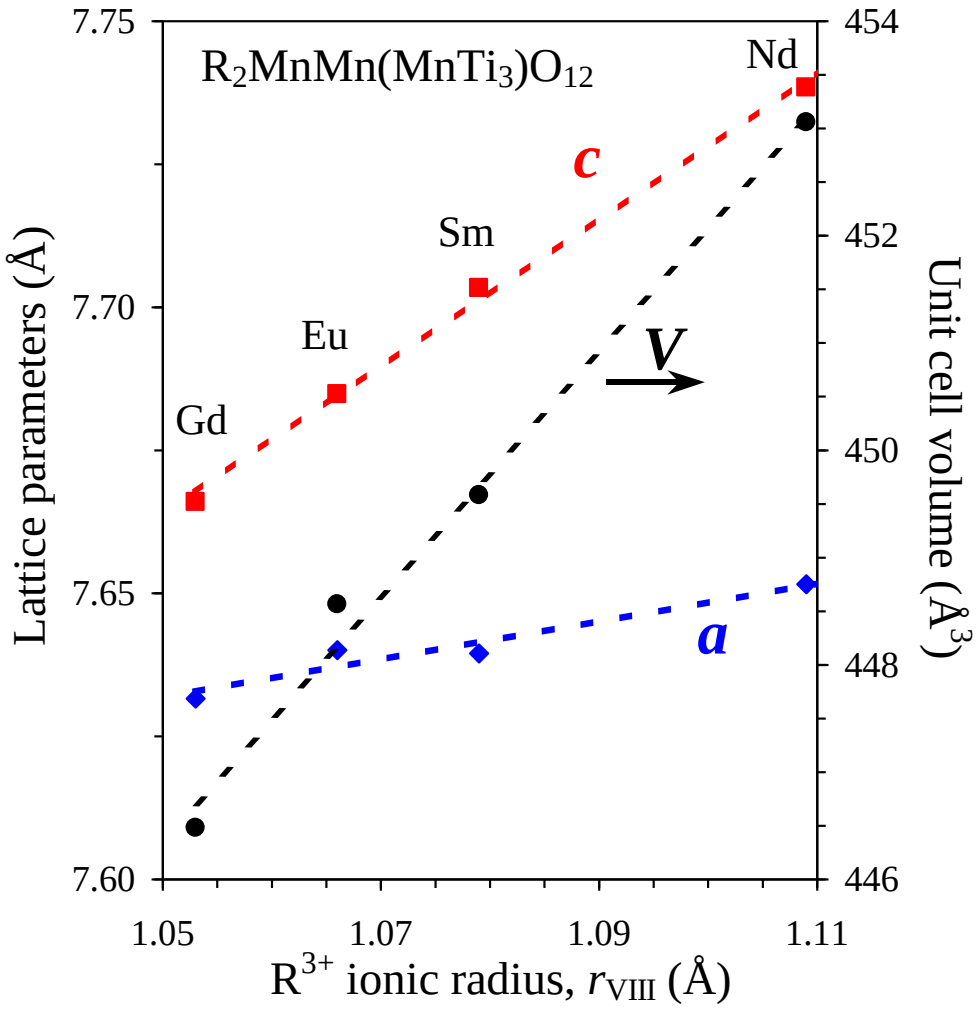

Figure 4.1. Compositional dependence of the lattice parameters (*a* and *c* (space group $P4_2/nmc$): the left-hand axis) and unit cell volume (the right-hand axis) in $R_2MnMn(MnTi_3)O_{12}$ with R = Nd, Sm,[22] Eu, and Gd as a function of the ionic radius in 8-fold coordination. Broken lines are linear fits. Numbers give the ferrimagnetic temperatures, T_c.

Structure parameters of $Sm_2MnMn(Mn_{4-x}Ti_x)O_{12}$ were used as the initial model for the crystal structure refinements of $R_2MnMn(MnTi_3)O_{12}$ with R = Nd, Eu, and Gd.[22] They were found to crystallize in the parent structure of the A-site columnar-ordered quadruple perovskite family with space group $P4_2/nmc$ (No. 137).[19] No SHG signals were detected at RT in all the samples confirming the centrosymmetric structure. Refinements of occupation factors (*g*) showed that there was antisite disorder of R^{3+} and Mn^{2+} cations between the R and Mn1 sites

(corresponding to A and A′ sites, respectively, in the generic chemical formula $A_2A'A''B_4O_{12}$). We also found that the cations at the square-planar Mn1 site are split from the ideal 2a site (0.75, 0.25, 0.75) with the occupation factor g = 1 to a 4*c* site (0.75, 0.25, *z*) with g = 0.5. For example, the refined g values deviated noticeably from the expected values in $Eu_2MnMn(MnTi_3)O_{12}$ (g(Eu) = 0.952(2) and g(Mn1) = 0.635(2)) and especially in $Gd_2MnMn(MnTi_3)O_{12}$ (g(Gd) = 0.916(2) and g(Mn1) = 0.760(3)). On the other hand, the refined g(Mn2) values were close to 1 (e.g., g(Mn2) = 0.984(4) in $Eu_2MnMn(MnTi_3)O_{12}$). Therefore, in the final stages of the refinements, we fixed g(Mn2) at 1, and the antisite disorder of R^{3+} and Mn^{2+} cations between the R and Mn1 sites was refined with constraints g(Mn) = 1 – g(R) for the R site (4d) and g(Mn1) = g(R) – 0.5 and g(R1) = 1 – g(R) for the split Mn1 site (4c), where only the g(R) parameter was refined, to keep the total chemical compositions at the nominal values. Refined structural parameters, primary bond lengths, and bond-valence sums (BVS)[30] are summarized in **Tables 4.1. and 4.2.**, and experimental, calculated, and difference synchrotron XRPD patterns are shown in **Figure 4.2** for $Eu_2MnMn(MnTi_3)O_{12}$ as an example.

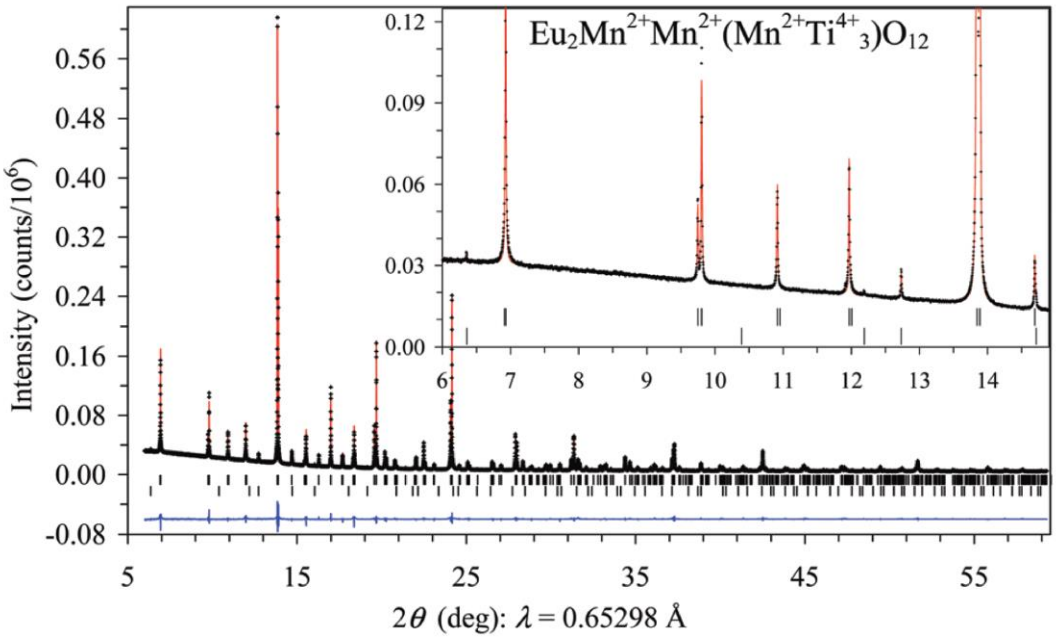

Figure 4.2. Experimental (black crosses), calculated (red line) and difference (blue line) synchrotron X-ray powder diffraction patterns for $Eu_2MnMn(MnTi_3)O_{12}$ at T = 295 K. The tick marks show possible Bragg reflection positions of the main perovskite phase (the first row) and $Eu_2Ti_2O_7$ impurity (the second row). The inset shows an enlarged fragment (no experimental reflections were observed below 6 degrees). An ideal cation distribution with the oxidation states for $Eu_2MnMn(MnTi_3)O_{12}$ is written.

Table 4.1. Structure Parameters of $R_2MnMn(MnTi_3)O_{12}$ with R = Nd, Eu, and Gd at *T* = 295 K from Synchrotron X-ray Powder Diffraction Data

R	Nd	Eu	Gd
a (Å)	7.65158(1)	7.64005(1)	7.63162(1)
c (Å)	7.73843(2)	7.68483(1)	7.66601(2)
V (Å^3)	453.0594(17)	448.5660(9)	446.4803(15)
g(R)	0.9158(11)Nd+ 0.0842Mn	0.9158(10)Eu+ 0.0842Mn	0.8482(13)Gd+ 0.1518Mn
z(R)	0.22500(5)	0.22206(4)	0.22122(5)
B(R) (Å^2)	0.645(9)	0.636(7)	0.493(9)
g(Mn1)	0.4158Mn+ 0.0842Nd	0.4158Mn+ 0.0842Eu	0.3482Mn+ 0.1518Gd
z(Mn1)	0.7931(3)	0.7939(3)	0.7960(3)
B(Mn1) (Å^2)	1.43(6)	1.46(6)	1.23(7)
g(Mn2)	1Mn	1Mn	1Mn
B(Mn2) (Å^2)	0.27(5)	0.11(4)	0.49(7)
g(Mn/Ti)	0.25Mn+0.75Ti	0.25Mn+0.75Ti	0.25Mn+0.75Ti
B(Mn/Ti) (Å^2)	0.459(12)	0.508(11)	0.418(13)
y(O1)	0.0613(4)	0.0656(4)	0.0697(5)
z(O1)	–0.0357(5)	–0.0372(4)	–0.0382(6)
B(O1) (Å^2)	0.61(7)	0.76(6)	0.66(9)
y(O2)	0.5408(4)	0.5393(4)	0.5398(5)
z(O2)	0.5693(4)	0.5729(4)	0.5679(5)
B(O2) (Å^2)	1.05(8)	0.88(7)	1.02(10)
x(O3)	0.4474(2)	0.4463(3)	0.4470(4)
B(O3) (Å^2)	1.01(7)	1.22(7)	1.39(11)
R_{wp} (%)	2.52	3.16	3.85

R_p (%)	1.78	2.16	2.48
R_I (%)	6.11	4.21	4.28
R_F (%)	3.02	2.07	1.64
Impurities	-	$Eu_2Ti_2O_7$: 0.9 %	$Gd_2Ti_2O_7$: 2.7 %
			Pnma-per.: 3.5 %

Crystal data: space group $P4_2/nmc$ (No. 137, cell choice 2), $Z = 2$. R – 4*d* site (0.25, 0.25, *z*); Mn1 – 4*c* site (0.75, 0.25, *z*) near 2*a* site (0.75, 0.25, 0.75); Mn2 – 2*b* site (0.75, 0.25, 0.25); Mn/Ti – 8*e* site (0, 0, 0); O1 and O2 – 8*g* site (0.25, *y*, *z*), and O3 – 8*f* site (*x*, –*x*, 0.25). *g*(O1) = *g*(O2) = *g*(O3) = 1, were *g* is the occupation factor. *Pnma*-per.: a $GdFeO_3$-type perovskite phase with *Pnma* symmetry.

Table 4.2. Bond Lengths, Bond Angles, Bond-Valence Sum (BVS), and Distortion Parameters of $(Mn/Ti)O_6$ (Δ) in $R_2MnMn(MnTi_3)O_{12}$ with R = Nd, Eu, and Gd at T = 295 K

R	Nd	Eu	Gd
R–O1 (Å) ×2	2.349(4)	2.326(3)	2.301(4)
R–O1 (Å) ×2	2.481(3)	2.440(3)	2.419(4)
R–O2 (Å) ×2	2.531(3)	2.490(3)	2.505(4)
R–O3 (Å) ×4	2.771(1)	2.771(1)	2.767(1)
BVS(R^{3+})	+3.15	+3.03	+3.04
Mn1–O3 (Å) ×4	2.162(3)	2.147(3)	2.155(4)
Mn1–O2 (Å) ×2	2.670(4)	2.681(3)	2.631(4)
Mn1–O1 (Å) ×2	3.033(4)	3.051(3)	3.066(4)
Mn1–Mn1	0.667(4)	0.675(4)	0.705(4)
BVS($Mn1^{2+}$)	+1.72	+1.77	+1.76
Mn2–O2 (Å) ×4	2.125(3)	2.108(3)	2.126(4)
Mn2–O1 (Å) ×4	2.902(3)	2.913(3)	2.930(4)
BVS($Mn2^{2+}$)	+1.81	+1.89	+1.79
Mn/Ti–O1 (Å) ×2	1.989(1)	1.995(1)	2.002(1)
Mn/Ti–O2 (Å) ×2	2.011(1)	2.013(1)	2.001(1)
Mn/Ti–O3 (Å) ×2	2.017(1)	2.007(1)	2.000(1)

Δ(Mn/Ti)	3.6×10^{-5}	1.4×10^{-5}	1.8×10^{-7}
BVS(M^{n+})	+3.53	+3.53	+3.57
Mn/Ti–O1–Mn/Ti ×2	148.25(8)	144.06(7)	147.22(8)
Mn/Ti–O2–Mn/Ti ×2	146.39(8)	143.18(7)	146.36(8)
Mn/Ti–O3–Mn/Ti ×2	144.71(8)	144.93(7)	146.77(8)

BVS = $\sum_{i=1}^{N} v_i$, $v_i = \exp[(R_0 - l_i)/B]$, N is the coordination number, $B = 0.37$, $R_0(Nd^{3+}) = 2.117$, $R_0(Eu^{3+}) = 2.076$, $R_0(Gd^{3+}) = 2.065$, $R_0(Mn^{2+}) = 1.79$, $R_0(Ti^{4+}) = 1.815$, and $R_0(M^{n+}) = 1.809$ (an average of $3Ti^{4+} + Mn^{2+}$).[29]

The BVS values for the R sites (+3.03 to +3.15) were close to the expected value of +3 in all the samples. The BVS values of the Mn1 and Mn2 sites (+1.72 to +1.89) supported the +2 oxidation state of Mn as expected from the stoichiometry and the initial use of MnO. Because of the statistical distribution of Mn^{2+} and $3Ti^{4+}$ at the Mn/Ti site the BVS values were calculated using an average R_0 value of 1.809. The BVS values calculated in such a way (+3.53 to +3.57) were close to the expected average oxidation state of +3.5 for the Mn/Ti site.

The antisite disorder of R^{3+} and Mn^{2+} cations increases for the smallest rare-earth cation with R = Gd, where this structure is still stable (at the synthesis conditions used). In addition, a small amount of a *Pnma* modification appeared in the $Gd_2MnMn(MnTi_3)O_{12}$ sample as an impurity, and $Dy_2MnMn(MnTi_3)O_{12}$ already crystallizes in the *Pnma*-type structure.[28] A complete disorder of R^{3+} and Mn^{2+} cations at the perovskite A site is realized in the *Pnma*-type structure. Therefore, when the difference in the ionic radii of the R^{3+} and Mn^{2+} cations decreases, the R^{3+} and Mn^{2+} cation antisite disorder increases, and this disorder finally leads to the destabilization of the A-site columnar-ordered structure.

4.3.2 Magnetic Properties of $R_2MnMn(MnTi_3)O_{12}$

Figure 4.3.–4.5. show ZFC and FCC magnetic susceptibility curves (χ versus T) of $R_2MnMn(MnTi_3)O_{12}$ measured at H = 100 Oe and 10 kOe. All the samples demonstrated sharp increases of FCC susceptibilities below T_c = 20 K (R = Nd), 30 K (R = Eu), and 42 K (R = Gd), where T_C was determined from sharp peaks on the 100 Oe FCC dχT/dT versus T curves. These sharp increases indicated the development of large uncompensated ferromagnetic moments. There was a clear divergence between the 100 Oe ZFC and FCC curves just below T_C, while the 10 kOe ZFC and FCC curves almost coincided with each other. Both 100 Oe and 10 kOe FCC curves of $Nd_2MnMn(MnTi_3)O_{12}$ showed maxima (near 9–11 K) and a decrease of susceptibilities at lower temperatures. This behavior could be caused by the ordering of the Nd^{3+} sublattice in the opposite direction compared with the Mn^{2+} sublattices.

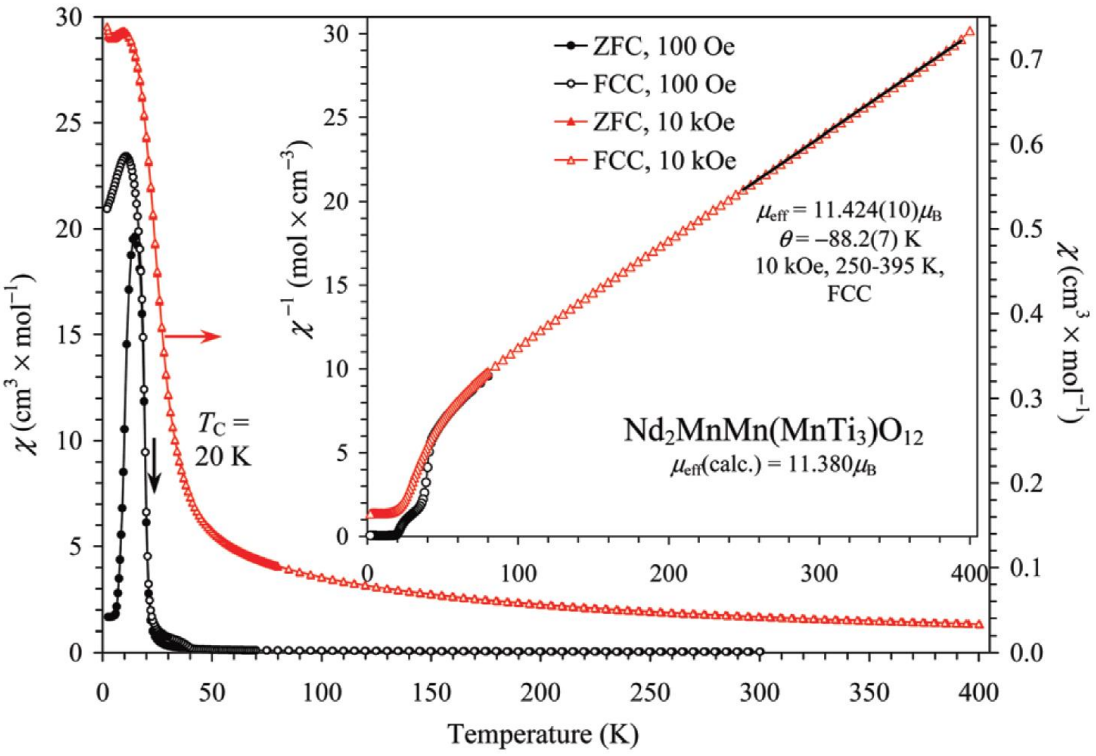

Figure 4.3. ZFC (filled symbols) and FCC (empty symbols) dc magnetic susceptibility (χ = M/H) curves of $Nd_2MnMn(MnTi_3)O_{12}$ measured at 100 Oe (black, circles; left-hand axes) and 10 kOe (red, triangles; right-hand axes). The inset gives the FCC χ^{-1} versus T curves at 100 Oe and 10 kOe with the Curie–Weiss fit. Anomalies near 40 K (at 100 Oe) are most probably originated from an impurity (for example, they are close to T_c of Mn_3O_4).

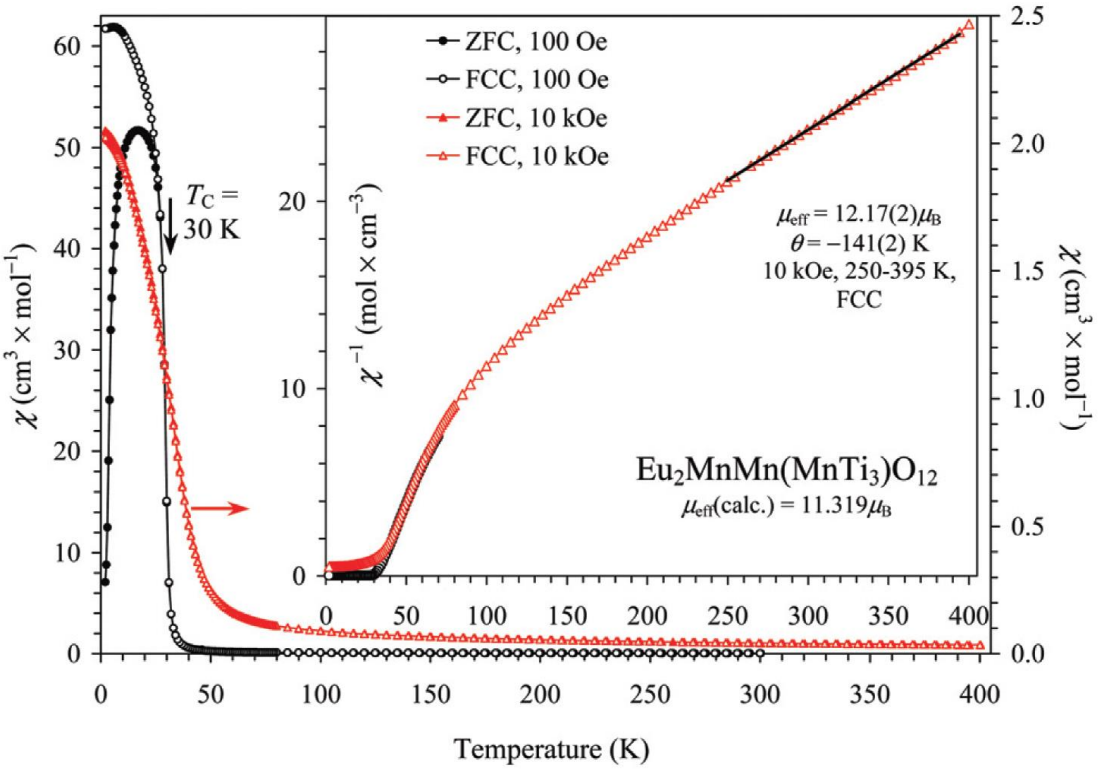

Figure 4.4. ZFC (filled symbols) and FCC (empty symbols) dc magnetic susceptibility (χ = M/H) curves of $Eu_2MnMn(MnTi_3)O_{12}$ measured at 100 Oe (black, circles; left-hand axes) and 10 kOe (red, triangles; righthand axes). The inset gives the FCC χ^{-1} versus T curves at 100 Oe and 10 kOe with the Curie–Weiss fit.

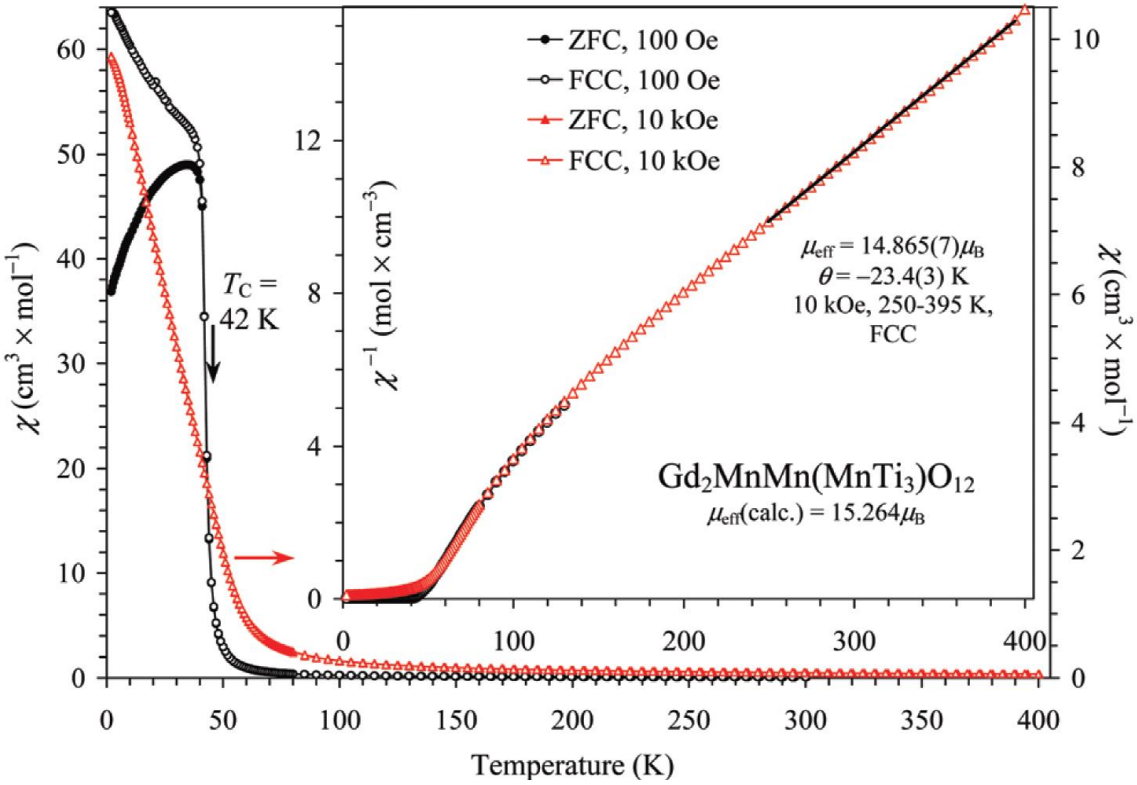

Figure 4.5. ZFC (filled symbols) and FCC (empty symbols) dc magnetic susceptibility (χ = M/H) curves of $Gd_2MnMn(MnTi_3)O_{12}$ measured at 100 Oe (black, circles; left-hand axes) and 10 kOe (red, triangles; righthand axes). The inset gives the FCC χ^{-1} versus T curves at 100 Oe and 10 kOe with the Curie–Weiss fit.

Inverse magnetic susceptibilities followed the Curie–Weiss law at high temperatures above about 200 K (insets of **Figure 4.3.–4.5.**). However, noticeable deviations developed below 200 K, and the deviations enhanced when approaching T_C. This behavior of χ^{-1} versus T curves is typical for ferrimagnetic materials.[28,31] Parameters of the Curie–Weiss fits are summarized in **Table 4.3**.

Table 4.3. Temperatures of Magnetic Anomalies and Parameters of Curie-Weiss Fits and *M* versus *H* Curves at *T* = 5 K for $R_2MnMn(MnTi_3)O_{12}$ with R = Nd, Eu, and Gd

R	T_{SG} (K)	μ_{eff} (μ_B/f.u.)	μ_{calc} (μ_B/f.u.)	θ (K)	M_S (μ_B/f.u.)	M_R (μ_B/f.u.)	H_C (Oe)
Nd	20	11.424(10)	11.380	–88.2(7)	3.62	0.52	~770
Eu	30	12.17(2)	11.319	–141(2)	5.43	0.26	~30
Gd	42	14.865(7)	15.264	–23.4(3)	18.6	0.25	~30

Curie–Weiss fits were performed between 250 and 395 K using the FCC χ^{-1} versus T data at 10 kOe. M_S is the magnetization value at T = 5 K and H = 70 kOe. M_R is the remnant magnetization at 5 K and H = 0 Oe, and H_C is the coercive field at 5 K. For μ_{calc}, we used 3.5μ_B for Nd^{3+}, 3.4μ_B for Eu^{3+}, and 8.0μ_B for Gd^{3+}.[30]

Isothermal *M versus H* curves showed step-like hysteresis with very small coercive fields H_C (about 30 Oe for R = Eu and Gd and about 770 Oe for R = Nd) that is typical for soft ferrimagnetic materials (**Figure 4.6.**). The extrapolated remnant magnetization, M_R(extra.), at T = 5 K obtained by the extrapolation between 40 kOe and 70 kOe to zero fields reached about 1.4 μ_B per f.u. for R = Nd, 4.0 μ_B per f.u. for R = Eu, and 17.6 μ_B per f.u. for R = Gd. Eu^{3+} cations are usually considered as non-magnetic;[31] therefore, its M_R(extra.) of 4.0 μ_B per f.u. can be explained by the ferromagnetic ordering of Mn^{2+} at the A′ and A″ sites and an antiferromagnetic arrangement of Mn^{2+} at the B site.[22] The slightly reduced moment (compared with the expected one of 5.0 μ_B per f.u.) can be caused by some frustration at the A′ and A″ sites or a very small contribution from an antiferromagnetic arrangement of Eu^{3+} cations. The reduced Mn^{2+} moments at the A′ and A″ sites were observed in $Ca_{1.4}Mn_{0.6}Ti_2O_6$,[18] $Sm_2MnMn(Mn_{4-x}Ti_x)O_{12}$ [32] and $NaDyMn_2Ti_4O_{12}$.[33] The maximum ordered moment of a Gd^{3+}

cation is 7 μ_B. Therefore, the M_R(extra.) value of 17.6 μ_B per f.u. in $Gd_2MnMn(MnTi_3)O_{12}$ can be explained by the same spin ordering of Mn^{2+} cations plus a ferromagnetic arrangement of all Gd^{3+} cations in the same direction as the total moment of Mn^{2+} cations. On the other hand, the reduced M_R(extra.) value of 1.4 μ_B per f.u. in $Nd_2MnMn(MnTi_3)O_{12}$ can be caused by the same spin ordering of Mn^{2+} cations plus an antiferromagnetic arrangement Nd^{3+} cations (that is, in the opposite direction to the total moment of Mn^{2+} cations). Therefore, *M* versus *H* and χ versus *T* data of $Nd_2MnMn(MnTi_3)O_{12}$ are consistent with each other. Magnetic measurements gave evidence that ferrimagnetic structures are realized in all $R_2MnMn(MnTi_3)O_{12}$. $Gd_2MnMn(MnTi_3)O_{12}$ has the largest transition temperature and the largest ordered moment among other members of this series.

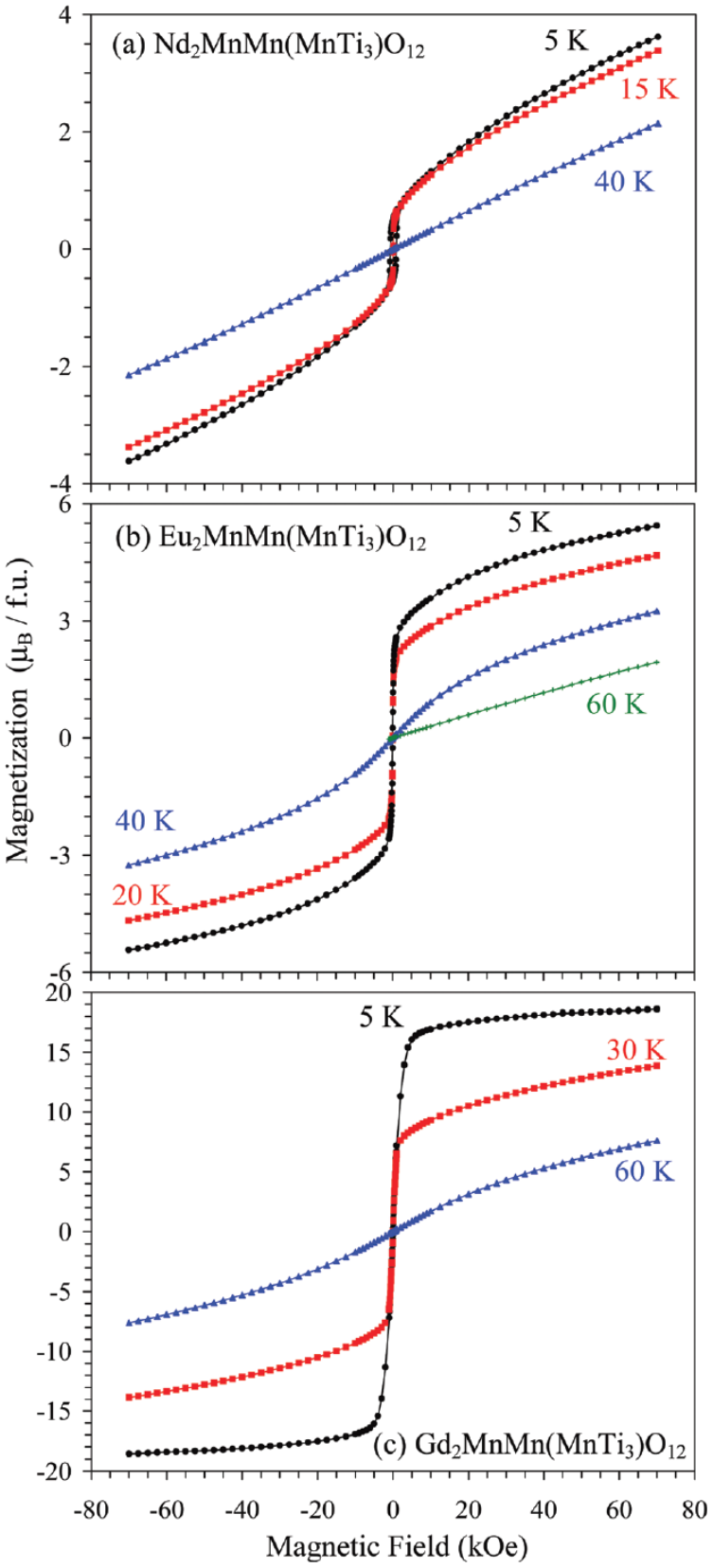

Figure 4.6. *M* versus *H* curves of $R_2MnMn(MnTi_3)O_{12}$ for (a) R = Nd, (b) R = Eu, and (c) R = Gd at different temperatures.

Results of specific heat measurements of $R_2MnMn(MnTi_3)O_{12}$ at H = 0 and 90 kOe are given in **Figure 4.7**. Weak anomalies were observed at T_C for R = Nd and Eu, while specific heat anomalies were significantly larger for R = Gd. These results confirmed long-range magnetic ordering. Additional strong anomalies, centered at about 5 K, were observed for R = Nd, and Gd. These results confirmed contributions of these rare-earth cations into long-range ordering. Note that additional weak anomalies were also observed in the R = Eu sample near 7 K. A magnetic field of 90 kOe shifted magnetic entropy to temperatures much higher than T_C: the effect of the 90 kOe magnetic field was observed from about 65 K for R = Nd, 90 K for R = Eu, and 130 K for R = Gd.

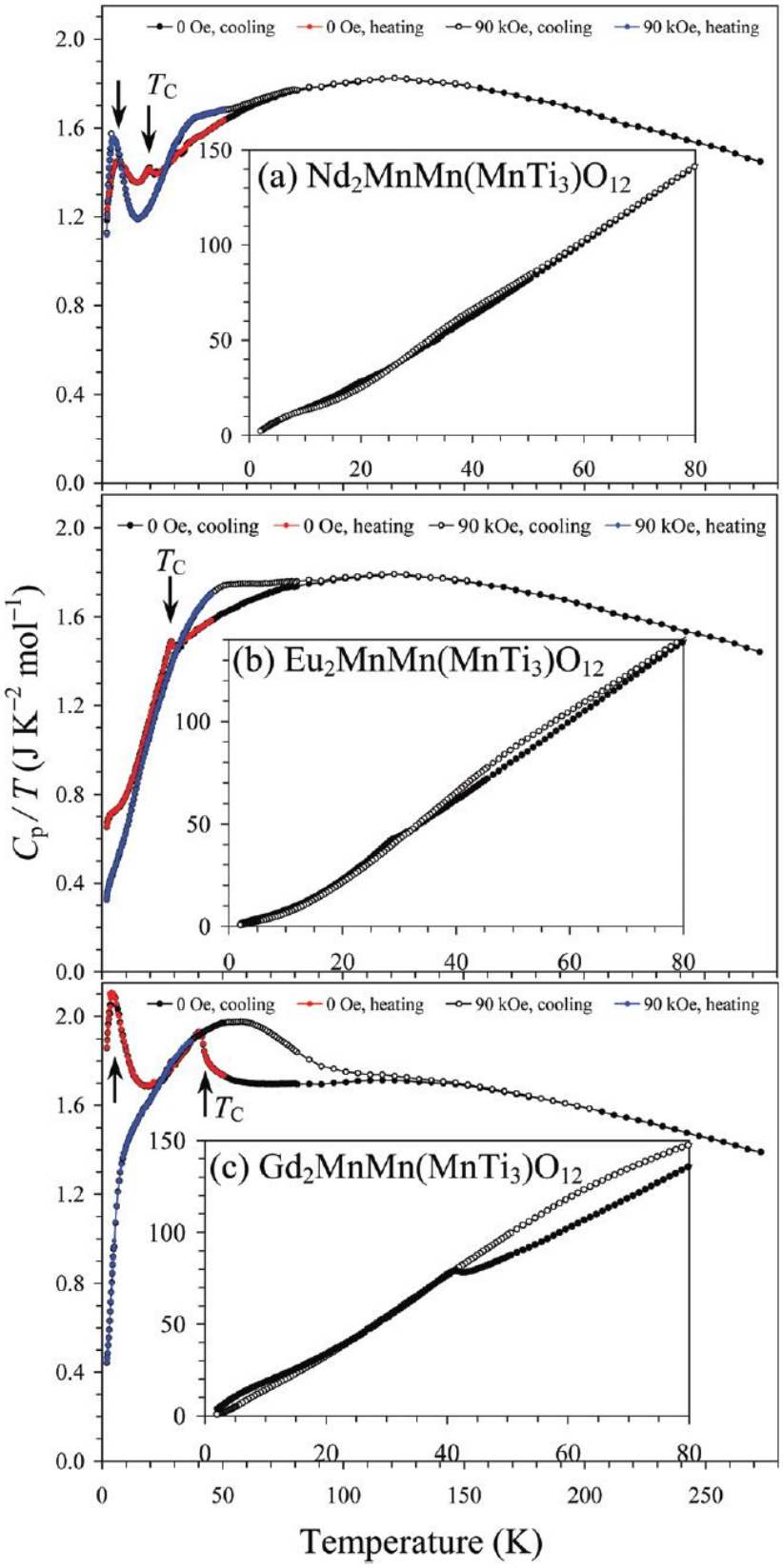

Figure 4.7. Specific heat data of $R_2MnMn(MnTi_3)O_{12}$ for (a) R = Nd, (b) R = Eu, and (c) R = Gd, plotted as C_p/T versus T. Measurements were performed on cooling and heating at H = 0

Oe and 90 kOe. Insets present the C_p (in J K^{-1} mol^{-1}) versus T curves at H = 0 Oe and 90 kOe on cooling below 80 K. Arrows show magnetic anomalies at H = 0 Oe.

4.3.3. Dielectric Properties of $R_2MnMn(MnTi_3)O_{12}$

Dielectric constant and loss of $Gd_2MnMn(MnTi_3)O_{12}$ as functions of temperature and frequency are given in **Figure 4.8.** Broad maxima were observed on dielectric constant near 240 K at a frequency of 100 Hz and 260 K at a frequency of 665 kHz – this behavior is typical for relaxor-type ferroelectrics. At higher temperatures and at low frequencies, the dielectric constant increases most probably due to an extrinsic Maxwell–Wagner relaxation. **Figure 4.9.** gives a dielectric constant of $R_2MnMn(MnTi_3)O_{12}$ at H = 0 Oe and 90 kOe and one frequency of 665 kHz. All the samples showed broad dielectric constant anomalies near 250 K (R = Eu), 260 K (R = Gd), and 295 K (R = Nd) at this frequency. The magnetic field of 90 kOe had almost no effects on the dielectric constant values and peak positions, and no dielectric anomalies were observed at the magnetic transition temperatures. This fact shows that magnetic and ferroelectric-like properties have different origins, like in $BiFeO_3$,[34] and the coupling between magnetism and ferroelectricity is very weak.

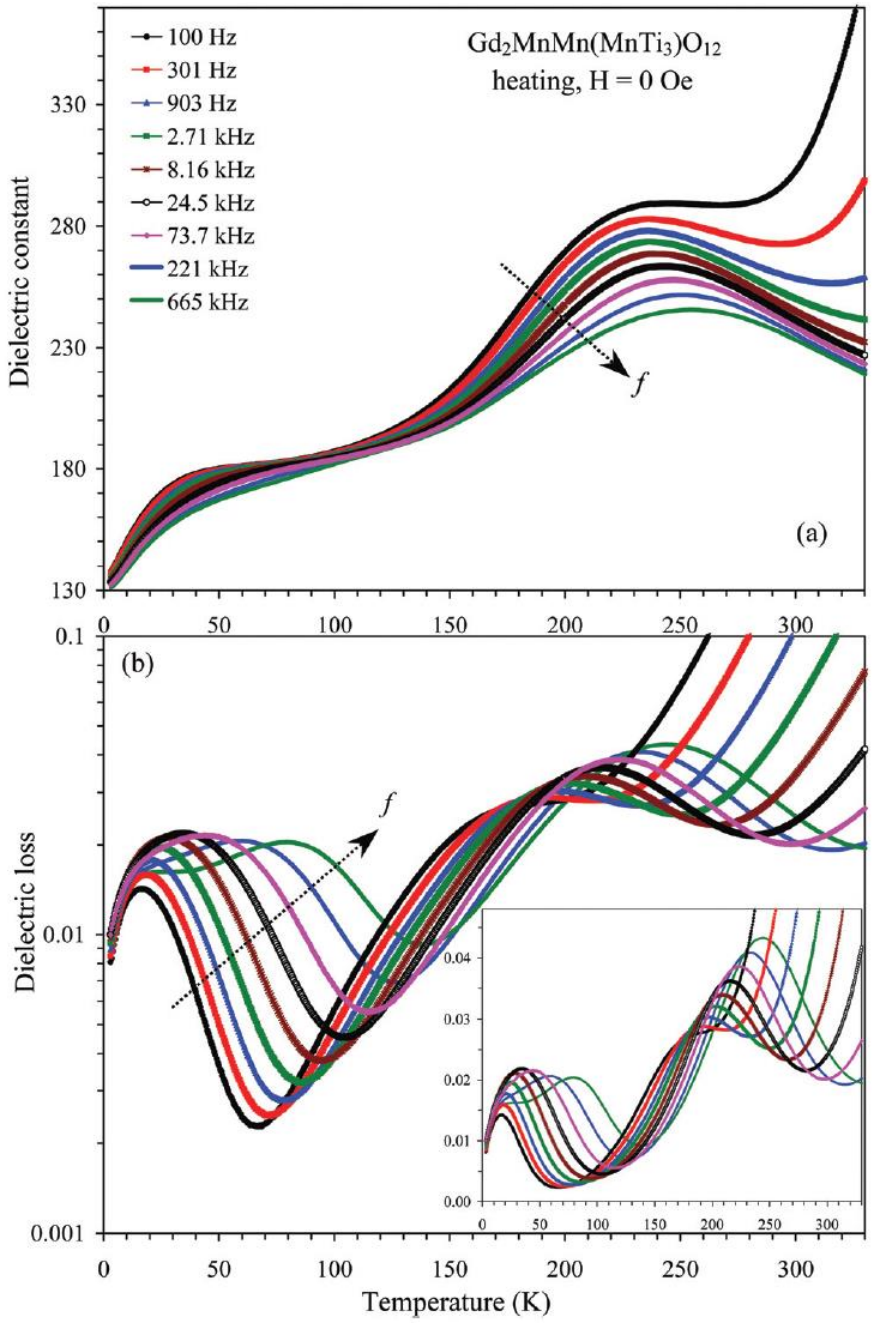

Figure 4.8. (a) Frequency-dependent (100 Hz–665 kHz) dielectric constant of $Gd_2MnMn(MnTi_3)O_{12}$ as a function of temperature measured at H = 0 Oe on heating. (b) The corresponding frequency-dependent dielectric loss of $Gd_2MnMn(MnTi_3)O_{12}$, plotted in the logarithmic scale. Inset gives the same dielectric loss in the linear scale.

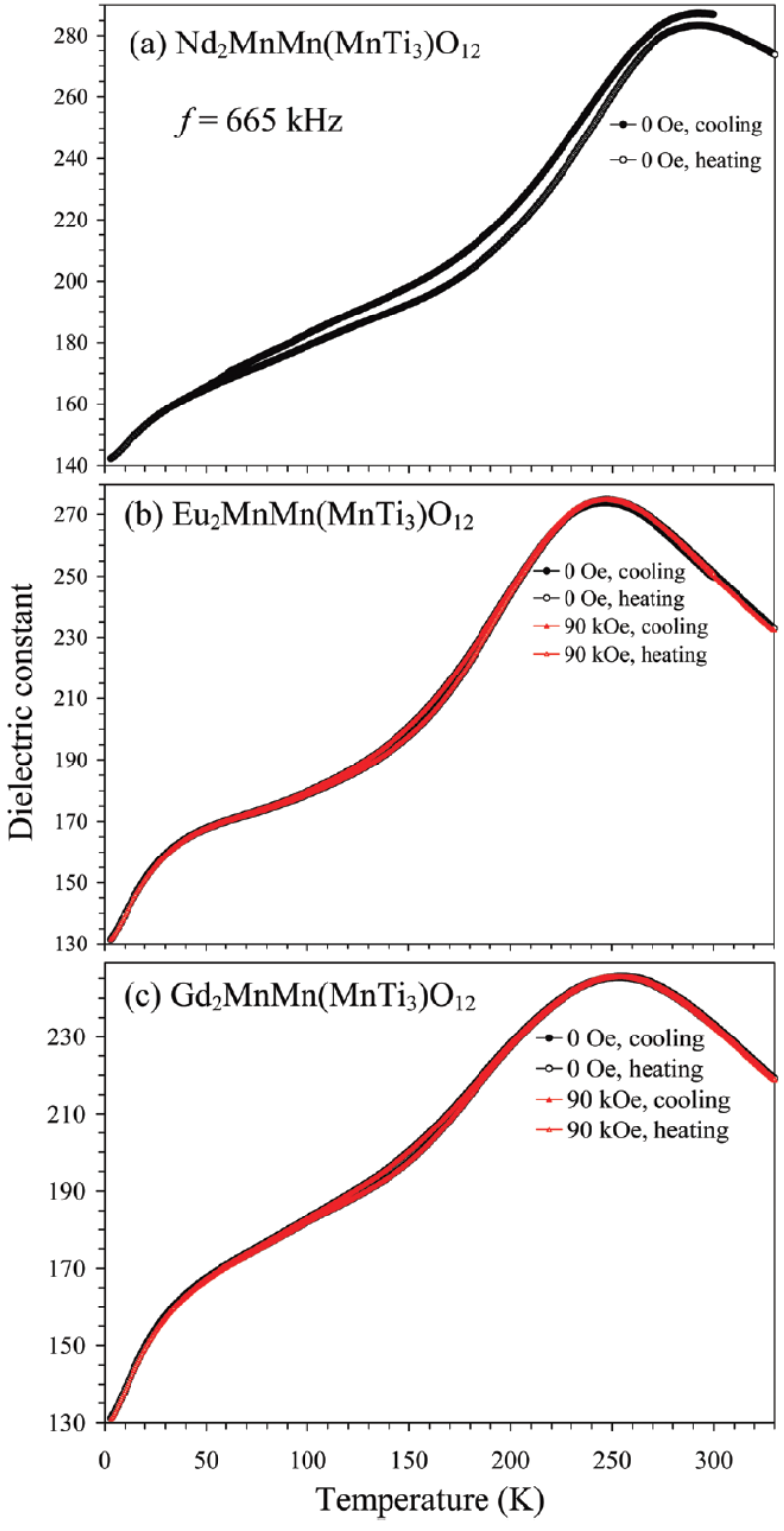

Figure 4.9. Temperature dependence of dielectric constant of $R_2MnMn(MnTi_3)O_{12}$ for (a) R = Nd, (b) R = Eu, and (c) R = Gd. Measurements were performed on cooling and heating at *H* = 0 Oe (black) and 90 kOe (red). Data at one frequency of 665 kHz are shown for clarity.

4.3.3. Ferroelectric properties of $R_2MnMn(MnTi_3)O_{12}$

Typical impedance data are plotted in **Figure 4.10.** together with the fitting results and an equivalent circuit. The data were fitted by two R-CPE elements representing grain and grain boundary contributions. The temperature dependence of the obtained resistivity is given in **Figure 4.11.** for R = Eu and Gd as examples. Both samples were quite resistive with resistivity exceeding 108 Ohm*cm at RT. Near and above RT the resistivity followed the activation law with the activation energy of about 0.5 eV.

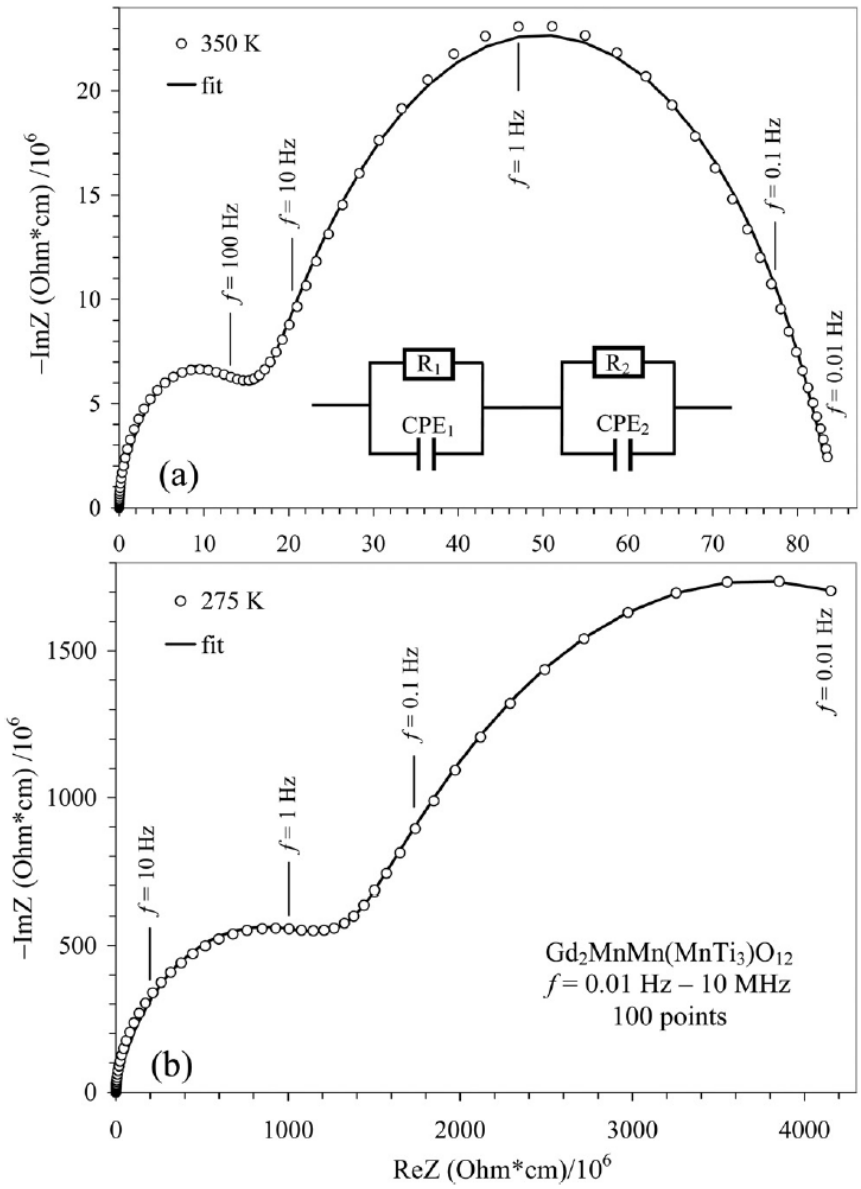

Figure 4.10. Impedance Re*Z* versus -Im*Z* plots for $Gd_2MnMn(MnTi_3)O_{12}$ at two selected temperatures (a) T = 350 K and (b) T = 275 K. Experimental points are shown by circles and fitting results are given by line. The equivalent circuit used for the fittings is shown on panel (a). *R*: a resistor, CPE: a constant phase element.

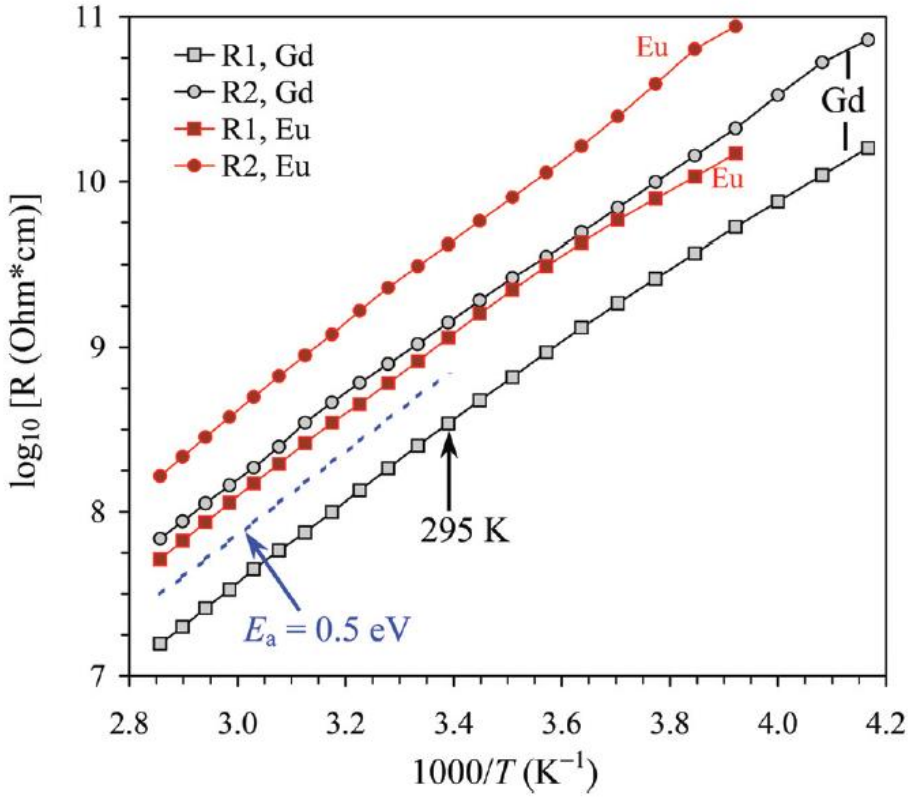

Figure 4.11. Temperature dependence of resistivity obtained from the impedance measurements for $Eu_2MnMn(MnTi_3)O_{12}$ and $Gd_2MnMn(MnTi_3)O_{12}$, plotted as $\log_{10}R$ versus 1000/*T*. *R*1 is usually interpreted as grain resistivity, and *R*2 – as grain boundary resistivity. *E*a: activation energy.

No SHG signals were observed in $R_2MnMn(MnTi_3)O_{12}$ at low temperatures (down to 108 K). This feature could be realized if the correlation length of local polar distortions is shorter than the optical wavelength. As SHG measurements did not detect polar distortions we performed *P*–*E* loop measurements at 77 K. At RT, the resistivity was not high enough to apply high voltage. The results are summarized in **Figure 4.12**. Saturated *P*–*E* loops could not be reached under the maximum electric fields of 130–160 kV cm^{-1} that we could apply in the case of R = Nd and Eu, but the shape of the *P*–*E* loops (**Figure 4.12.** b and c) was typical for ferroelectric materials (for which saturation was not reached) or for relaxor ferroelectrics.

Moreover, the switching current accompanied by polarization reversal was observed. In the case of $Gd_2MnMn(MnTi_3)O_{12}$, the leakage current was dominated even at 77 K (**Figure 4.12.** d); this result was in agreement with the more conductive nature of $Gd_2MnMn(MnTi_3)O_{12}$ (**Figure 4.11.**). Relaxor-type ferroelectric properties in perovskite materials are usually observed in ferroelectric solid solutions, often containing Pb^{2+} and Bi^{3+} cations, where there is compositional inhomogeneity on the local level, and there exist polar nano regions and local off-center displacements of cations.[4,35–37] We observed antisite disorder in $R_2MnMn(MnTi_3)O_{12}$, which could slightly vary on local scales producing the required compositional inhomogeneity. There is also statistical distribution of Mn^{2+} and Ti^{4+} cations in one B site. The ferroelectric transition at 630 K in the parent compound, $CaMnTi_2O_6$,[17,18] is driven by long-range cooperative displacements of Mn^{2+} cations at the square-planar A′ sites in one direction from the square-planar units and by cooperative displacements of Ti^{4+} cations at the B site. Due to antisite disorder involving the square-planar A′ sites and statistical occupation at the B site in $R_2MnMn(MnTi_3)O_{12}$, long-range cooperative displacements of cations will be disturbed, while short-range cation displacements at the A′ and B sites could survive resulting in relaxor-like ferroelectric transitions with significantly lower transition temperatures in comparison with $CaMnTi_2O_6$. The general mechanisms of relaxor-like properties of $R_2MnMn(MnTi_3)O_{12}$ and usual ABO_3 perovskites might be the same. Therefore, $R_2MnMn(MnTi_3)O_{12}$ could be analogs of classical relaxors, such as $PbMg_{1/3}Nb_{2/3}O_3$ and $PbSc_{1/2}Ta_{1/2}O_3$, in the A-site columnar-ordered perovskite family, and investigations of solid solutions between $R_2MnMn(MnTi_3)O_{12}$ and ferroelectric $CaMnTi_2O_6$ might be interesting.

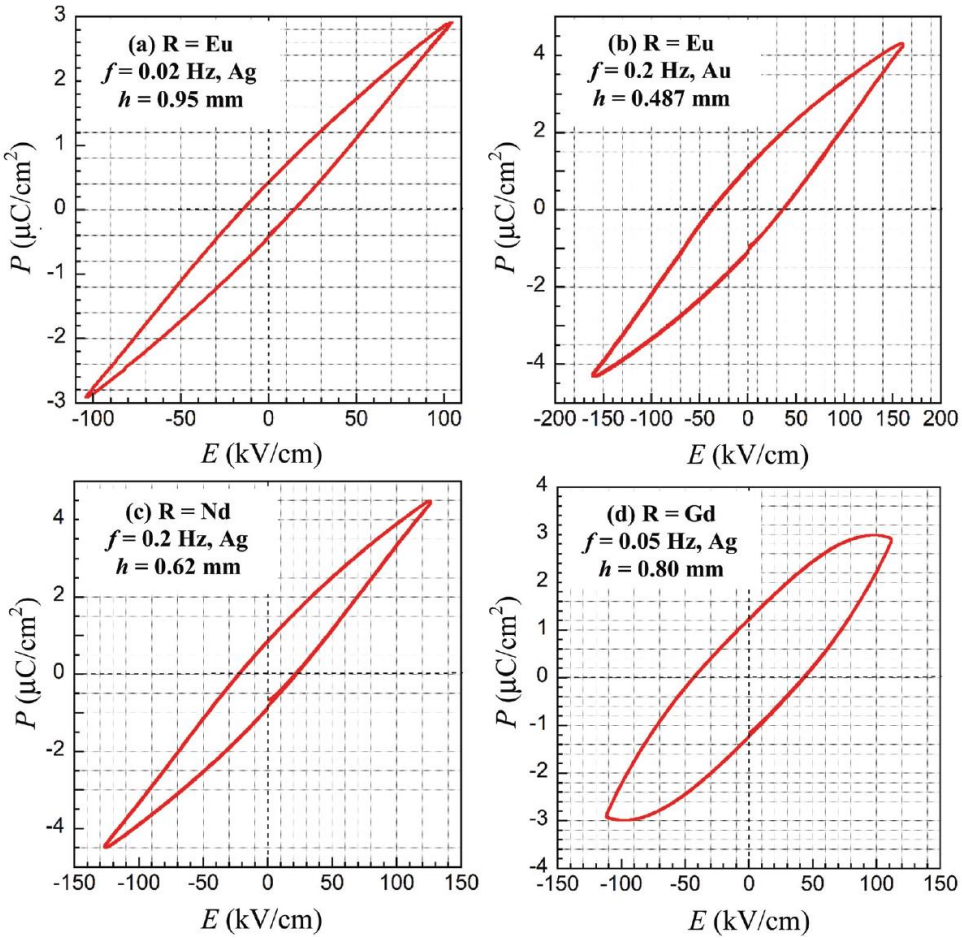

Figure 4.12. *P–E* hysteresis loops at T = 77 K for (a and b) $Eu_2MnMn(MnTi_3)O_{12}$, (c) $Nd_2MnMn(MnTi_3)O_{12}$ and (d) $Gd_2MnMn(MnTi_3)O_{12}$.

4.4. Summary of Chapter 4

New members of the A-site columnar-ordered quadruple perovskite family, $R_2MnMn(MnTi_3)O_{12}$ with R = Nd, Eu, and Gd were prepared by the high-pressure and high-temperature method. Their crystal structures were studied by synchrotron powder X-ray diffraction at room temperature. Their magnetic, dielectric and ferroelectric properties were also investigated. They exhibit broad dielectric constant anomalies just below room temperature typical for relaxor ferroelectrics. They show long-range ferrimagnetic transitions below 20 K (R = Nd), 30 K (R = Eu), and 42 K (R = Gd) with large uncompensated moments. Their properties are drastically different from the ferroelectric and antiferromagnetic properties of parent $Ca_2MnMnTi_4O_{12}$.

References in Chapter 4

1. R. H. Mitchell, *Perovskites: Modern and Ancient*; Almaz Press: Thunder Bay, Ontario, Canada, **2002**.
2. A. M. Abakumov, A. A. Tsirlin and E. V. Antipov, *Transition-Metal Perovskites*. In *Comprehensive Inorganic Chemistry II (Second Edition): From Elements to Applications*, eds. J. Reedijk and K. R. Poeppelmeier, Elsevier: Amsterdam, **2013**, *2*, 1-40.
3. N. Izyumskaya, Y. Alivov and H. Morkoç, Oxides, oxides, and more oxides: high-κ oxides, ferroelectrics, ferromagnetics, and multiferroics, *Crit. Rev. Solid State Mater. Sci.*, **2009**, *34*, 89-179.
4. F. Li, M. J. Cabral, B. Xu, Z. Cheng, E. C. Dickey, J. M. LeBeau, J. Wang, J. Luo, S. Taylor, W. Hackenberger, L. Bellaiche, Z. Xu, L.-Q. Chen, T. R. Shrout and S. Zhang, Giant piezoelectricity of Sm-doped $Pb(Mg_{1/3}Nb_{2/3})O_3$-$PbTiO_3$ single crystals, *Science*, **2019**, *364*, 264-268.
5. M. V. Talanov, Group-theoretical analysis of 1:3 A-site-ordered perovskite formation, *Acta Cryst.*, **2019**, *A75*, 379-397.
6. F. Mezzadri, G. Calestani, M. Calicchio, E. Gilioli, F. Bolzoni, R. Cabassi, M. Marezio and A. Migliori, Synthesis and characterization of multiferroic $BiMn_7O_{12}$, *Phys. Rev. B: Condens. Matter Mater. Phys.*, **2009**, *79*, 100106(R).
7. W. A. Slawinski, H. Okamoto and H. Fjellvag, Triclinic crystal structure distortion of multiferroic $BiMn_7O_{12}$, *Acta Crystallogr., Sect. B: Struct. Sci. Crystl. Eng. Mater.*, **2017**, *73*, 313-320.
8. A. A. Belik, Y. Matsushita, Y. Kumagai, Y. Katsuya, M. Tanaka, S. Yu. Stefanovich, B. I. Lazoryak, F. Oba and K. Yamaura, Complex structural behavior of $BiMn_7O_{12}$ quadruple perovskite, *Inorg. Chem*., **2017**, *56*, 12272-12281.

9. F. Mezzadri, M. Buzzi, C. Pernechele, G. Calestani, M. Solzi, A. Migliori and E. Gilioli, Polymorphism and multiferroicity in $Bi_{1-x/3}(Mn^{III}_3)(Mn^{III}_{4-x}Mn^{IV}_x)O_{12}$, *Chem. Mater.*, **2011**, *23*, 3628-3635.
10. D. D. Khalyavin, R. D. Johnson, F. Orlandi, P. G. Radaelli, P. Manuel and A. A. Belik, Emergent helical texture of electric dipoles, *Science*, **2020**, *369*, 680-684.
11. W.-T. Chen, C.-W. Wang, H.-C. Wu, F.-C. Chou, H.-D. Yang, A. Simonov and M. S. Senn, Improper ferroelectric polarization in a perovskite driven by intersite charge transfer and ordering, *Phys. Rev. B: Condens. Matter Mater. Phys.*, **2018**, *97*, 144102.
12. A. A. Belik, Y. S. Glazkova, Y. Katsuya, M. Tanaka, A. V. Sobolev and I. A. Presniakov, Low-temperature structural modulations in $CdMn_7O_{12}$, $CaMn_7O_{12}$, $SrMn_7O_{12}$, and $PbMn_7O_{12}$ perovskites studied by synchrotron X-ray powder diffraction and Mossbauer spectroscopy, *J. Phys. Chem. C*, **2016**, *120*, 8278-8288.
13. M. A. Subramanian, D. Li, N. Duan, B. A. Reisner and A. W. Sleight, High dielectric constant in $ACu_3Ti_4O_{12}$ and $ACu_3Ti_3FeO_{12}$ phases, *J. Solid State Chem.*, **2000**, *151*, 323-325.
14. T. B. Adams, D. C. Sinclair and A. R. West, Giant barrier layer capacitance effects in $CaCu_3Ti_4O_{12}$ ceramics, *Adv. Mater.*, **2002**, *14*, 1321-1323.
15. J. Li, M. A. Subramanian, H. D. Rosenfeld, C. Y. Jones, B. H. Toby and A. W. Sleight, Clues to the giant dielectric constant of $CaCu_3Ti_4O_{12}$ in the defect structure of "$SrCu_3Ti_4O_{12}$", *Chem. Mater.*, **2004**, *16*, 5223-5225.
16. L. Liu, S. Ren, J. Liu, F. Han, J. Zhang, B. Peng, D. Wang, A. A. Bokov and Z.-G. Ye, Localized polarons and conductive charge carriers: understanding $CaCu_3Ti_4O_{12}$ over a boad temperature range, *Phys. Rev. B: Condens. Matter Mater. Phys.*, **2019**, *99*, 094110.
17. A. Aimi, D. Mori, K. Hiraki, T. Takahashi, Y. J. Shan, Y. Shirako, J. S. Zhou and Y. Inaguma, High-pressure synthesis of A-site ordered double perovskite $CaMnTi_2O_6$ and

ferroelectricity driven by coupling of A-site ordering and the second-order Jahn–Teller effect, *Chem. Mater*., **2014**, *26*, 2601-2608.

18. Z. Li, Y. Cho, X. Li, X. Li, A. Aimi, Y. Inaguma, J. A. Alonso, M. T. Fernandez-Diaz, J. Yan, M. C. Downer, G. Henkelman, J. B. Goodenough and J. Zhou, New mechanism for ferroelectricity in the perovskite $Ca_{2-x}Mn_xTi_2O_6$ synthesized by spark plasma sintering, *J. Am. Chem. Soc.*, **2018**, *140*, 2214-2220.
19. A. A. Belik, Rise of A-site columnar-ordered $A_2A'A''B_4O_{12}$ quadruple perovskites with intrinsic triple order, *Dalton Trans.,* **2018**, *47*, 3209-3217.
20. M. Fukuda, T. Nishikubo, Z. Pan, Y. Sakai, M.-H. Zhang, S. Kawaguchi, H. W. Yu, Y. Okimoto, S.-Y. Koshihara, M. Itoh, J. Rodel and M. Azuma, Enhanced spontaneous polarization by V^{4+} substitution in a lead-free perovskite $CaMnTi_2O_6$, *Inorg. Chem*., **2020**, *59*, 11749-11756.
21. A. M. Vibhakar , D. D. Khalyavin, P. Manuel, J. Liu, A. A. Belik and R. D. Johnson, Spontaneous rotation of ferrimagnetism driven by antiferromagnetic spin canting, *Phys. Rev. Lett.*, **2020**, *124*, 127201.
22. A. A. Belik, L. Zhang, R. Liu, D. D. Khalyavin, Y. Katsuya, M. Tanaka and K. Yamaura, Valence variations by B-site doping in A-site columnar-ordered quadruple perovskites $Sm_2MnMn(Mn_{4-x}Ti_x)O_{12}$ with $1 \le x \le 3$, *Inorg. Chem*., **2019**, *58*, 3492-3501.
23. M. Tanaka, Y. Katsuya and A. Yamamoto, A new large radius imaging plate camera for high-resolution and high-throughput synchrotron X-ray powder diffraction by multiexposure method, *Rev. Sci. Instrum*., **2008**, *79*, 075106.
24. M. Tanaka, Y. Katsuya, Y. Matsushita and O. Sakata, Development of a synchrotron powder diffractometer with a one-dimensional X-ray detector for analysis of advanced materials, *J. Ceram. Soc. Jpn*., **2013**, *121*, 287-290.
25. F. Izumi and T. Ikeda, A Rietveld-analysis program RIETAN-98 and its applications to zeolites, *Mater. Sci. Forum,* **2000**, 321-324, 198-205.

26. S. K. Kurtz and T. T. Perry, A powder technique for the evaluation of nonlinear optical materials, *J. Appl. Phys.,* **1968**, *39*, 3798-3813.

27. Y. Inaguma, A. Aimi, Y. Shirako, D. Sakurai, D. Mori, H. Kojitani, M. Akaogi and M. Nakayama, High-pressure synthesis, crystal structure, and phase stability relations of a $LiNbO_3$-type polar titanate $ZnTiO_3$ and its reinforced polarity by the second-order Jahn–Teller effect, *J. Am. Chem. Soc.,* **2014**, *136*, 2748-2756.

28. R. Liu, M. Tanaka, K.Yamaura and A. A.Belik, High-pressure synthesis, crystal structures, and magnetic and dielectric properties of $GdFeO_3$-type perovskites $(Dy_{0.5}Mn_{0.5})(Mn_{1-x}Ti_x)O_3$ with x = 0.5 and 0.75, *J. Alloys Compd.,* **2020**, *825*, 154019.

29. R. D. Shannon, Revised effective ionic radii and systematic studies of interatomic distances in halides and chalcogenides. *Acta Crystallogr., Sect. A: Cryst. Phys., Diffr., Theor. Gen. Crystallogr.,* **1976**, *32*, 751-767.

30. N. E. Brese and M. O'Keeffe, Bond-valence parameters for solids, *Acta Crystallogr., Sect. B: Struct. Sci.*, **1991**, *47*, 192-197.

31. C. Kittel, *Introduction to Solid State Physics*; 8th Ed., John Wiley and Sons, Inc: New York, **2005**.

32. A. M. Vibhakar, D. D. Khalyavin, P. Manuel, R. Liu, K. Yamaura, A. A. Belik and R. D. Johnson, Unusual effects of magnetic dilution in the ferrimagnetic columnar ordered $Sm_2MnMnMn_{4-x}Ti_xO_{12}$ perovskites, 2020, arXiv: 2009.10005 [cond-mat.].

33. R. Liu, R. Scatena, D. D. Khalyavin, R. D. Johnson, Y. Inaguma, M. Tanaka, Y. Matsushita, K. Yamaura and A. A. Belik, High-pressure synthesis, crystal structures, and properties of A-site columnar-ordered quadruple perovskites $NaRMn_2Ti_4O_{12}$ with R = Sm, Eu, Gd, Dy, Ho, Y, *Inorg. Chem.*, **2020**, *59*, 9065-9076.

34. G. Catalan and J. F. Scott, Physics and application of bismuth ferrite, *Adv. Mater.*, **2009**, *21*, 2463-2485.

35. F. Li, S. Zhang, T. Yang, Z. Xu, N. Zhang, G. Liu, J. Wang, J. Wang, Z. Cheng, Z.-G. Ye, J. Luo, T. R. Shrout and L.-Q. Chen, The origin of ultrahigh piezoelectricity in relaxor-ferroelectric solid solution crystals, *Nat. Commun*., **2016**, *7*, 13807.
36. Y. Kuroiwa, S. Kim, I. Fujii, S. Ueno, Y. Nakahira, C. Moriyoshi, Y. Sato and S. Wada, Piezoelectricity in perovskite-type pseudo-cubic ferroelectrics by partial ordering of off-centered cations, *Commun. Mater.*, **2020**, *1*, 71.
37. D. Y. Li, Y. J. Zeng, D. Batuk, L. M. C. Pereira, Z. Z. Ye, C. Fleischmann, M. Menghini, S. Nikitenko, J. Hadermann, K. Temst, A. Vantomme, M. J. Van Bael, J.-P. Locquet and C. Van Haesendonck, Relaxor ferroelectricity and magnetoelectric coupling in ZnO–Co nanocomposite thin films: beyond multiferroic composites, *ACS Appl. Mater. Interfaces*, **2014**, *6*, 4737-4742

Chapter 5. High-Pressure Synthesis, Crystal Structures, and Properties of $NaRMn_2Ti_4O_{12}$ with R = Sm, Eu, Gd, Dy, Ho, and Y

5.1 Introduction

ABO_3 perovskite materials containing titanium at the octahedral B site ($B = Ti^{4+}$) have crucial and widespread applications in modern technologies that originate from the exceptional dielectric, ferroelectric, and piezoelectric properties of such materials.[1–3] They constantly attract the attention of researchers working in the fields of fundamental and applied science.

$BaTiO_3$ and $PbTiO_3$ perovskites exhibit ferroelectric transitions at about 405 and 763 K, respectively. $BaTiO_3$ shows two additional phase transitions to other ferroelectric phases below 278 and 185 K.[2,4] Zr-doped $PbTiO_3$ perovskites are still the best piezoelectric materials for actuator and sensor applications in electronic devices.[2,3] $SrTiO_3$ is an archetypal incipient ferroelectric or a quantum paraelectric with changes in dielectric constant from about 370 at room temperature to about 18000 at 1.5 K.[5] This property has attracted great attention to $SrTiO_3$, and ferroelectricity in $SrTiO_3$ could be triggered by isotope substitutions and strain engineering.[6,7] $SrTiO_3$ has wide applications: for example, as a substrate for thin-film growths. $CaTiO_3$ crystallizes in the $GdFeO_3$-type Pnma structure at room temperature, and it shows no further symmetry changes on cooling and no ferroelectricity.[4] $CaTiO_3$ was also considered to be a quantum paraelectric. $CdTiO_3$, like $CaTiO_3$, crystallizes in the $GdFeO_3$-type *Pnma* structure at room temperature, but it undergoes a ferroelectric transition below about 85 K.[4,8]

Divalent cations at the A sites of $ATiO_3$ perovskites can be replaced for a 1:1 mixture of monovalent and trivalent cations. $Na_{0.5}R_{0.5}Ti_{O3}$ compounds with R = rare-earth cations crystallize in the $GdFeO_3$-type *Pnma* structure, show no ferroelectric transitions, and were suggested to have quantum paraelectric behaviors.[9,10] On the other hand, $Na_{0.5}Bi_{0.5}TiO_3$ shows complex phase transformations, the appearance of ferroelectric phases, complex and

hierarchical ferroelectric domains, and strong and anisotropic diffuse scattering.[11] $Na_{0.5}Bi_{0.5}TiO_3$ also forms morphotropic phase boundaries in different solid solutions and is considered a promising lead-free piezoelectric material to replace toxic lead in Zr-doped $PbTiO_3$ perovskites.[12]

A giant dielectric constant, which was temperature independent in wide temperature ranges, was discovered in the A-site-ordered quadruple perovskite $CaCu_3Ti_4O_{12}$ containing Ti^{4+} at the B site.[13,14] The origin of such an exceptional property has been the subject of considerable investigation, and different mechanisms have been suggested in the literature. Currently, the most accepted picture involves the electrical inhomogeneity of $CaCu_3Ti_4O_{12}$ ceramics, with semiconducting grains and insulating grain boundaries that create an internal barrier layer capacitor effect.[15,16] The idea of replacing Ca^{2+} in $CaCu_3Ti_4O_{12}$ for a mixture of $0.5Na^+$ and $0.5R^{3+}$ was also applied in the literature, and the resulting $(Na_{0.5}R_{0.5})Cu_3Ti_4O_{12}$ materials showed interesting dielectric properties. [17,18]

Recently, a new mechanism for ferroelectricity was suggested in a $CaMnTi_2O_6$ perovskite containing Ti^{4+} at the B site.[19,20] This compound has a ferroelectric transition at 630 K, a long-range antiferromagnetic transition at 10 K, and switchable polarization at room temperature. It crystallizes in another subfamily of the perovskite structure – in the so-called A-site columnar-ordered quadruple-perovskite structure with the generic chemical formula $A_2A'A''B_4O_{12}$.[21] Such perovskites have one column consisting of the AO_{10} polyhedra and one column consisting of alternating square-planar $A'O_4$ units and $A''O_4$ tetrahedra; the B sublattice is formed by corner-shared BO_6 octahedra as in all other (oxygen stoichiometric) perovskites. $CaMnTi_2O_6$ crystallizes in space group $P4_2/nmc$ (No. 137) above 630 K and space group $P4_2mc$ (No. 105) below 630 K.[19,20]

In this work, we investigated the effects of the replacement of $2Ca^{2+}$ cations in $CaMnTi_2O_6$ for a mixture of Na^+ and R^{3+} cations, where R^{3+} is a rare-earth cation. We could prepare $NaRMn_2Ti_4O_{12}$ with R = Sm, Eu, Gd, Dy, Ho, Y using a high-pressure, high-temperature

method. We found that they maintain the paraelectric structure of $CaMn_2Ti_4O_{12}$ between 1.5 and 300 K and crystallize in space group $P4_2/nmc$. Mn^{2+} cations remain highly disordered at the square-planar A′ site. They show a large dielectric constant of a possible extrinsic origin similar to the case for $CaCu_3Ti_4O_{12}$. Magnetic and specific heat measurements showed long-range magnetic ordering in all compounds below about 12 K, and the Ctype antiferromagnetic ordering of Mn^{2+} cations at the A′ and A″ sites was confirmed by neutron diffraction for R = Dy. However, certain magnetic rare-earth elements disturb the long-range ordering of Mn^{2+}, resulting in a second transition at lower temperatures.

5.2. Experimental details of Chapter 5

$NaRMn_2Ti_4O_{12}$ with R = La, Nd, Sm, Eu, Gd, Dy−Lu, Y were prepared from stoichiometric mixtures of MnO, "Na_2TiO_3", and commercial R_2O_3 (99.9−99.99%) and TiO_2 (99.99%) at 6 GPa and about 1750 K for 2 h (heating time to the synthesis temperature was 10 min) in Pt capsules using a belt-type high-pressure apparatus. After heat treatments, the samples were quenched to room temperature (RT), and the pressure was slowly released. The temperature of our high-pressure apparatus is controlled by the heating power with a calibrated relationship between power and temperature. All samples were dark brown hard pellets; the powder (after the pellets were ground) was brownish orange. All R_2O_3 chemicals were dried at 1273 K for several hours before use. Single-phase MnO was prepared from commercial MnO_2 (99.99%) by annealing at 1273 K in a 20% H_2 + 80% Ar flow for 2 h. "Na_2TiO_3" was prepared by annealing a stoichiometric mixture of TiO_2 and commercial Na_2CO_3 (99%) at 1073 K for 100 h in air with several intermediate grindings. "Na_2TiO_3" was a mixture of β - Na_2TiO_3 and $Na_8Ti_5O_{12}$ by X-ray diffraction.

X-ray powder diffraction (XRPD) data were collected at RT on a Rigaku MiniFlex600 diffractometer using Cu Kα radiation (a 2θ range of 8−100°, a step width of 0.02°, and a scan speed of 1°/min). High-temperature XRPD data of $NaSmMn_2Ti_4O_{12}$ were measured on a

Rigaku SmartLab instrument using Cu Kα1 radiation (45 kV, 200 mA; a 2θ range of 5−100°, a step width of 0.02°, and a scan speed of 1°/ min) from 300 to 770 K and from 770 to 300 K using a furnace attachment. Synchrotron XRPD data were measured at RT on a large Debye−Scherrer camera at the undulator beamline BL15XU of SPring-8.[22,23] The intensity data were collected between 2 and 60.23° at 0.003° intervals in 2θ; the incident beam was monochromated at λ = 0.65298 Å. The samples were packed into Lindemann glass capillaries (inner diameter 0.1 mm), which were rotated during measurements. Absorption coefficients were also measured. The Rietveld analysis was performed using the RIETAN-2000 program.[24] Mass fractions of phases (mass %) reported in this work were estimated by RIETAN-2000 from the refined scale factors after the Rietveld analysis of synchrotron XRPD data.

Neutron powder diffraction data of $NaDyMn_2Ti_4O_{12}$ were collected at the ISIS pulsed neutron and muon spallation source at the Rutherford Appleton Laboratory (U.K.), using the WISH diffractometer located at the second target station.[25] The sample (∼1.88 g: samples from four capsules were mixed) was loaded into a cylindrical 3 mm diameter vanadium can and measured at 1.5−20 K. Rietveld refinements of the crystal and magnetic structures were performed using the FullProf program[26] against the data measured in detector banks at average 2θ values of 58, 90, 122, and 154°, each covering 32° of the diffraction plane.

Powder second-harmonic-generation (SHG) measurements for $NaRMn_2Ti_4O_{12}$ with R = Sm, Gd were performed at room temperature on a modified Kurtz[27] nonlinear optical system using 1064 nm light in order to check the presence or absence of centrosymmetry. The experimental details are described in ref 28.

Magnetic measurements were performed on a SQUID magnetometer (Quantum Design, MPMS-XL-7T) between 2 and 400 K in different applied fields under both zero-field-cooled (ZFC) and field cooled on cooling (FCC) conditions. The inverse magnetic susceptibilities (χ^{-1}) were fit by the Curie−Weiss equation

$$\chi(T) = \mu_{\text{eff}}\, 2N \left(3k_{\text{B}}(T-\Theta)\right)^{-1} \quad (1)$$

where μ_{eff} is the effective magnetic moment, N is Avogadro's number, k_{B} is Boltzmann's constant, and Θ is the Curie−Weiss temperature. For the fitting, we used the FCC curves measured at 10 kOe and temperature intervals between 200 and 395 K. Isothermal magnetization measurements were performed between −70 and +70 kOe (at T = 1.8 and 5 K) and between −10 and +10 kOe (at T = 2 K). Frequency-dependent ac susceptibility measurements were performed on cooling with a Quantum Design MPMS-1T instrument at different frequencies (f) and different applied oscillating magnetic fields (H_{ac}). Specific heat, C_{p}, at magnetic fields of 0 and 90 kOe was recorded between 2 and 100 K on cooling by a pulse relaxation method using a commercial calorimeter (Quantum Design PPMS). Dielectric properties were measured on a Quantum Design PPMS using a NOVOCONTROL Alpha-A High-Performance Frequency Analyzer between 3 and 330 K on cooling and heating in the frequency range of 100 Hz and 2 MHz and at zero magnetic fields under usual-vacuum and high-vacuum conditions of the PPMS instrument. Under usual vacuum conditions, contributions from ice (most probably) to the dielectric constant were observed between about 220 and 270 K (depending on frequency). The extrinsic (ice) contribution disappeared under high-vacuum conditions; however, below about 50 K, the real sample temperature deviated significantly from the system temperature. Therefore, dielectric measurements under usual-vacuum and high-vacuum conditions were combined to obtain dielectric data in the whole temperature range.

Differential scanning calorimetry (DSC) curves were recorded on a Mettler Toledo DSC1 STARe system at a heating/cooling rate of 10 K/min under an N_2 flow between 290 and 723−873 K in open Al capsules and between 290 and 973 K in open Pt capsules. Several DSC runs were performed to check the reproducibility.

5.3. Results and discussion

5.3.1. Phase Compositions.

$NaRMn_2Ti_4O_{12}$ with R = Nd contained two perovskites phases: an A-site-ordered quadruple perovskite phase $(Nd_{0.8}Na_{0.2})Mn_3(Ti_{0.925}Mn_{0.075})_4O_{12}$ with space group *Im*–3 (about 75 mass %; *a* = 7.55000(2) Å) and a $GdFeO_3$-type *Pnma* perovskite phase $(Nd_{0.5}Na_{0.5})TiO_3$ (about 23 mass %; *a* = 5.43738(5) Å, *b* = 7.68966(6) Å, and *c* = 5.42755(5) Å) plus TiO_2 impurity (about 2 mass %). Note that the compositions of the A sites in both perovskite-related phases for R = Nd and the given lattice parameters were obtained by analysis of synchrotron XRPD data. A similar phase composition was found in the case of R = La. $NaRMn_2Ti_4O_{12}$ with R = Er–Lu contained a $GdFeO_3$-type *Pnma* perovskite phase, whose formula can be presented as $(Na_{0.25}R_{0.25}Mn_{0.5})TiO_3$, and a TiO_2 impurity (about 2–3 mass %). For example, the lattice parameters refined from synchrotron XRPD data at RT were *a* = 5.39602(2) Å, *b* = 7.54442(2) Å, and *c* = 5.23484(2) Å for R = Er and *a* = 5.39584(2) Å, *b* = 7.53471(2) Å, and *c* = 5.22424(2) Å for R = Yb (**Figure 5.1**).

$NaRMn_2Ti_4O_{12}$ with R = Sm, Eu, Gd, Dy, Ho, and Y mainly consisted of a new perovskite phase, whose reflections could be indexed in a tetragonal system. The subsequent structural analysis showed that they adopt the parent structure of the A-site columnar-ordered quadruple perovskite family with space group $P4_2/nmc$ (No. 137).[21,29] They all contained about 2–4 mass % of TiO_2 impurity; $NaRMn_2Ti_4O_{12}$ with R = Ho and Y also contained about 8 mass % of a $GdFeO_3$-type *Pnma* perovskite phase. The SHG response was not detected for $NaRMn_2Ti_4O_{12}$ with R = Sm and Gd at RT. Therefore, SHG measurements confirmed a centrosymmetric space group.

The above results show that for $NaRMn_2Ti_4O_{12}$, the A-site columnar-ordered quadruple perovskite structure is stabilized for the middle-size rare-earth elements of R = Sm–Ho and Y, with a transition region at R = Ho and Y to the $GdFeO_3$-type *Pnma* perovskite structure.

$NaTbMn_2Ti_4O_{12}$ should also crystallize in the same structure as the samples with R = Sm–Ho and Y, but we did not prepare it because a high-quality Tb_2O_3 chemical is not readily available. These results provide further evidence that the stability of A-site columnar-ordered quadruple perovskites in general strongly depends on the occupation of the A′, A″, and B sites, and that it is considerably limited.[21] For example, $R_2MnMn(Mn_2Sb_2)O_{12}$ is stable for R = La–Sm (at synthesis conditions used for all examples),[30] $R_2MnMnMn_4O_{12}$ is stable for R = Gd–Er and Y,[31] $R_2CuMnMn_4O_{12}$ is stable for R = Dy–Lu and Y,[32] and $R_2MnMn(MnTi_3)O_{12}$ is stable for R = Nd–Gd.[33]

Figure 5.1 . gives the compositional dependence of the lattice parameters in $NaRMn_2Ti_4O_{12}$. The lattice parameters change monotonically as a function of the ionic radii of the R^{3+} cations in a 10-fold coordination.[34] As the ionic radii in a 10-fold coordination are not available for the majority of R^{3+} cations we used the ionic radii in an 8-fold coordination plus 0.105 Å (the average difference between the ionic radii in 8- and 9-fold coordination is 0.055 Å, and the average difference between the ionic radii in 9- and 10-fold coordination is 0.05 Å).[34]

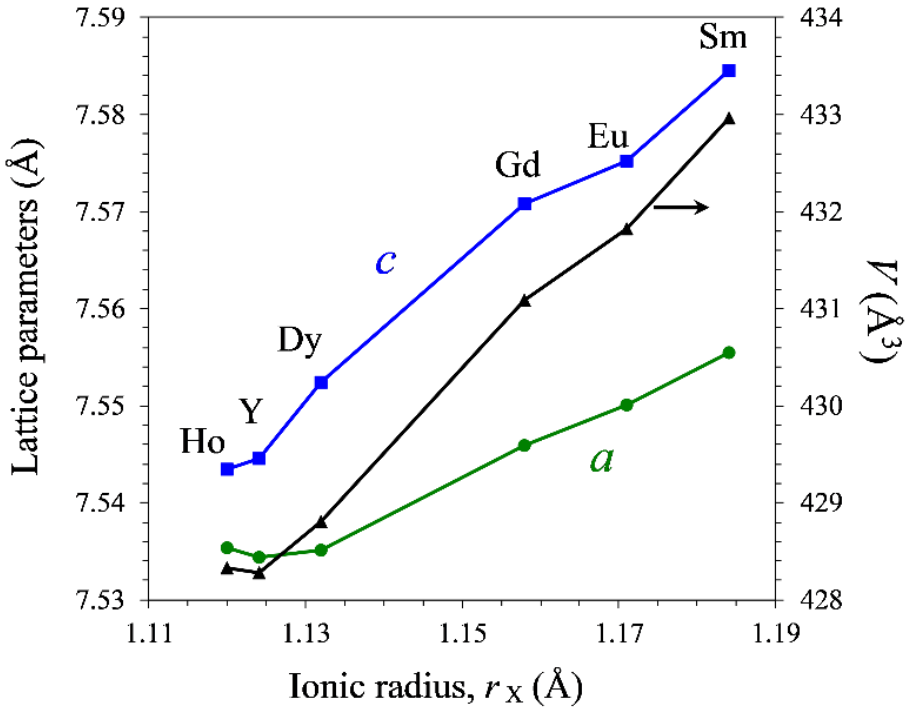

Figure 5.1. Compositional dependence of the room-temperature lattice parameters (*a* and *c*; space group $P4_2/nmc$) in $NaRMn_2Ti_4O_{12}$ as a function of the ionic radius of R^{3+} cations in the 10-fold coordination.

5.3.2. Crystal Structure.

In the following analysis of the $NaRMn_2Ti_4O_{12}$ (R = Sm, Eu, Gd, Dy, Ho, and Y) crystal structures we selected $NaDyMn_2Ti_4O_{12}$ as a representative to facilitate comparison with neutron diffraction studies. The initial structural model was taken from Ref. 33 for $Sm_2MnMn(Mn_{4-x}Ti_x)O_{12}$. It was confirmed that the A sites (in $A_2A'A''B_4O_{12}$) are statistically occupied by Na^+ and R^{3+} cations: the refined occupation factors were *g*(Dy) = 0.5033(9) and *g*(Na) = 0.4967. Therefore, the ideal 1:1 ratio of Na: R was fixed in the final refinements. The thermal parameter (*B*) of the square-planar Mn1 site (A′) in the ideal 2*a* (0.75, 0.25, 0.75) position was large for all the samples (*B*(Mn1) = 2.75(5) Å^2 for R = Dy), which indicated that the Mn1 site should be split. Indeed, moving Mn1 from the ideal 2*a* (0.75, 0.25, 0.75) position

with g(Mn1) = 1 (where g is the occupation factor) to the 4c (0.75, 0.25, z) position with g(Mn1) = 0.5 significantly reduced the B parameter for the Mn1 site and R values (from R_{wp} = 3.14 %, R_P = 2.10 %, R_I = 4.57 %, R_F = 4.71 % for the ideal Mn1 site to R_{wp} = 2.52 %, R_P = 1.84 %, R_I = 4.11 %, R_F = 4.07 % for the split Mn1 site). No evidence for further anti-site cation disorder could be found from the synchrotron X-ray diffraction data analysis, where deviations of the occupation factors from the ideal values were small and correlated with the thermal parameters (as usually observed in powder diffraction experiments). On the contrary, neutron diffraction measurements indicated about 6 % Dy/Mn occupational disorder between A and (A′, A′′) sites. We note that different synthetic batches of $NaDyMn_2Ti_4O_{12}$ were used for synchrotron and neutron diffraction experiments, and slightly different synthesis conditions (even though we used the same nominal synthesis conditions) could result in different cation distributions; the preparation of the neutron sample in a large volume could also affect the cation distribution.

Tables 5.1. and 5.2. give the refined structural parameters for all the samples. **Table 5.3.** summarizes the main bond lengths, bond-valence sum (BVS)[35] values, and Ti–O–Ti bond angles. Experimental, calculated, and difference synchrotron XRPD diffraction patterns of $NaDyMn_2Ti_4O_{12}$ are plotted in **Figure 5.2.**a. **Figure 5.3.** illustrates the crystal structure of $NaDyMn_2Ti_4O_{12}$.

The BVS values for the Na/R site (+1.88 to +2.06), calculated using the average R_0 values (= 0.5[$R_0(Na^+)$ + $R_0(R^{3+})$], that is, assuming the presence of a virtual $0.5Na^+/0.5R^{3+}$ atom), we're close to the expected value of +2 for all samples. We also calculated separate BVS values for R^{3+} and Na^+ cations. The BVS(Na^+) values were about +1.4 for samples with R = Sm, Eu, Gd, Dy, and Ho, and +1.5 for R = Y, suggesting that Na^+ cations are always over bonded. The common BVS(Na^+) values originate from similar Na/R–O bond lengths (approx. 2.55 Å) found in all samples. Such rigidity in the bonding of the Na/R cations originates from the structural features of the A-site columnar-ordered quadruple perovskites, where the octahedral tilts are primarily realized to establish square-planar coordination for the Mn1 site and tetrahedral

coordination for the Mn2 site. On the other hand, the BVS values for R^{3+} cations reduce from +3.03 (R = Sm) to +2.55 (R = Ho) suggesting that smaller rare-earth cations are underhanded. Such under bonding of R^{3+} and overbending of Na^{+} could determine the rare-earth stability range of these A-site columnar-ordered quadruple perovskites.

The Mn2–O2 bond lengths for the tetrahedral Mn2 site were within 2.096–2.133 Å in all samples as expected for Mn^{2+} cations, resulting in BVS values close to +2 (+1.83 to +2.01). The BVS values for the Ti site (+4.04 to +4.15) were close to the expected value of +4 for all samples, and the octahedral distortion parameter, $\Delta(TiO_6) = 1–4\times10^{-5}$ (the definition is given in the footnote of **Table 5.3.**), was very small suggesting a nearly regular TiO_6 octahedron in all the samples. Only the BVS values for the square-planar Mn1 site (+1.59 to +1.77) deviated noticeably from the expected value of +2. Interestingly, the BVS values were almost identical for the split Mn1 position and the ideal Mn1 position; this fact could suggest that Mn^{2+} cations can move in a certain region. The distance between the split and ideal positions was about 0.3 Å in all the samples; the similar shifts of Mn^{2+} cations from the center of the square-planar units (0.3–0.4 Å) were observed in the ferroelectric and paraelectric phases of $CaMnTi_2O_6$.[19,20] The ideal cation distribution in $NaRMn_2Ti_4O_{12}$ can be presented as $[Na^{+}R^{3+}]_A[Mn^{2+}]_{A'}[Mn^{2+}]_{A''}[Ti^{4+}{}_4]_BO_{12}$ to match with a generic chemical formula $A_2A'A''B_4O_{12}$ for such perovskites.[21]

So far, A-site columnar-ordered quadruple perovskites were only reported with Ca^{2+} and R^{3+} cations at the A site. Our results showed that such perovskites can also accommodate Na^{+} cations at the A site.

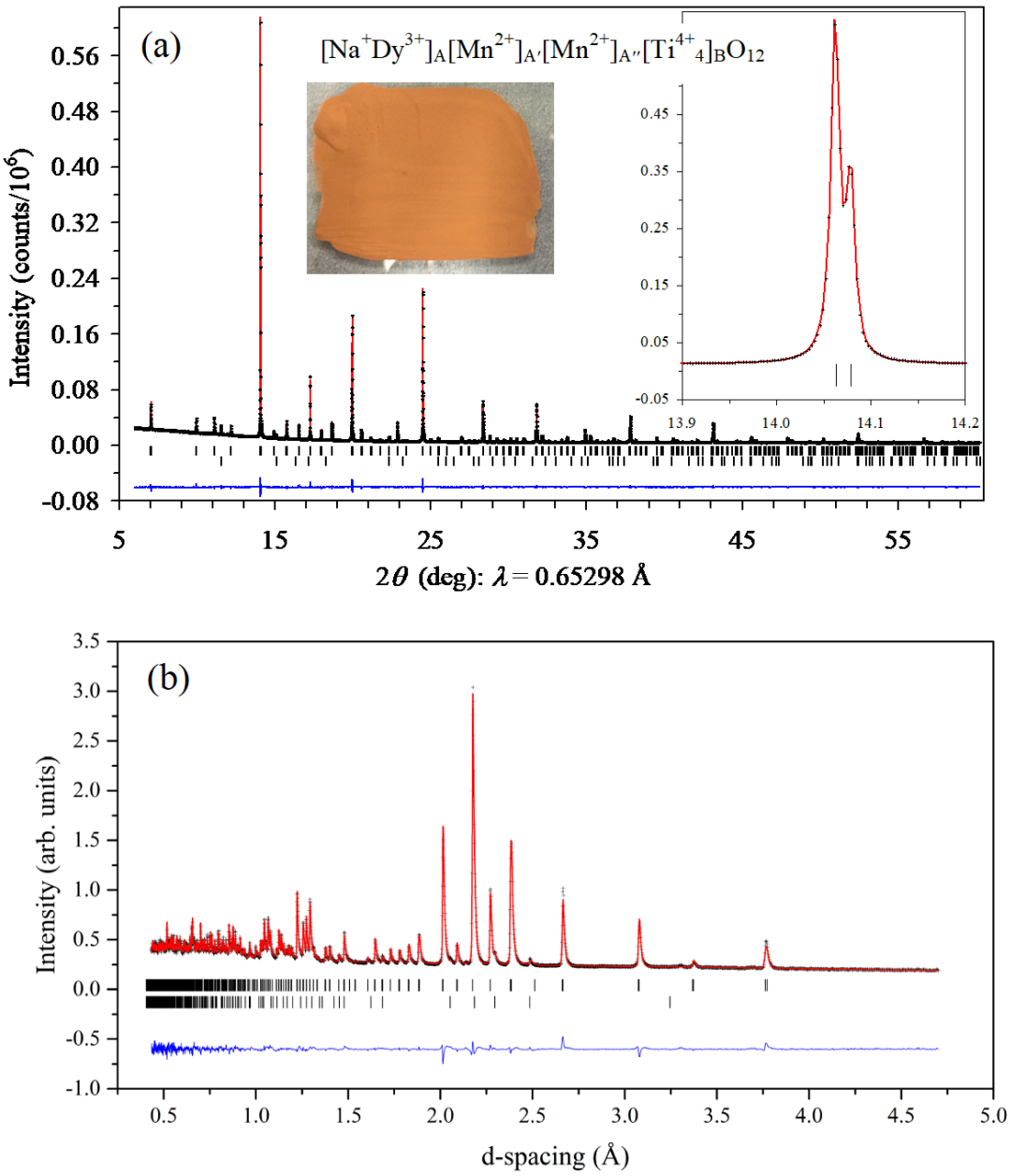

Figure 5.2. (a) Experimental (black crosses), calculated (red line), and difference (blue line) synchrotron X-ray powder diffraction patterns at T = 295 K and (b) neutron powder diffraction patterns at T = 20 K for $NaDyMn_2Ti_4O_{12}$. The tick marks show possible Bragg reflection positions for the main perovskite phase (the first row) and TiO_2 impurity (the second row). The right inset in panel (a) shows an enlarged fragment near the strongest reflections. The left inset in panel (a) shows the color of a powder $NaDyMn_2Ti_4O_{12}$ sample.

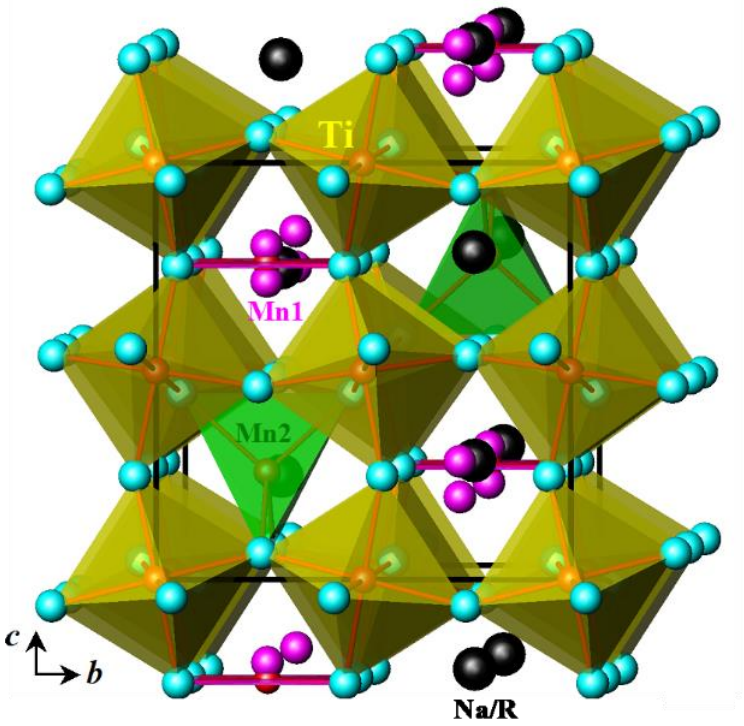

Figure 5.3. Crystal structure of $NaDyMn_2Ti_4O_{12}$. Ideal $Mn1O_4$ square-planar units, $Mn2O_4$ tetrahedra, and TiO_6 octahedra are shown. (Na/R) atoms are presented by large black spheres. The split Mn1 sites are also shown by pink spheres.

Table 5.1. Structure Parameters of $NaRMn_2Ti_4O_{12}$ with R = Sm, Eu, and Gd

R	Sm	Eu	Gd
Source		Synchrotron X-ray	
Wavelength (Å)		0.65298	
d-space range (Å)		0.6506-6.238	
Crystal system		Tetragonal	
Space group		$P4_2/nmc$ (No. 137, cell choice 2)	
Z		2	
Temperature (K)		295	
Formula Weight (g/mol)	666.725	668.329	673.615
a (Å)	7.55548(1)	7.55009(1)	7.54595(2)
c (Å)	7.58456(2)	7.57526(2)	7.57080(5)
V (Å^3)	432.9665(17)	431.8192(14)	431.092(3)

z(Na/R)	0.22628(7)	0.22516(6)	0.22460(9)
B(Na/R) (Å^2)	0.360(10)	0.402(9)	0.400(14)
z(Mn1$_{SQ}$)	0.7911(3)	0.7896(3)	0.7885(5)
B(Mn1$_{SQ}$) (Å^2)	0.92(6)	0.80(5)	0.85(8)
B(Mn2$_T$) (Å^2)	0.53(5)	0.53(4)	0.34(7)
B(Ti$_O$) (Å^2)	0.673(12)	0.657(10)	0.670(15)
y(O1)	0.0520(4)	0.0522(3)	0.0526(5)
z(O1)	–0.0376(4)	–0.0354(3)	–0.0356(5)
B(O1) (Å^2)	0.12(6)	0.03(5)	0.33(8)
y(O2)	0.5397(4)	0.5406(3)	0.5443(5)
z(O2)	0.5627(4)	0.5622(3)	0.5614(5)
B(O2) (Å^2)	0.31(6)	0.44(6)	0.35(8)
x(O3)	0.4523(3)	0.4514(2)	0.4524(4)
B(O3) (Å^2)	0.68(6)	0.83(6)	0.75(9)
R_{wp} (%)	2.82	2.19	2.39
R_p (%)	1.95	1.58	1.60
R_I (%)	4.19	5.94	4.22
R_F (%)	2.66	4.57	2.88
R_{exp} (%)	0.96	0.93	0.81
TiO_2 impurity (mass %)	3.6	2.0	1.9

Na/R – 4*d* site (0.25, 0.25, *z*); Mn1 – 4*c* site (0.75, 0.25, *z*) near 2*a* site (0.75, 0.25, 0.75); Mn2 – 2*b* site (0.75, 0.25, 0.25); Ti – 8*e* site (0, 0, 0); O1 and O2 – 8*g* site (0.25, *y*, *z*), and O3 – 8*f* site (*x*, –*x*, 0.25). *g*(Mn2) = *g*(Ti) = *g*(O1) = *g*(O2) = *g*(O3) = 1, were *g* is the occupation factor, and *g*(Mn1) = 0.5 and *g*(Na/R) = 0.5Na + 0.5R. SQ: square-planar, T: tetrahedral; O: octahedral.

Table 5.2. Structure Parameters of $NaRMn_2Ti_4O_{12}$ with R = Dy, Y, and Ho at T = 295 K from Synchrotron X-ray Powder Diffraction Data

R	Dy	Y	Ho
Formula Weight (g/mol)	678.865	605.233	681.257
a (Å)	7.53507(1)	7.53441(1)	7.53532(1)
c (Å)	7.55243(1)	7.54452(2)	7.54347(3)
V (Å^3)	428.8069(6)	428.2822(13)	428.3259(19)
z(Na/R)	0.22248(4)	0.22498(17)	0.22254(8)
B(Na/R) (Å^2)	0.464(6)	0.61(3)	0.616(12)
z(Mn1$_{SQ}$)	0.79279(17)	0.7916(4)	0.7903(4)
B(Mn1$_{SQ}$) (Å^2)	0.29(3)	0.49(7)	0.85(8)
B(Mn2$_T$) (Å^2)	0.45(3)	0.87(6)	0.65(7)
B(Ti$_O$) (Å^2)	0.595(8)	0.554(15)	0.460(15)

y(O1)	0.0539(3)	0.0593(6)	0.0528(5)
z(O1)	–0.0356(3)	–0.0370(5)	–0.0353(5)
B(O1) (Å^2)	0.31(4)	0.20(9)	0.31(8)
y(O2)	0.5436(2)	0.5408(5)	0.5474(5)
z(O2)	0.5619(2)	0.5596(5)	0.5596(5)
B(O2) (Å^2)	0.35(4)	0.55(8)	0.46(8)
x(O3)	0.45154(19)	0.4550(3)	0.4566(4)
B(O3) (Å^2)	0.78(4)	0.69(8)	1.22(10)
R_{wp} (%)	2.52	1.47	2.76
R_p (%)	1.84	1.08	1.87
R_I (%)	4.11	6.29	5.58
R_F (%)	4.04	6.97	4.21
R_{exp} (%)	1.11	0.70	0.97
TiO_2 impurity (mass %)	2.7	3.3	2.0
Pnma impurity (mass %)	-	8.3	8.3

Additional information is the same as in Table 1.

Table 5.3. Bond Lengths (in Å), Bond Angles (in Deg), Bond-Valence Sum (BVS), and Distortion Parameters of TiO_6 (Δ) in $NaRMn_2Ti_4O_{12}$ with R = Sm, Eu, Gd, Dy, Y, and Ho at T = 295 K

R	Sm	Eu	Gd	Dy	Y	Ho
Na/R–O1 (Å) ×2	2.334(3)	2.350(3)	2.348(4)	2.350(2)	2.300(4)	2.355(4)
Na/R–O1 (Å) ×2	2.498(3)	2.475(2)	2.470(4)	2.446(2)	2.443(3)	2.448(4)
Na/R–O2 (Å) ×2	2.516(3)	2.518(2)	2.541(3)	2.523(2)	2.521(4)	2.556(4)
Na/R–O3 (Å) ×4	2.725(1)	2.726(1)	2.723(1)	2.722(1)	2.713(1)	2.712(1)
BVS(R^{3+})	+3.03	+2.93	+2.83	+2.68	+2.66	+2.55
BVS(Na^+)	+1.39	+1.39	+1.38	+1.42	+1.49	+1.39
0.5[BVS(R^{3+})+ BVS(Na^+)]	+2.21	+2.16	+2.11	+2.05	+2.08	+1.97
BVS(Na/R)	+2.06	+2.02	+1.98	+1.95	+1.99	+1.88
Mn1–O3 (Å) ×4	2.184(3)	2.171(3)	2.179(4)	2.172(2)	2.206(4)	2.223(5)
Mn1–O2 (Å) ×2	2.602(3)	2.601(3)	2.585(5)	2.559(2)	2.567(5)	2.541(5)
Mn1–O1 (Å) ×2	2.950(3)	2.945(3)	2.952(4)	2.934(2)	2.979(5)	2.936(4)
Mn1–Mn1	0.624(4)	0.601(4)	0.582(7)	0.646(3)	0.620(5)	0.609(6)
BVS($Mn1^{2+}$)	+1.69	+1.74	+1.72	+1.77	+1.62	+1.59
BVS($Mn1i^{2+}$)	+1.69	+1.74	+1.72	+1.77	+1.63	+1.58

Mn2–O2 (Å) ×4	2.132(3)	2.126(3)	2.109(4)	2.107(2)	2.133(4)	2.096(4)
Mn2–O1 (Å) ×4	2.793(3)	2.802(2)	2.802(4)	2.805(2)	2.831(4)	2.798(4)
BVS($Mn2^{2+}$)	+1.85	+1.87	+1.95	+1.96	+1.83	+2.01
Ti–O1 (Å) ×2	1.950(1)	1.947(1)	1.947(1)	1.946(1)	1.956(1)	1.944(1)
Ti–O2 (Å) ×2	1.971(1)	1.970(1)	1.971(1)	1.969(1)	1.961(1)	1.969(1)
Ti–O3 (Å) ×2	1.963(1)	1.964(1)	1.960(1)	1.958(1)	1.946(1)	1.942(1)
Δ(Ti)	1.9×10^{-5}	2.4×10^{-5}	2.7×10^{-5}	2.2×10^{-5}	1.0×10^{-5}	4.2×10^{-5}
BVS(Ti^{4+})	+4.04	+4.06	+4.06	+4.09	+4.12	+4.15
Ti–O1–Ti ×2	151.17(8)	151.65(7)	151.46(8)	151.00(7)	148.75(8)	151.48(8)
Ti–O2–Ti ×2	146.86(8)	146.81(7)	146.25(8)	146.26(7)	147.74(8)	146.11(8)
Ti–O3–Ti ×2	149.92(8)	149.35(7)	149.95(8)	149.41(7)	151.48(8)	152.47(8)

BVS = $\sum_{i=1}^{N} v_i$, $v_i = \exp[(R_0 - l_i)/B]$, l_i is a bond length, N is the coordination number, $B = 0.37$, $R_0(Sm^{3+}) = 2.088$ Å, $R_0(Eu^{3+}) = 2.076$ Å, $R_0(Gd^{3+}) = 2.065$ Å, $R_0(Dy^{3+}) = 2.036$ Å, $R_0(Y^{3+}) = 2.014$ Å, $R_0(Ho^{3+}) = 2.023$ Å, $R_0(Na^{+}) = 1.80$ Å, $R_0(Mn^{2+}) = 1.79$ Å, $R_0(Ti^{4+}) = 1.815$ Å, R_0(Na/R) is the average value of $R_0(Na^{+})$ and $R_0(R^{3+})$.[35] $\Delta = (1/N)\sum_{i=1}^{N} [(l_i - l_{av})/l_{av}]^2$, where $l_{av} = (1/N)\sum_{i=1}^{N} l_i$ is the average distance. Mn1i is the ideal 2*a* site (0.75, 0.25, 0.75).

5.3.3. Thermal Properties of $NaRMn_2Ti_2Ti_4O_{12}$.

High-temperature studies were performed prior to the detailed structural investigations described above in order to rule out, or confirm, the existence of a ferroelectric transition as observed in CaMnTi2O6.[19,20] **Figure 5.4.** shows the temperature dependence of the lattice parameters and unit cell volume of $NaSmMn_2Ti_4O_{12}$ during heating and cooling. The volumetric coefficient of thermal expansion of $NaSmMn_2Ti_4O_{12}$ has a typical value on the order of 10^{-5} K^{-1} between 300 and 750 K (**Figure 5.4.**b).

On heating, the difference between the *a* and *c* parameters first decreases with increasing temperature up to about 600 K, but then it increases sharply above 650 K up to 770 K, where the DSC anomalies were observed. On cooling, the difference between the *a* and *c*

parameters became monotonic again. In the case of $CaMnTi_2O_6$, [19,20] the difference between the *a* and *c* parameters rapidly decreases on heating in the ferroelectric $P4_2mc$ phase, and the *a* and *c* parameters almost merged in the paraelectric $P4_2/nmc$ phase above 630 K. The high-temperature behavior of $NaRMn_2Ti_4O_{12}$ can probably be explained by annealing and relaxation effects of the metastable, stressed high-pressure phases, which were obtained by quenching. High-pressure and high-temperature synthesis conditions naturally introduce huge residual stresses in the as-prepared samples. Since the lattice is noncubic, the elastic moduli can be different for the in-plane and out-of-plane directions, making the stresses anisotropic. Hence, the annealing procedure that releases the stresses will result in an anisotropic change of the lattice parameters. This sample crystallizes in a different *Pnma* perovskite structure, confirming that the high-temperature DSC anomalies observed for the A-site columnar ordered quadruple perovskites are not caused by an intrinsic structural phase transition. After DSC experiments, all samples were checked by laboratory XRPD (at room temperature), and no noticeable changes in the phase compositions were found. We note that, as the $NaRMn_2Ti_4O_{12}$ compounds already adopt the parent A-site columnar-ordered quadruple-perovskite crystal structure at room temperature, higher temperature structural transitions are unlikely since any further symmetry increase will necessarily destroy the coordination environments for the Mn1 and Mn2 sites and hence likely lead to sample decomposition.

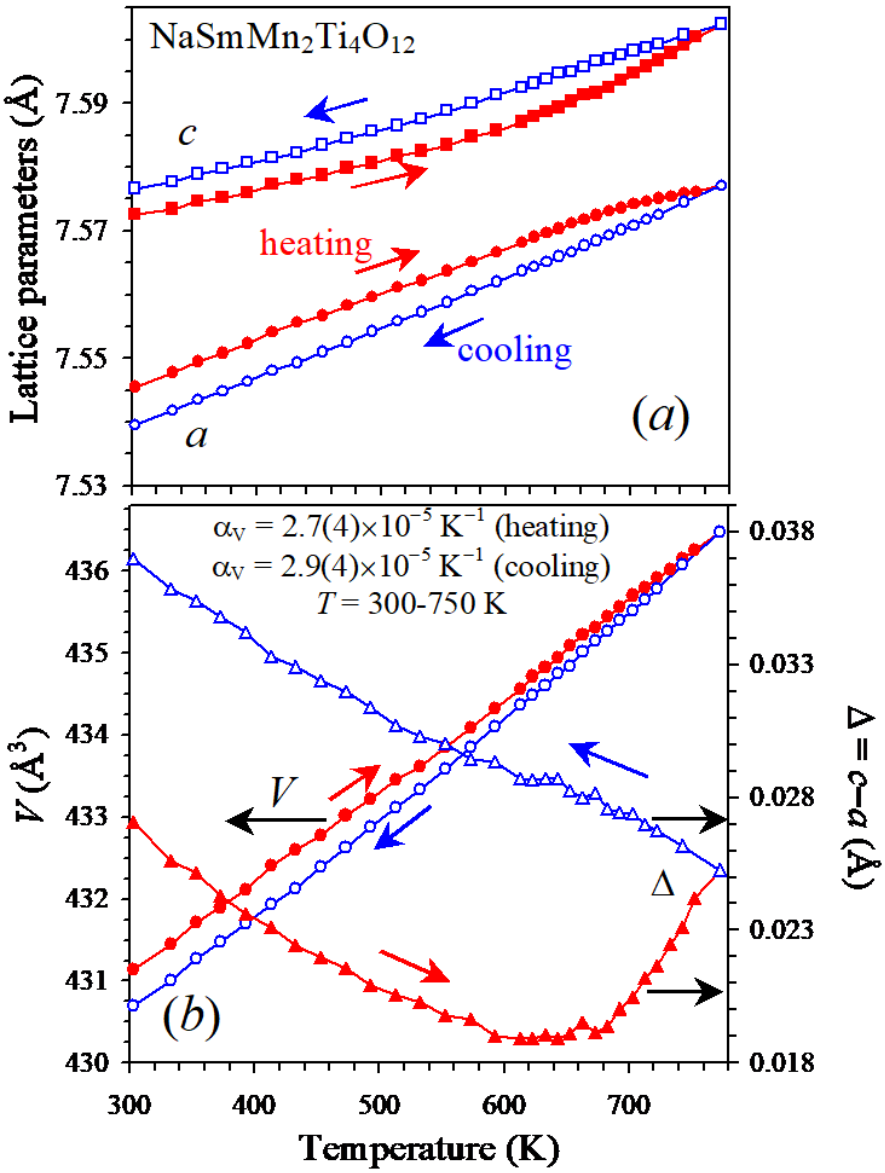

Figure 5.4. Temperature dependence of (a) the *a* and *c* lattice parameters and (b) unit-cell volume (the left-hand axis) and the difference between the *c* and *a* parameters (the right-hand axis) in $NaSmMn_2Ti_4O_{12}$ during heating and cooling. α_V is the volumetric coefficient of thermal expansion.

5.3.4. Magnetic Properties of $NaRMn_2Ti_2Ti_4O_{1.2}$.

Figures 5.5.–5.7. show magnetic susceptibility curves (χ versus T) of $NaRMn_2Ti_4O_{12}$. The samples containing R^{3+} cations with large moments (R = Gd, Dy, Ho) show no clear features on the χ versus T curves, which were dominated by paramagnetic-like contributions from R^{3+} cations. Weak anomalies at T_N could only be seen on the $d(\chi T)/dT$ versus T curves (insets of Figures **5.5**−**5.7**). The samples containing R^{3+} cations with small moments (R = Sm, Eu) and nonmagnetic R^{3+} cations (R = Y) showed small maxima at T_N. $NaSmMn_2Ti_4O_{12}$ exhibits two anomalies near T_{N1} = 10.5 K and T_{N2} = 5.0 K on the χ versus T curves at 100 Oe and 10 kOe. Two anomalies could also be seen on the 100 Oe $d(\chi T)/dT$ versus T curves of $NaEuMn_2Ti_4O_{12}$ near T_{N1} = 11.5 K and T_{N2} = 5.0 K.

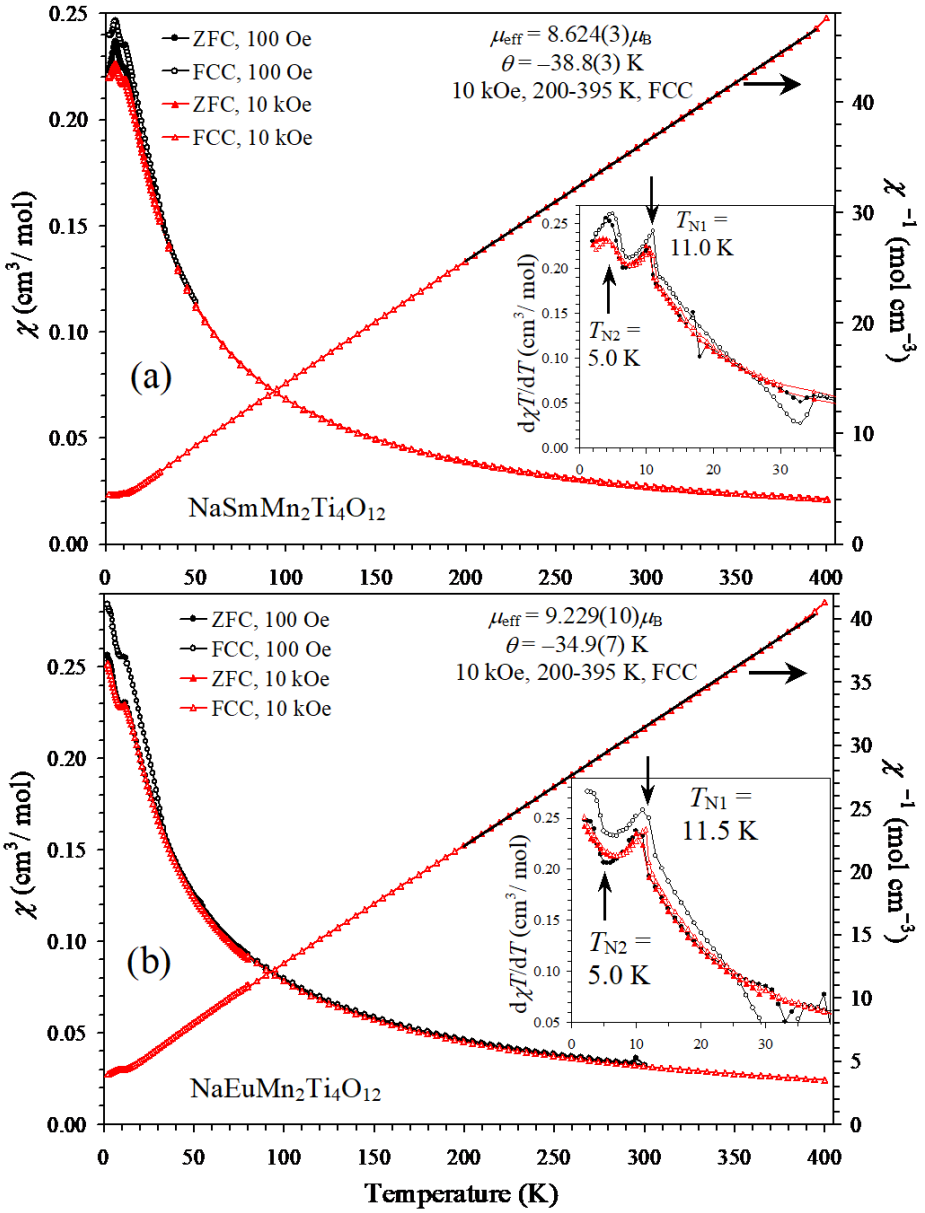

Figure 5.5. ZFC (filled symbols) and FCC (empty symbols) dc magnetic susceptibility ($\chi = M/H$) curves of (a) $NaSmMn_2Ti_4O_{12}$ and (b) $NaEuMn_2Ti_4O_{12}$ measured at 100 Oe and 10 kOe (left-hand axes). Right-hand axes give the FCC χ^{-1} versus T curves at 10 kOe with the Curie–Weiss fit and fitting parameters. Insets show the d(χT)/dT versus T curves below 40 K to emphasize magnetic anomalies.

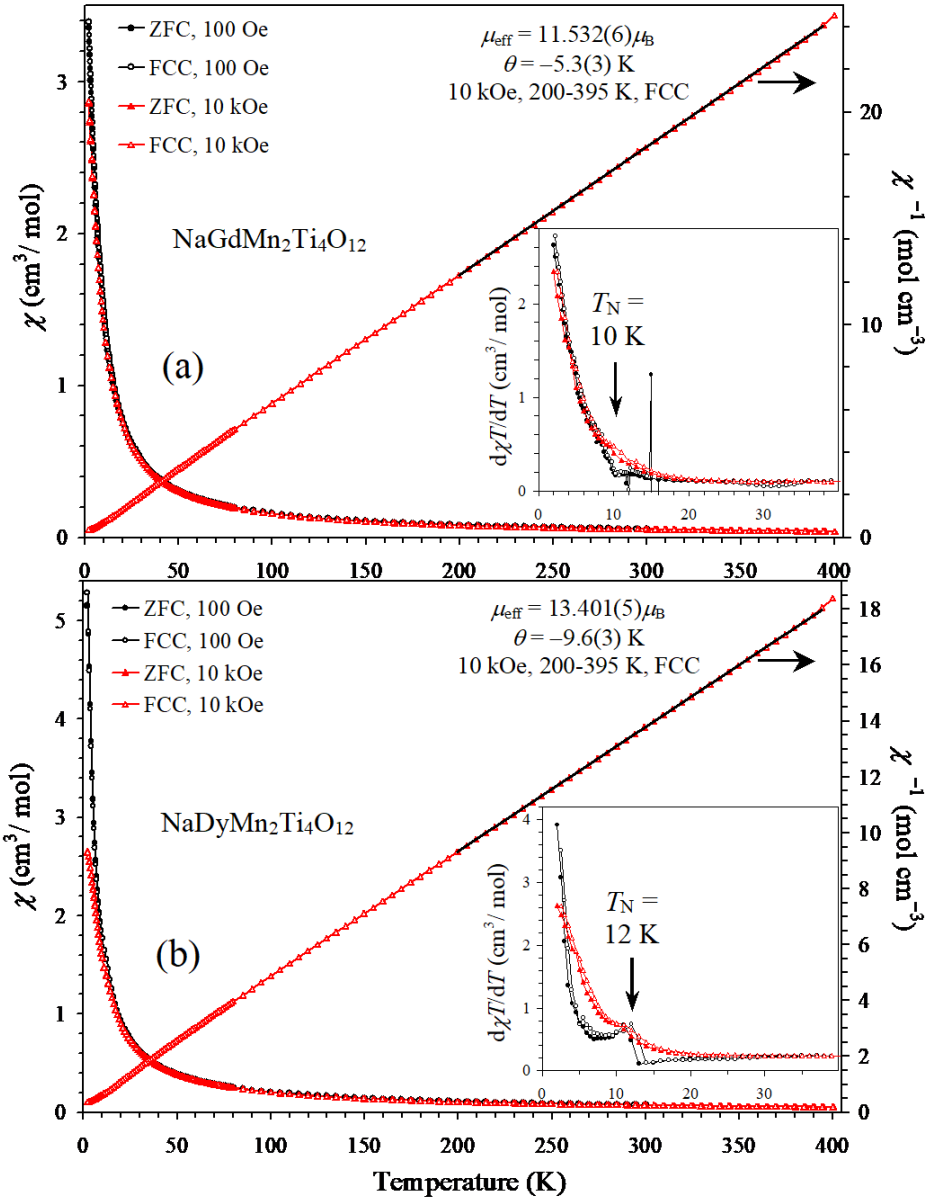

Figure 5.6. ZFC (filled symbols) and FCC (empty symbols) dc magnetic susceptibility ($\chi = M/H$) curves of (a) $NaGdMn_2Ti_4O_{12}$ and (b) $NaDyMn_2Ti_4O_{12}$ measured at 100 Oe and 10 kOe (left-hand axes). Right-hand axes give the FCC χ^{-1} versus T curves at 10 kOe with the Curie–Weiss fit and fitting parameters. Insets show the d(χT)/dT versus T curves below 40 K to emphasize magnetic anomalies.

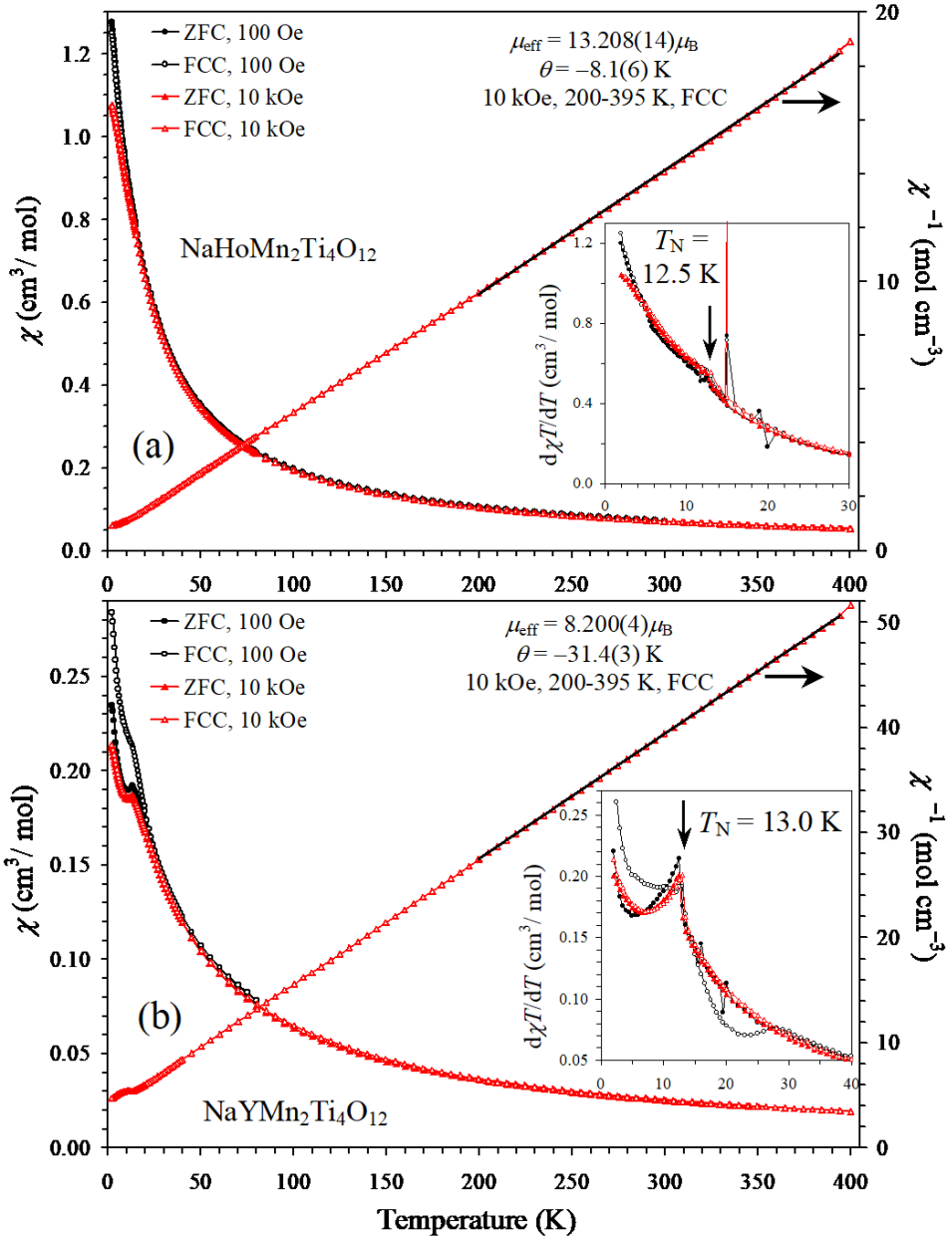

Figure 5.7. ZFC (filled symbols) and FCC (empty symbols) dc magnetic susceptibility ($\chi = M/H$) curves of (a) $NaHoMn_2Ti_4O_{12}$ and (b) $NaYMn_2Ti_4O_{12}$ measured at 100 Oe and 10 kOe (left-hand axes). Right-hand axes give the FCC χ^{-1} versus T curves at 10 kOe with the Curie–Weiss fit and fitting parameters. Insets show the d(χT)/dT versus T curves below 40 K to emphasize magnetic anomalies.

The fitting results with eq. (1) are summarized in **Table 5.4.** The Curie–Weiss linear behavior of the inverse susceptibilities was observed from 400 K down to almost T_N. The

experimental effective magnetic moments were close to the calculated ones in all the samples, and the negative Weiss temperatures confirm the dominated antiferromagnetic interactions.

Some samples showed a weak divergence between the 100 Oe ZFC and FCC curves and small anomalies on the 100 Oe d(χT)/dT versus T curves near 33 K (R = Sm and Eu), 36 K (R = Gd), and 28 K (R = Y). These temperatures are close to T_N of $MnCO_3$ (T_N = 34–35 K), and these additional magnetic anomalies could originate from this impurity, which shows canted antiferromagnetic properties,[37] even in an amount below the detection limit of synchrotron XRPD. Any contributions from the impurity disappear in high magnetic fields (10 kOe).

Table 5.4. Temperatures of Magnetic Anomalies and Parameters of the Curie–Weiss Fits and *M* versus *H* curves at *T* = 5 K for $NaRMn_2Ti_4O_{12}$

R	T_N (K)	μ_{eff} (μ_B/f.u.)	μ_{calc} (μ_B/f.u.)	θ (K)	M_S (μ_B/f.u.)
Sm	10.5, 5.0	8.624(3)	8.500	–38.8(3)	2.796
Eu	11.5, 5.0	9.229(10)	9.031	–34.9(7)	2.959
Gd	10.0	11.532(6)	11.576	–5.3(3)	10.559
Dy	12.0	13.401(5)	13.504	–9.6(3)	7.917
Ho	12.5	13.208(14)	13.348	–8.1(6)	7.355
Y	13.0	8.200(4)	8.367	–31.4(3)	2.497

The Curie–Weiss fits are performed between 200 and 395 K using the FCC χ^{-1} versus T data at 10 kOe. M_S is the magnetization value at T = 5 K and H = 70 kOe; the remnant magnetization (M_R) is nearly zero at T = 5 K, and the coercive field (H_C) is nearly zero T = 5 K. μ_{calc} is calculated using 1.5 μ_B for Sm^{3+}, 3.4 μ_B for Eu^{3+}, 8.0 μ_B for Gd^{3+}, 10.6 μ_B for Dy^{3+}, 10.4 μ_B for Ho^{3+}, and 5.916 μ_B for Mn^{2+}. T_N values were determined from peaks on the 100 Oe FCC d(χT)/dT versus T curves.

M versus H curves at T = 5 K was nearly linear without any hysteresis for $NaRMn_2Ti_4O_{12}$ with R = Sm, Eu, and Y (**Figure 5.8.** a) suggesting pure antiferromagnetic behavior. An S-type shape was observed for $NaRMn_2Ti_4O_{12}$ with R = Gd, Dy, and Ho (**Figure 8**b) from the strong

paramagnetic contributions of rare-earth cations, but no hysteresis was observed at T = 5 K. A tiny hysteresis opened at T = 1.8–2 K (**Figures 5.8.**) in samples that show a strong additional low-temperature specific heat anomaly (R = Sm and Dy).

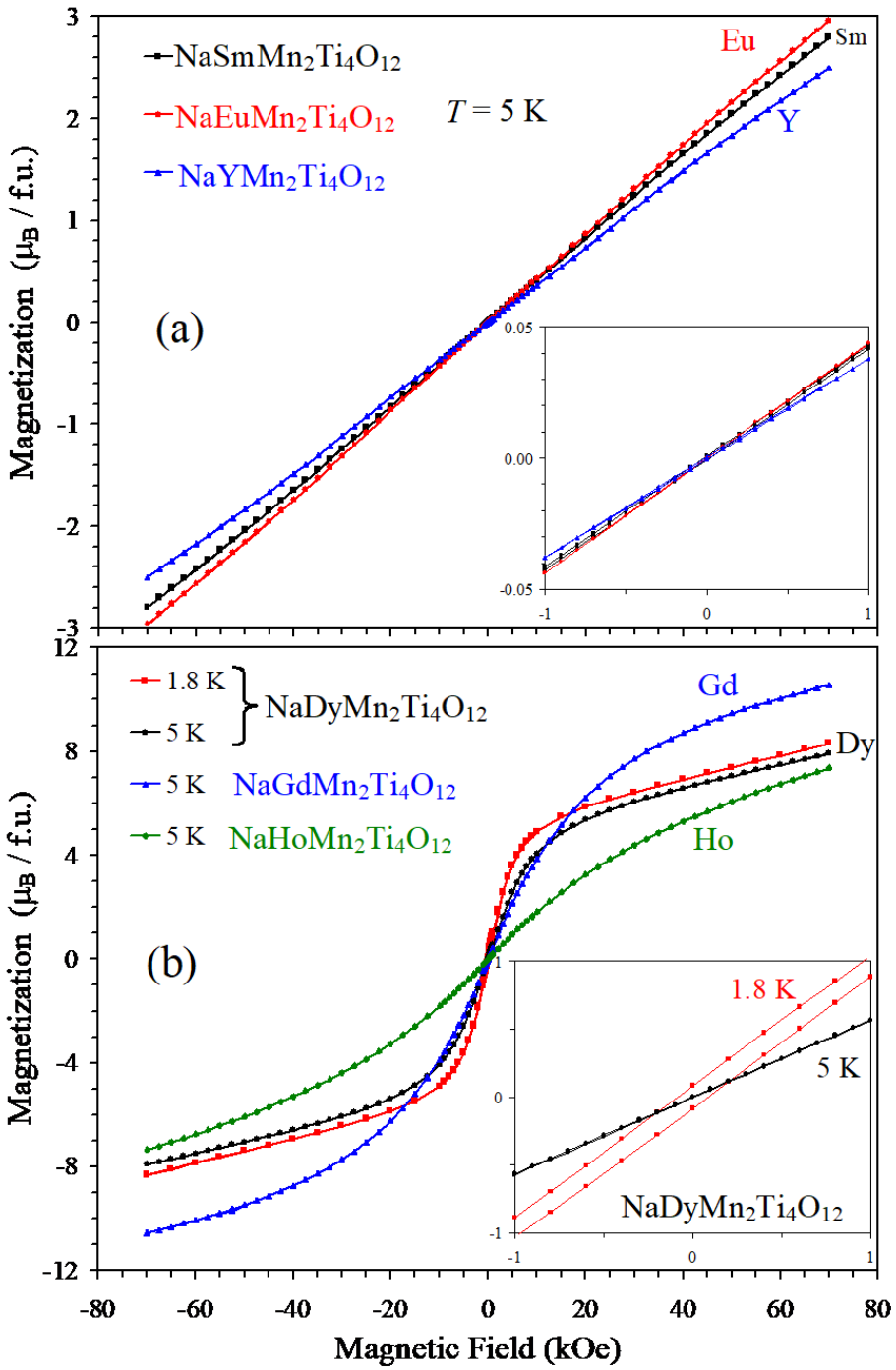

Figure 5.8. *M* versus *H* curves of $NaRMn_2Ti_4O_{12}$ (a) for R = Sm, Eu, and Y at *T* = 5 K and (b) for R = Dy at *T* = 1.8 and 5 K and for R = Gd and Ho at *T* = 5 K. Insets show details near the origin.

Specific heat measurements confirmed long-range magnetic orders at T_N in all of the samples (**Figures 5.9.** and **5.10.**). However, all of the samples showed additional magnetic anomalies at a lower temperature. Specific heat data (plotted as C_p/T versus *T*) of $NaRMn_2Ti_4O_{12}$ with R = Eu, Ho, Y were qualitatively similar to each other : (1) in addition to a sharp peak at T_N there was a hump near 8 K at *H* = 0 Oe and (2) a magnetic field of 90 kOe just slightly decreased T_N by about 1.5 K, keeping the hump. The C_p/T versus *T* values of $NaGdMn_2Ti_4O_{12}$ sharply increased down to 2 K at *H* = 0 Oe, and a magnetic field of 90 kOe suppressed this increase; a similar behavior of C_p/T versus *T* curves was observed in $GdMn_7O_{12}$.[38] C_p/T versus *T* curves of $NaRMn_2Ti_4O_{12}$ with R = Sm, Dy showed strong additional broad anomalies centered at 3.5 and 2.8 K, respectively, at *H* = 0 Oe. C_p/T versus *T* curves of $NaDyMn_2Ti_4O_{12}$ at *H* = 90 kOe were qualitatively similar to those of R = Eu, Ho, Y: that is, the broad anomaly near 2.8 K was suppressed. A magnetic field of 90 kOe had small effects in the case of $NaSmMn_2Ti_4O_{12}$.

The *mm*2 R site symmetry implies that the crystal electric field ground state of R ions with half-integer total angular momentum, *J* (e.g., Sm, Gd, and Dy), will be composed of a single Kramers doublet. If the degeneracy of the Kramers doublet is lifted by long-range magnetic ordering, a low-temperature Schottky anomaly might be expected to occur in the specific heat, as observed. In an applied high magnetic field the low-temperature Schottky anomaly will be suppressed, and powder averaging will instead result in the respective magnetic entropy being "spread out" over a wide temperature range.

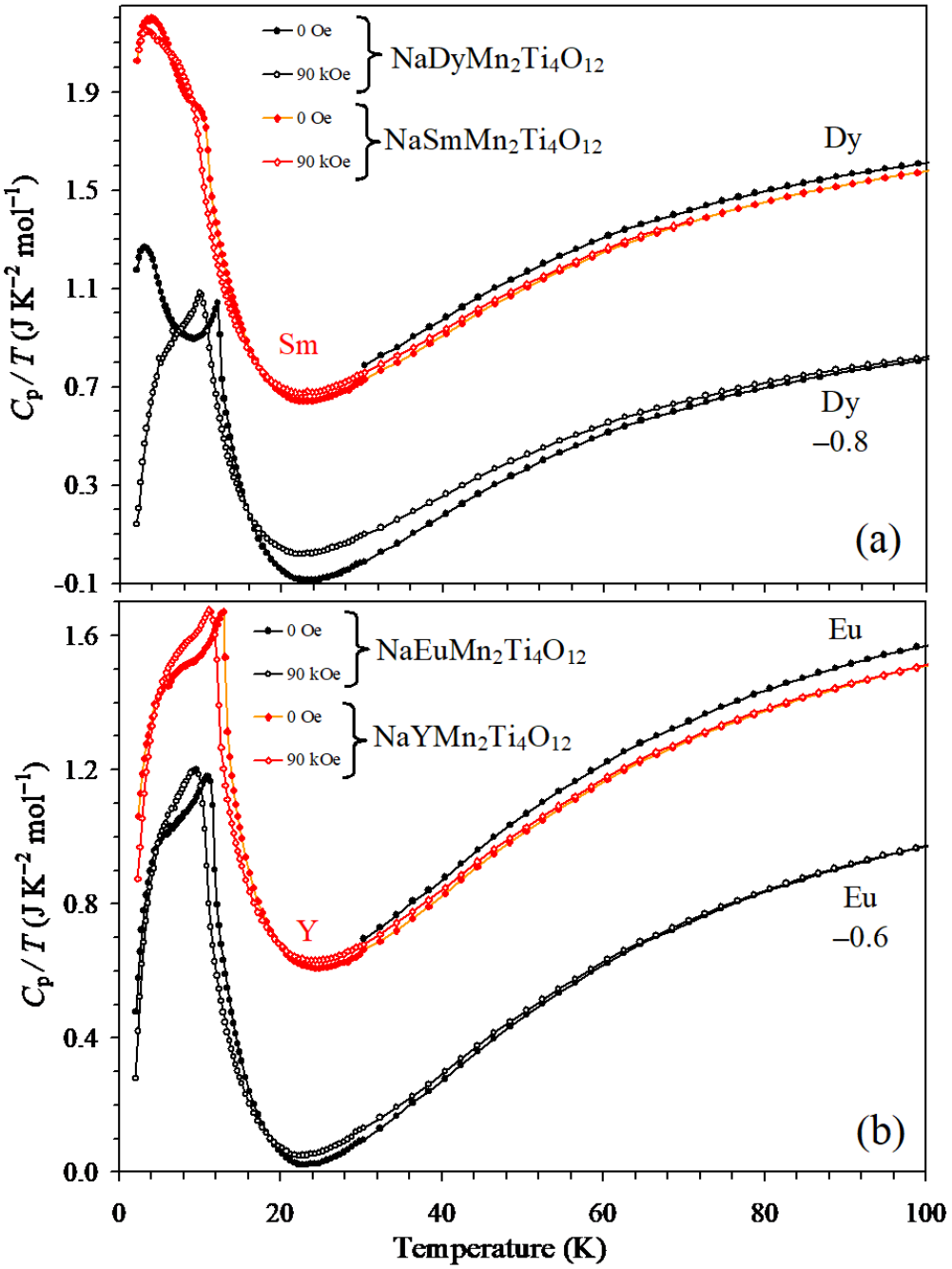

Figure 5.9. Specific heat data of $NaRMn_2Ti_4O_{12}$ plotted as C_p/T versus T with (a) R = Sm and Dy and (b) R = Eu and Y. Measurements were performed on cooling at H = 0 Oe (filled symbols) and 90 kOe (empty symbols). For R = Dy and Eu, the original data at H = 0 Oe between 30 and 100 K and shifted (for clarity) data are shown; the shift values are given in the figure.

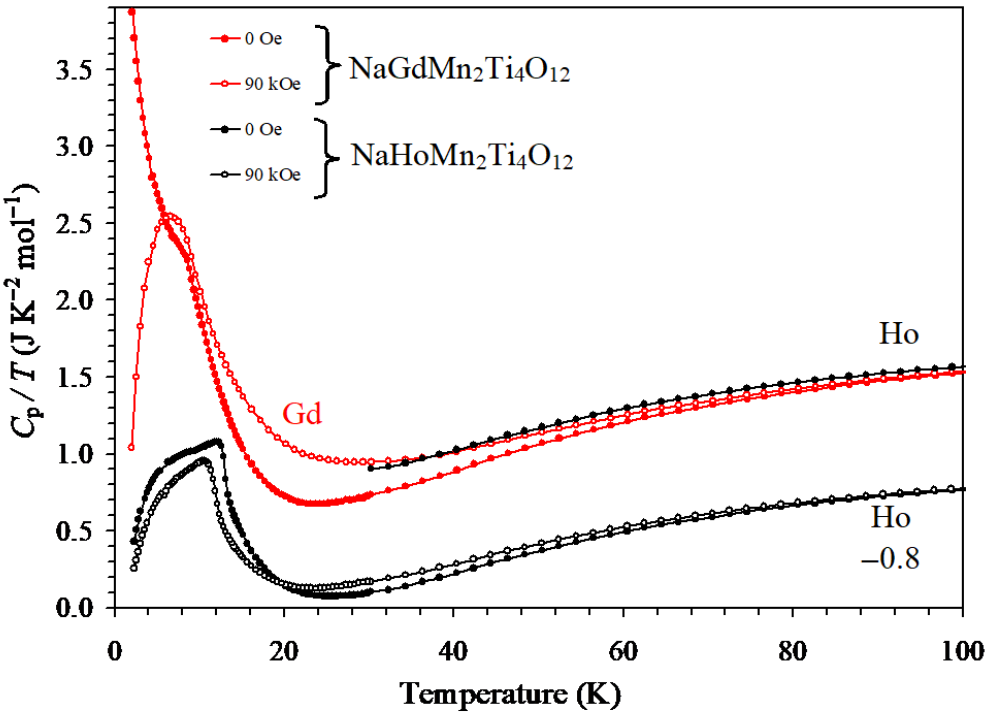

Figure 5.10. Specific heat data of $NaRMn_2Ti_4O_{12}$ plotted as C_p/T versus T with R = Gd and Ho. Measurements were performed on cooling at H = 0 Oe (filled symbols) and 90 kOe (empty symbols). For R = Ho, the original data at H = 0 Oe between 30 and 100 K and shifted (for clarity) data are shown; the shift value is given in the figure.

5.3.5. Neutron Deffractions of $NaRMn_2Ti_2Ti_4O_{1.2}$.

The R = Dy sample was selected for neutron diffraction studies for the following reasons: (1) it does not have a *Pnma* impurity, (2) it shows two possible magnetic transitions, and (3) among the R = Sm, Eu, Gd, Dy samples without a *Pnma* impurity, the R = Dy sample has the smallest neutron absorption coefficient. Measurements were performed at 20 K in the paramagnetic state just above T_{N1}, at 6 K between T_{N2} and T_{N1}, and at 1.5 K below T_{N2}, to gain insight into long-range magnetic ordering and the possible origin of the second magnetic transition, which was not observed in CaMnTi2O6. [19,20] The initial XRPD model was in good

agreement with the data; however, a significant improvement in the fitting was obtained by introducing about 6% Dy/Mn occupational disorder between A and (A′, A″) sites (R_{wp} = 4.18%, R_P = 4.49%, and R_F = 4.70% were improved to R_{wp} = 3.74%, R_P = 4.20%, and R_F = 4.14%). Such site disorder has been observed in other A-site columnar-ordered perovskites.[33] We note that an equivalent quality of the fitting could be achieved by introducing occupational disorder between Na and Mn; however, the amount of Na in the A′ and A″ sites was found to be larger (12.0%) in this case. The two scenarios with Dy/Mn or Na/Mn anti-site substitutions were considered separately, as parameter correlations prevent the simultaneous refinement of occupancies for all three cations. Neutron diffraction gave further evidence for the splitting of the Mn1 site, as the thermal parameter obtained for Mn when it was constrained to the ideal Mn1 site was unphysically large ($B \approx 7$ Å^2) and was also found to be independent of the anti-site cation disorder. A TiO_2 impurity phase was also present in a small amount, 3.3(2) mass %, in the measured sample.

Below the magnetic phase transition temperature, new diffraction peaks were observed in the diffraction pattern. These peaks could be fit using the same profile parameters as used for the paramagnetic refinement, indicating that the magnetic order is well correlated in all three dimensions. The three strongest magnetic diffraction peaks (see **Figure 5.11.** inset) could be indexed {102}, {212}, and {100} with respect to the paramagnetic crystal structure. Symmetry analysis using ISODISTORT[39] gave four irreducible representations for the Mn lattice in which Mn1 was considered sitting in its ideal non-split position. We consider four symmetry-adapted modes, F_i, A_i, C_i, and G_i, where the subscript i denotes the direction of the magnetic moments. Broadly speaking, these modes describe magnetic structures with either ferromagnetic (FM) or antiferromagnetic (AFM) nearest-neighbor interactions and moments parallel or perpendicular to the tetragonal *c*-axis. The measured magnetic intensities are at *hkl* positions that satisfy the diffraction condition $l = 2n$ and $h+k = 2n+1$, where n is an integer. These diffraction conditions

uniquely determine a C-type magnetic structure of the Mn lattice, according to which AFM coupled layers in the *ab*-plane are FM coupled along the *c*-crystallographic direction. Furthermore, the observation of the magnetic diffraction peak {100}, together with the absence of the (001) peak, uniquely determines the moment direction be parallel to the tetragonal *c*-axis (i.e. Γ_2^- with $P4_2'/n'm'c$, No. 137.512 magnetic space group). This magnetic structure was refined against the data, an excellent agreement factor R_{mag} = 3.34 % was achieved, and a Mn magnetic moment of 2.58(2) μ_B at 6 K was found, which is noticeably reduced compared with the expected moment of 5μ_B for Mn^{2+}. The same magnetic structure and similar magnetic moment of 2.58 μ_B were found in $Ca_{1.4}Mn_{0.6}Ti_2O_6$ in the ground state at 1.5 K.[20] We note that the symmetry of the system (Γ_2^-) allows the moments at the A′ and A″ sites to be refined independently, however, this admixes an A_z mode that would produce magnetic peaks in the position of the diffractogram where nothing was detected. Surprisingly, the magnetic Bragg peaks broaden at 1.5 K below the second magnetic transition, revealing a transition to a state with short-range magnetic correlations (**Figure 5.11.**a inset). The origin of this transition is not clear and will be the subject of future studies, but it could be related to the polarization of Dy magnetic moments together with some Na/Dy occupational disorder in the A sites.

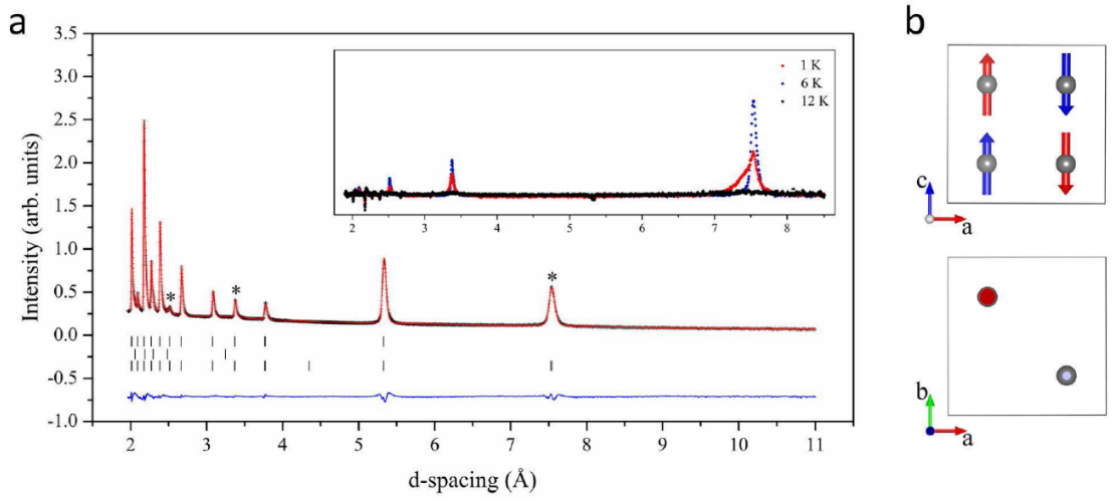

Figure 5.11. (a) Neutron powder diffraction pattern at T = 6 K for $NaDyMn_2Ti_4O_{12}$. Data

and fit are shown as black crosses and a red line, respectively, and their difference is drawn as a blue line at the bottom of the panel (reliability factors: R_p = 3.41 %, R_{wp} = 3.03 %, R_{Bragg} = 3.56 % (nuclear) and R_{Bragg} = 3.34 % (magnetic)). The tick marks show possible Bragg reflection positions for the main perovskite phase (first row); TiO_2 impurity (second row); and C-type magnetic structure of the manganese A′ and A″ the lattice of the main perovskite phase (third row). Peaks with magnetic intensity contributions are marked by an asterisk and their temperature evolutions are shown in the inset. (b) View of the C-type magnetic structure along with different crystallographic directions. Mn atoms in the square planar and the tetrahedral coordination sites are shown with blue and red arrows, respectively.

5.3.6. Dielectric Properties of $NaRMn_2Ti_2Ti_4O_{1.2}$.

Dielectric measurements showed the existence of two plateaus: a low-temperature plateau with a dielectric constant of about 100 and a high-temperature plateau with a dielectric constant of about 600. The dielectric constant changed in a steplike manner between the two plateaus, and the temperature of the steplike change strongly depended on frequency. At the same time, very strong dielectric loss peaks appeared at the temperature of the steplike dielectric change. The low-temperature plateau was quite narrow in the case of $NaGdMn_2Ti_4O_{12}$ (**Figure 5.12.**), while it was wider in the cases of $NaDyMn_2Ti_4O_{12}$ (**Figure 5.13.**). The temperature dependence of the dielectric constant of $NaRMn_2Ti_4O_{12}$ resembles that of $CaCu_3Ti_4O_{12}$ except for one difference; the high-temperature plateau does not reach giant values as in $CaCu_3Ti_4O_{12}$. [13–15] Therefore, we can assume that changes in the dielectric constant occur via the same mechanism in $NaRMn_2Ti_4O_{12}$ and Ca $Cu_3Ti_4O_{12}$: that is, there is an electrical inhomogeneity of $NaRMn_2Ti_4O_{12}$ ceramics with semiconducting grains and insulating grain boundaries (or vice versa). However, we emphasize that $NaRMn_2Ti_4O_{12}$ ceramics were highly insulating even at room temperature, and the total resistivity of $NaRMn_2Ti_4O_{12}$ceramics could

not be measured with a PPMS system.

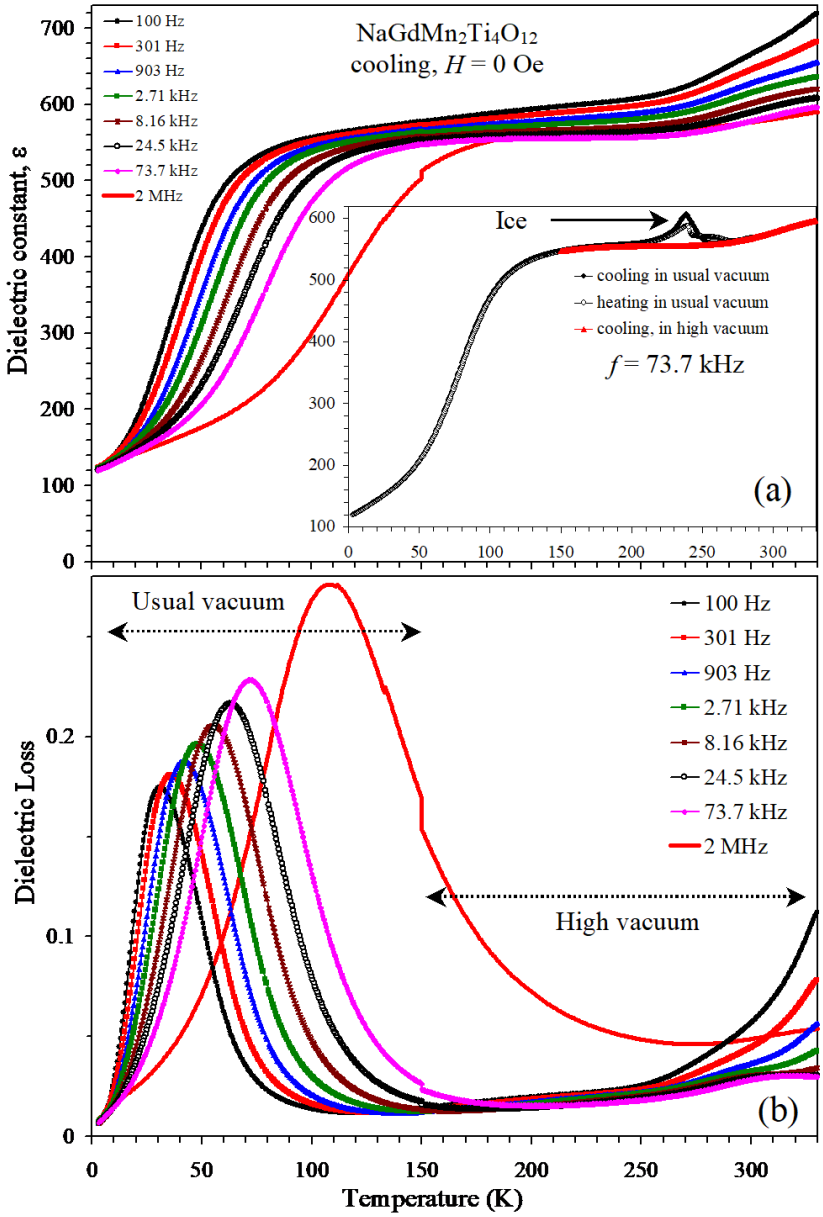

Figure 5.12. (a) Dielectric constant and (b) dielectric loss of $NaGdMn_2Ti_4O_{12}$ as a function of temperature measured at H = 0 Oe on heating at different frequencies. Measurements in usual and high vacuum conditions were combined at 150 K. The inset gives dielectric constant in usual (3–330 K) and high vacuum (150–330 K) conditions to emphasize extrinsic contributions near 220–270 K in usual vacuum conditions.

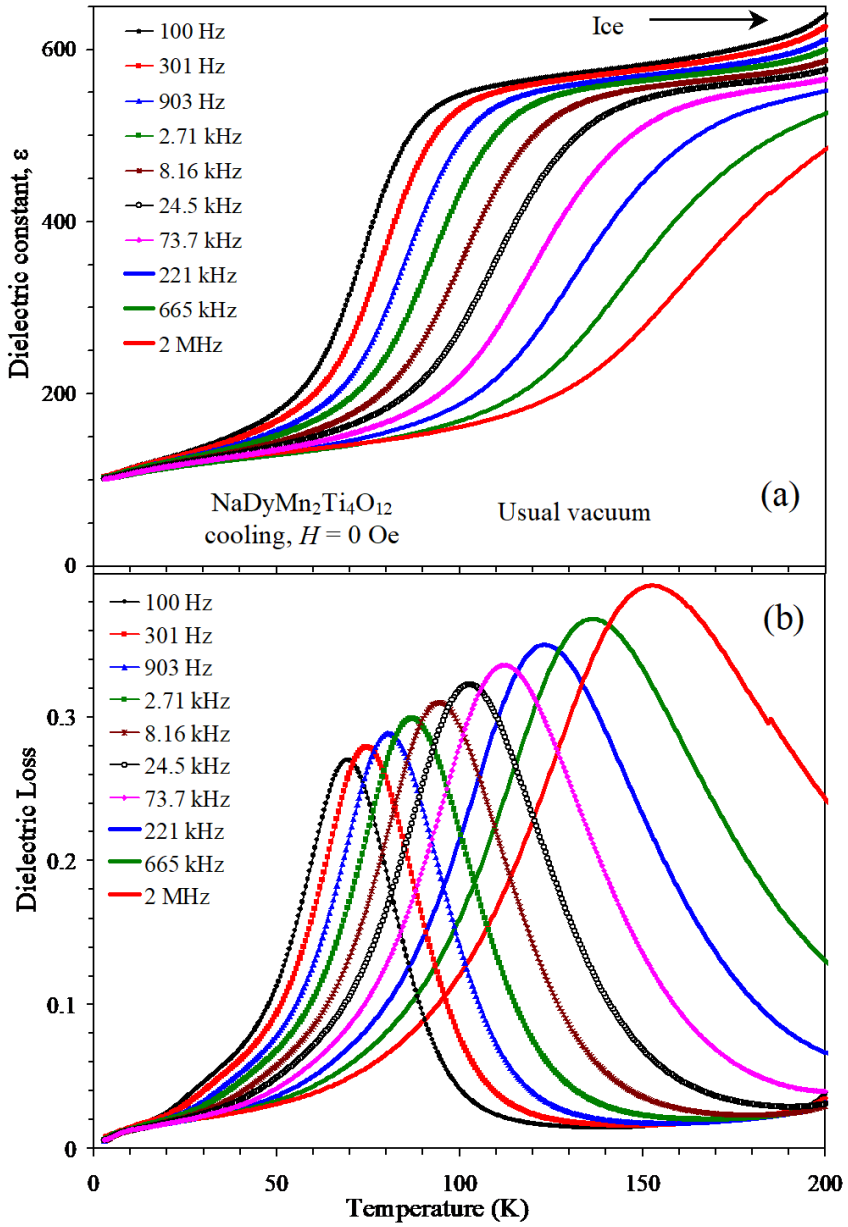

Figure 5.13. (a) Dielectric constant and (b) dielectric loss of $NaDyMn_2Ti_4O_{12}$ as a function of temperature measured at H = 0 Oe on cooling at different frequencies. Measurements were performed in usual vacuum conditions, the data are shown below 200 K, where extrinsic contributions are absent.

5.4. Summary of Chapter 5

A-site columnar-ordered quadruple perovskites $NaRMn_2Ti_4O_{12}$ with R = Sm, Eu, Gd, Dy, Ho, Y were prepared by a high-pressure, high-temperature method. Structural studies between 1.5 and 300 K based on an analysis of powder synchrotron X-ray and neutron diffraction data indicated that they maintained the centrosymmetric paraelectric structure at all temperatures, with Mn^{2+} cations high disordered at the square-planar site. We have shown a C-type magnetic structure for R = Dy at 6 K, similar to that found in the $CaMnTi_2O_6$ compound. Given similarities in the magnetic susceptibility and heat capacity data, we anticipate the same magnetic structure in all A-site columnar-ordered $NaRMn_2Ti_4O_{12}$ compounds, at least below T_{N1} = 8−13 K. However, additional magnetic features were observed at lower temperatures for R = Sm, Eu, Dy.

References in Chapter 5

1. Dawber, M.; Rabe, K.; Scott, J., Physics of thin-film ferroelectric oxides. *Rev. Mod. Phys.* **2005,** *77* (4), 1083.
2. Izyumskaya, N.; Alivov, Y.; Morkoc, H., Oxides, oxides, and more oxides: high-κ oxides, ferroelectrics, ferromagnetics, and multiferroics. *Crit. Rev. Solid State Mater. Sci.* **2009,** *34* (3-4), 89-179.
3. Izyumskaya, N.; Alivov, Y.-I.; Cho, S.-J.; Morkoç, H.; Lee, H.; Kang, Y.-S., Processing, structure, properties, and applications of PZT thin films. *Crit. Rev. Solid State Mater. Sci.* **2007,** *32* (3-4), 111-202.
4. Kennedy, B. J.; Zhou, Q.; Zhao, S.; Jia, F.; Ren, W.; Knight, K. S., Low-temperature structure and the ferroelectric phase transitions in the $CdTiO_3$ perovskite. *Phys. Rev. B* **2017,** *96* (21), 214105.
5. Müller, K. A.; Burkard, H., $SrTiO_3$: An intrinsic quantum paraelectric below 4 K. *Phys. Rev. B* **1979,** *19* (7), 3593.
6. Itoh, M.; Wang, R.; Inaguma, Y.; Yamaguchi, T.; Shan, Y.; Nakamura, T., Ferroelectricity induced by oxygen isotope exchange in strontium titanate perovskite. *Phys. Rev. Lett.* **1999,** *82* (17), 3540.
7. Jang, H.; Kumar, A.; Denev, S.; Biegalski, M. D.; Maksymovych, P.; Bark, C.; Nelson, C. T.; Folkman, C.; Baek, S. H.; Balke, N., Ferroelectricity in strain-free $SrTiO_3$ thin films. *Phys. Rev. Lett.* **2010,** *104* (19), 197601.
8. Taniguchi, H.; Shan, Y. J.; Mori, H.; Itoh, M., Critical soft-mode dynamics and unusual anticrossing in $CdTiO_3$ studied by Raman scattering. *Phys. Rev. B* **2007,** *76* (21), 212103.
9. Inaguma, Y.; Sohn, J.-H.; Kim, I.-S.; Itoh, M., Quantum Paraelectricity in a Perovskite $La_{1/2}Na_{1/2}TiO_3$. *J. Phys. Soc. Jpn.* **1992,** *61* (10), 3831-3832.

10. Shan, Y. J.; Nakamura, T.; Inaguma, Y.; Itoh, M., Preparation and dielectric characterizations of the novel perovskite-type oxides ($Ln_{1/2}Na_{1/2}$)TiO_3 (Ln= Dy, Ho, Er, Tm, Yb, Lu). *Solid State Ionics* **1998,** *108* (1-4), 123-128.
11. Gorfman, S.; Glazer, A.; Noguchi, Y.; Miyayama, M.; Luo, H.; Thomas, P., Observation of a low-symmetry phase in $Na_{0.5}Bi_{0.5}TiO_3$ crystals by optical birefringence microscopy. *J. Appl. Crystallogr.* **2012,** *45* (3), 444-452.
12. McQuade, R. R.; Dolgos, M. R., A review of the structure-property relationships in lead-free piezoelectric (1−*x*)$Na_{0.5}Bi_{0.5}TiO_3$(*x*)$BaTiO_3$. *J. Solid State Chem.* **2016,** *242*, 140-147.
13. Subramanian, M.; Li, D.; Duan, N.; Reisner, B.; Sleight, A., High dielectric constant in $ACu_3Ti_4O_{12}$ and $ACu_3Ti_3FeO_{12}$ phases. *J. Solid State Chem.* **2000,** *151* (2), 323-325.
14. Homes, C.; Vogt, T.; Shapiro, S.; Wakimoto, S.; Ramirez, A., Optical response of high-dielectric-constant perovskite-related oxide. *Science* **2001,** *293* (5530), 673-676.
15. Liu, L.; Ren, S.; Liu, J.; Han, F.; Zhang, J.; Peng, B.; Wang, D.; Bokov, A. A.; Ye, Z.-G., Localized polarons and conductive charge carriers: Understanding $CaCu_3Ti_4O_{12}$ over a broad temperature range. *Phys. Rev. B* **2019,** *99* (9), 094110.
16. Adams, T. B.; Sinclair, D. C.; West, A. R., Giant barrier layer capacitance effects in $CaCu_3Ti_4O_{12}$ ceramics. *Adv. Mater.* **2002,** *14* (18), 1321-1323.
17. Ferrarelli, M. C.; Adams, T. B.; Feteira, A.; Sinclair, D. C.; West, A. R., High intrinsic permittivity in $Na_{1/2}Bi_{1/2}Cu_3Ti_4O_{12}$. *Appl. Phys. Lett.* **2006,** *89* (21), 212904.
18. Ferrarelli, M. C.; Sinclair, D. C.; West, A. R., Possible incipient ferroelectricity in Mn-doped $Na_{1/2}Bi_{1/2}Cu_3Ti_4O_{12}$. *Appl. Phys. Lett.* **2009,** *94* (21), 212901.
19. Aimi, A.; Mori, D.; Hiraki, K.-i.; Takahashi, T.; Shan, Y. J.; Shirako, Y.; Zhou, J.; Inaguma, Y., High-Pressure Synthesis of A-Site Ordered Double Perovskite $CaMnTi_2O_6$ and Ferroelectricity Driven by Coupling of A-Site Ordering and the Second-Order Jahn–Teller Effect. *Chem. Mater.* **2014,** *26* (8), 2601-2608.

20. Li, Z.; Cho, Y.; Li, X.; Li, X.; Aimi, A.; Inaguma, Y.; Alonso, J. A.; Fernandez-Diaz, M. T.; Yan, J.; Downer, M. C.; Henkelman G.; Goodenough J. B.; Zhou J., New Mechanism for Ferroelectricity in the Perovskite $Ca_{2-x}Mn_xTi_2O_6$ Synthesized by Spark Plasma Sintering. *J. Am. Chem. Soc.* **2018,** *140* (6), 2214-2220.
21. Belik, A. A., Rise of A-site columnar-ordered $A_2A'A''B_4O_{12}$ quadruple perovskites with intrinsic triple order. *Dalton Transactions* **2018,** *47* (10), 3209-3217.
22. Tanaka, M.; Katsuya, Y.; Yamamoto, A., A new large radius imaging plate camera for high-resolution and high-throughput synchrotron x-ray powder diffraction by multiexposure method. *Rev. Sci. Instrum.* **2008,** *79* (7), 075106.
23. Tanaka, M.; Katsuya, Y.; Matsushita, Y.; Sakata, O., Development of a synchrotron powder diffractometer with a one-dimensional X-ray detector for analysis of advanced materials. *J. Ceram. Soc. Jpn.* **2013,** *121* (1411), 287-290.
24. Izumi, F.; Ikeda, T. In A rietveld-analysis programm RIETAN-98 and its applications to zeolites, *Mater. Sci. Forum*, **2000**, 321-324, 198-205.
25. Chapon, L. C.; Manuel, P.; Radaelli, P. G.; Benson, C.; Perrott, L.; Ansell, S.; Rhodes, N. J.; Raspino, D.; Duxbury, D.; Spill, E., Wish: The new powder and single crystal magnetic diffractometer on the second target station. *Neutron News* **2011,** *22* (2), 22-25.
26. Rodríguez-Carvajal, J., Recent advances in magnetic structure determination by neutron powder diffraction. *Physica B* **1993,** *192* (1-2), 55-69.
27. Kurtz, S.; Perry, T., A powder technique for the evaluation of nonlinear optical materials. *J. Appl. Phys.* **1968,** *39* (8), 3798-3813.
28. Inaguma, Y.; Aimi, A.; Shirako, Y.; Sakurai, D.; Mori, D.; Kojitani, H.; Akaogi, M.; Nakayama, M., High-pressure synthesis, crystal structure, and phase stability relations of a $LiNbO_3$-type polar titanate $ZnTiO_3$ and its reinforced polarity by the second-order Jahn–Teller effect. *J. Am. Chem. Soc.* **2014,** *136* (7), 2748-2756.

29. Leinenweber, K.; Parise, J., High-pressure synthesis and crystal structure of $CaFeTi_2O_6$, a new perovskite structure type. *J. Solid State Chem.* **1995,** *114* (1), 277-281.

30. Solana-Madruga, E.; Arévalo-López, Á. M.; Dos Santos-García, A. J.; Urones-Garrote, E.; Ávila-Brande, D.; Sáez-Puche, R.; Attfield, J. P., Double Double Cation Order in the High-Pressure Perovskites $MnRMnSbO_6$. *Angew. Chem. Int. Ed.* **2016,** *55* (32), 9340-9344.

31. Zhang, L.; Matsushita, Y.; Yamaura, K.; Belik, A. A., Five-Fold Ordering in High-Pressure Perovskites RMn_3O_6 (R= Gd–Tm and Y). *Inorg. Chem.* **2017,** *56* (9), 5210-5218.

32. Belik, A. A.; Khalyavin, D. D.; Zhang, L.; Matsushita, Y.; Katsuya, Y.; Tanaka, M.; Johnson, R. D.; Yamaura, K., Intrinsic Triple Order in A-site Columnar-Ordered Quadruple Perovskites: Proof of Concept. *Chemphyschem* **2018,** *19* (19), 2449-2452.

33. Belik, A. A.; Zhang, L.; Liu, R.; Khalyavin, D. D.; Katsuya, Y.; Tanaka, M.; Yamaura, K., Valence Variations by B-Site Doping in A-Site Columnar-Ordered Quadruple Perovskites $Sm_2MnMn(Mn_{4-x}Ti_x)O_{12}$ with $1 \leq x \leq 3$. *Inorg. Chem.* **2019,** *58* (5), 3492-3501.

34. Shannon, R. D., Revised effective ionic radii and systematic studies of interatomic distances in halides and chalcogenides. *Acta crystallographica section A: crystal physics, diffraction, theoretical and general crystallography* **1976,** *32* (5), 751-767.

35. Brese, N.; O'keeffe, M., Bond-valence parameters for solids. *Acta Crystallogr. Sect. B: Struct. Sci.* **1991,** *47* (2), 192-197.

36. Belik, A. A.; Matsushita, Y.; Kumagai, Y.; Katsuya, Y.; Tanaka, M.; Stefanovich, S. Y.; Lazoryak, B. I.; Oba, F.; Yamaura, K., Complex Structural Behavior of $BiMn_7O_{12}$ Quadruple Perovskite. *Inorg. Chem.* **2017,** *56* (20), 12272-12281.

37. Maartense, I., Magnetic Properties of Fe^{2+}-Doped $MnCO_3$. *Phys. Rev. B* **1972,** *6* (11), 4324.

38. Zhang, L.; Terada, N.; Johnson, R. D.; Khalyavin, D. D.; Manuel, P.; Katsuya, Y.; Tanaka, M.; Matsushita, Y.; Yamaura, K.; Belik, A. A., High-pressure synthesis, structures, and properties of trivalent A-site-ordered quadruple perovskites RMn_7O_{12} (R= Sm, Eu, Gd, and Tb). *Inorg. Chem.* **2018,** *57* (10), 5987-5998.
39. Stokes, H. T.; Orden, S. v.; Campbell, B. J., ISOSUBGROUP: an internet tool for generating isotropy subgroups of crystallographic space groups. *J. Appl. Crystallogr.* **2016,** *49* (5), 1849-1853.

Chapter 6. General conclusions and future prospects

6.1. General conclusions

The ABO_3 perovskite family contains two quite different A and B sites that can be occupied by different elements. It is said that nearly half of the Periodic Table can be located in the perovskite structure.[1] The distribution of different cations depends on the relative size of A and B cations and the nature of cations.[1]

The high-pressure and high-temperature method is an effective way to synthesize new members of the developing family of A-site columnar-ordered quadruple perovskites. In this thesis, three new triple A-site ordered perovskites $A_2A'A''B_4O_{12}$ have been successfully prepared. They all present attractive magnetic properties and other physical performances. The A site is usually occupied by the rare-earth elements, alkaline, and alkaline earth metals. The A′ site usually accommodates Mn^{2+} and other effective Jahn-Teller cations (Mn^{3+} and Cu^{2+}). The A″ site contains cations that allow tetrahedral coordination. Rare-earth elements usually affect magnetic properties. Mn^{2+} plays a significant role and can easily impact the materials' magnetic performance. $Y_2MnGa(Mn_{4-x}Ga_x)O_{12}$ with x = 0, 1, 2, and 3 solid solutions exhibit spin-glass-like magnetic properties due to the presence of Ga^{3+} at the octahedral B sites. $R_2MnMn(MnTi_3)O_{12}$ compounds with R = Nd, Eu, and Gd show ferrimagnetic properties and exhibit multiferroic activities due to ferrimagnetic and relaxor-like ferroelectric properties which are completely different from properties of the parent $Ca_2MnMnTi_4O_{12}$ compound. $NaRMn_2Ti_4O_{12}$ with R = Sm, Eu, Gd, Dy, Ho, and Y show a large dielectric constant of a possible extrinsic origin similar to the case of $CaCu_3Ti_4O_{12}$. Magnetic and specific heat measurements showed long-range magnetic ordering.

All samples studied in this thesis belong to the A-site columnar-ordered quadruple perovskites and their crystal structures were investigated from the X-ray diffraction and

neutron powder diffractions. Lattice parameters usually follow the monotonic trends depending of the size of rare-earth cations or the amount of dopant cations.

6.2. Future prospects

In the family of $A_2A'A''B_4O_{12}$ perovskites, ferroelectric properties have already been reported.[2] Moreover, new mechanisms of ferroelectricity have been suggested in $CaMnTi_2O_6$.[3] In this thesis, we found compounds that exhibit relaxor-like ferroelectric properties. Therefore, the $A_2A'A''B_4O_{12}$ perovskites show analogues dielectric behaviour with classical ABO_3 perovskites. New mechanisms of spin re-orientation transitions have been reported in $A_2A'A''B_4O_{12}$ perovskites, $R_2CuMnMn_4O_{12}$.[4] Therefore, the $A_2A'A''B_4O_{12}$ perovskites exhibit rich physical properties and have great potential for future development. By selecting appropriate elements, we can achieve improvements in dielectric, ferroelectric, and magnetic properties.

Depending on the charge of the A cations the average oxidation state of manganese at the perovskite B sites can change between +3 and +4, resulting in complex charge-, spin-, and orbital-order transitions and the appearance of spin-induced ferroelectric polarization.[5-10] A-site columnar-ordered $A_2A'A''B_4O_{12}$ quadruple perovskites are in the developing stage of research. Compared with classical ABO_3 perovskites or A-site-ordered $AA'_3B_4O_{12}$ quadruple perovskites, which have twelve-fold coordinated A site and square-planar coordinated A′ site, $A_2A'A''B_4O_{12}$ perovskites are more complex as they have ten-fold coordinated A site, square-planar coordinated A′ site, and an additional tetrahedrally coordinated A″ site. This A″ site makes them unique among perovskite compounds and gives an additional degree of freedom in design because the number of elements that can have a tetrahedral environment is larger than the number of elements that can have a square-planar environment.

Therefore, there are still a lot of possibilities in designing and preparation of new members of the $A_2A'A''B_4O_{12}$ perovskite family and different ways to modify their physical properties.

References in chapter 6

1. Giaquinta, D. M.; Zur Loye, H.-C., Structural predictions in the ABO_3 phase diagram. *Chem. Mater.* **1994,** *6* (4), 365-372.
2. Aimi, D. Mori, K. Hiraki, T. Takahashi, Y. J. Shan, Y. Shirako, J. S. Zhou and Y. Inaguma, High-pressure synthesis of A-site ordered double perovskite $CaMnTi_2O_6$ and ferroelectricity driven by coupling of A-site ordering and the second-order Jahn–Teller effect, *Chem. Mater*., **2014**, 26, 2601–2608.
3. Z. Li, Y. Cho, X. Li, X. Li, A. Aimi, Y. Inaguma, J. A. Alonso, M. T. Fernandez-Diaz, J. Yan, M. C. Downer, G. Henkelman, J. B. Goodenough and J. Zhou, New mechanism for ferroelectricity in the perovskite $Ca_{2-x}Mn_xTi_2O_6$ synthesized by spark plasma sintering, *J. Am. Chem. Soc.*, **2018**, 140, 2214−2220.
4. Vibhakar, A.; Khalyavin, D.; Manuel, P.; Liu, J.; Belik, A.; Johnson, R., Spontaneous rotation of ferrimagnetism driven by antiferromagnetic spin canting. *Phys. Rev. Lett.* **2020,** *124* (12), 127201.
5. Johnson, R.; Mezzadri, F.; Manuel, P.; Khalyavin, D.; Gilioli, E.; Radaelli, P., Evolution of Magneto-Orbital order Upon B-Site Electron Doping in $Na_{1-x}Ca_xMn_7O_{12}$ Quadruple Perovskite Manganites. *Phys. Rev. Lett.* **2018,** *120* (25), 257202.
6. Belik, A. A.; Glazkova, Y. S.; Terada, N.; Matsushita, Y.; Sobolev, A. V.; Presniakov, I. A.; Tsujii, N.; Nimori, S.; Takehana, K.; Imanaka, Y., Spin-driven multiferroic properties of $PbMn_7O_{12}$ perovskite. *Inorg. Chem.* **2016,** *55* (12), 6169-6177.
7. Chen, W.-T.; Wang, C.-W.; Wu, H.-C.; Chou, F.-C.; Yang, H.-D.; Simonov, A.; Senn, M. S., Improper ferroelectric polarization in a perovskite driven by intersite charge transfer and ordering. *Phys. Rev. B* **2018,** *97* (14), 144102.

8. Johnson, R.; Chapon, L.; Khalyavin, D.; Manuel, P.; Radaelli, P.; Martin, C., Giant improper ferroelectricity in the ferroaxial magnet $CaMn_7O_{12}$. *Phys. Rev. Lett.* **2012,** *108* (6), 067201.
9. Terada, N.; Glazkova, Y. S.; Belik, A. A., Differentiation between ferroelectricity and thermally stimulated current in pyrocurrent measurements of multiferroic MMn_7O_{12} (M= Ca, Sr, Cd, Pb). *Phys. Rev. B* **2016,** *93* (15), 155127.

.

List of appended publications

This thesis is based on the following publications.

1. Scientific papers in peer-reviewed journals

1. **Ran Liu**, Masahiko Yanaka, Hiromu Mori, Yoshiyuki Inaguma, Kazunari Yamuura, and Alexei A. Belik, Ferrimagnetic and relaxor ferroelectric Properties of $R_2MnMn(MnTi_3)O_{12}$ perovskites with Rn = Nd, Eu, and Gd, *J. Mater. Chem. C.* **2021**, 9(3), 947-956

2. **Ran Liu**, Rebecca Scatena, Dmitry D. Khalyavin, Roger D. Johnson, Yoshiyuki Inaguma, Masahiko Tanaka, Yoshitaka Matsushita, Kazunari Yamaura, and Alexei A. Belik. High-Pressure Synthesis, Crystal Structures, and Properties of A-Site Columnar-Ordered Quadruple Perovskites $NaRMn_2Ti_4O_{12}$ with R = Sm, Eu, Gd, Dy, Ho and Y, *Inorg. Chem.* **2020**, 59, 9065–9076

3. **Ran Liu**, Masahiko Tanaka, Kazunari Yamaura, Alexei A. Belik. High-pressure synthesis, crystal structures, and magnetic and dielectric properties of $GdFeO_3$-type perovskites $(Dy_{0.5}Mn_{0.5})(Mn_{1-x}Ti_x)O_3$ with x= 0.5 and 0.75. *J. Alloys Compd.* **2020**, 825, 154019.

4. **Ran Liu**, Dmitry D. Khalyavin, Naoki Tsunoda, Yu Kumagai,, Fumiyasu Oba, Yoshio Katsuya, Masahiko Tanaka, Kazunari Yamaura, and Alexei A. Belik. Spin-Glass Magnetic Properties of A-Site Columnar-Ordered Quadruple Perovskites, $Y_2MnGa(Mn_{4-x}Ga_x)O12$ with $0 \leq x \leq 3$, *Inorg. Chem.* **2019**, 58, 14830−14841

5. Anuradha M. Vibhakar, Dmitry D. Khalyavin, Pascal Manuel, **Ran Liu**, Kazunari Yamaura, Alexei A. Belik, and Roger D. Johnson, Effects of magnetic dilution in the ferrimagnetic columnar ordered $Sm_2MnMnMn_{4-x}Ti_xO_{12}$ perovskites. *Phys. Rev. B* **2020**,

102 (21), 214428.

6. Alexei A. Belik, Lei Zhang, **Ran Liu**, Dmitry D. Khalyavin, Yoshio Katsuya, Masahiko Tanaka, and Kazunari Yamaura, Valence Variations by B-Site Doping in A-Site Columnar-Ordered Quadruple Perovskites $Sm_2MnMn(Mn_{4-x}Ti_x)O_{12}$ with $1 \leq x \leq 3$, *Inorg. Chem.* **2019**, 58, 3492−3501

2. Oral presentations on conferences

1. **Ran Liu**, Dmitry D. khalyavin, Naoki Tsunada, Yu Kumagai, Fumiyasu Oba, Yoshio Katsuya, Masahiko Tanaka, Kasumari Yamaura, and Alexei A. Belik, "Spin-Glass Magnetic Properties of A-Site Columnar-Ordered Quadruple Perovskites $Y_2MnGa(Mn_{4-x}Ga_x)O_{12}$ with $0 \leq x \leq 3$", The 29th Annual Meeting of MRS-J: Sunrise of New Materials Innovation, Nov.27-29, 2019, Yokohama, Japan

2. **Ran Liu**, Dmitry D. Khalyavin, Naoki Tsunoda, Yu Kumagai, Fumiyasu Oba, Yoshio Katsuya, Masahiko Tanaka, Kazunari Yamaura, and Alexei A. Belik, "Crystal structures and magnetic properties of A-site columnar-ordered quadruple perovskites", The 11th International Conference on the Science and Technology for Advanced Ceramics, Jul. 9-11, 2019, Tsukuba, Japan

3. **Ran Liu**, Yoshio Katsuya, Masahiko Tanaka, Kazunari Yamaura, Alexei A. Belik, "Crystal structures and magnetic properties of A-site columnar-ordered quadruple perovskites $Y_2MnGa(Mn_{4-x}Ga_x)O_{12}$", The 28th Annual Meeting of MRS-J: Materials Innovation for Recycling-Based Society, Dec.18-20, 2018, Kitakyushu, Japan

Acknowledgment

I would like to express my gratitude to all those who helped me during the writing of this thesis. Firstly, I gratefully acknowledge the help of my supervisor Prof. Kazunari Yamaura and Prof. Alexei Belik. They give me the most suggestions and help in my studies. Thank their kindness and patience in helpt me address the problems when I met kinds of difficulties. In these years，Prof. Yamaura gave me a lot of support both on the research and living in Japan. Prof. Alexei gave me important instructions in the research and taught me how to be an experimentalist but also as an independent thinker. Their enthusiasm in science, diligence, and personality will inspire me in my future journey in science.

I also would like to thank Prof. Yoshihiro Tsujimoto for helping me to check the High-Pressure apparatus when I met the water problem. Besides, I want to thank Dr. Yoshitaka Matsushita, Dr. Yoshio Katsuya, and Dr. Masahiko Tanaka, for their help in SXRD measurement and XRPD measurement. I would like to give my gratitude to Dr. Yu Su, and Dr. Lei Zhang, because they taught me how to use lab facilities and gave me some advice, and help me to learn the data process. I would like to thank Mr. Hong Yan and Ms. Xun Kang for their help and supports. Furthermore, I would like to say thanks to my parents and my brother for their endless support.

I would like to express my gratitude to all of you again. Because of you, I could get such achievements.